Synthesis, Characterization of Ruthenium-Titanium Mixed Oxide and the Effect of Hydrogen Incorporation on Catalytic Propane and HCl Oxidation Reactions

Cumulative dissertation

Presented by

Wei Wang

Submitted to the
Faculty of Biology and Chemistry
and prepared in the
Institute of Physical Chemistry

For the degree of
Doktor der Naturwissenschaften
(*Dr. rer. nat.*)
Justus Liebig University Giessen, Germany
Giessen, December 2023

This thesis is accepted as a doctoral dissertation in fulfillment of the requirements for the degree of *Doctor Rerum Naturalium* by the Faculty of Biology and Chemistry, Justus Liebig University Giessen, Germany.

1st. Reviewer Prof. Dr. Herbert Over

Institute of Physical Chemistry, Justus Liebig University Giessen

2nd. Reviewer Prof. Dr. Yun Guo

Research Institute of Industrial Catalysis, East China University of Science & Technology

I declare that I have completed this dissertation single-handedly without the unauthorized help of second party and only with the assistance acknowledged therein. I have appropriately acknowledged and referenced all text passages that are derived literally from or based on the content of published or unpublished work of others, and all information that relates to verbal communications. I have abided by the principles of good scientific conduct laid down in the character of the Justus-Liebig-University of Giessen in carrying out the investigations described in the dissertation.

Gießen, den 07.11.2023	Wie Wang
Location, date	Signature

Acknowledgements

The present thesis is finalized under the meticulous guidance of Prof. Dr. Herbert Over. First of all, I would like to sincerely express my heartfelt appreciation to him for generously providing me the opportunity to work in such an excellent group for the present thesis as a joint Ph.D. student at the Justus Liebig University Giessen. As my supervisor, Prof. Dr. Herbert Over has invested significant dedication and effort on my Ph.D. project "Synthesis, Characterization of Ruthenium-Titanium Mixed Oxide and the Effect of Hydrogen Incorporation on Catalytic Propane and HCl Oxidation Reactions". During the initial exploratory period of this project, substantial difficulties and challenges were encountered while Prof. Dr. Herbert Over was patient with my shortcomings and always offered prompt and insightful guidance. With his continuous encouragement and targeted instruction over the past three years, I have made significant improvements in my abilities to analyze the experimental data from different aspects and proceed the research project with more positive attitude. Additionally, I am also appreciative of his quick and constructive feedback regarding scientific paper writing. Furthermore, Prof. Dr. Herbert Over's thorough approach to science and professionalism deeply impressed me and will continue to influence me during a lifelong time.

I would like to equally express my sincere appreciation to my supervisor Prof. Dr. Yun Guo at the East China University of Science and Technology, China. When I became a doctoral candidate eight years ago, Prof. Dr. Yun Guo provided me with ample space for exploration of my doctoral research topics, he was patient with my shortcomings and always offered constructive guidance whenever I encountered challenges both in research and life. He gradually cultivated me to look at problems with an objective and dialectical mentality, enabling me to effectively discover, understand and solve problems. His great personalities will also continue to affect me throughout my life.

I would also like to express my gratitude to Prof. Dr. Bernd M. Smarsly, who co-supervised my research at Justus Liebig University Giessen. He not only provided the necessary equipment for catalyst preparation and characterization, but also engaged in assistance in conducting comprehensive data analysis and creative suggestions. Furthermore, I appreciate his inspiring comments and assistance in refining the language in the scientific paper writing.

I would like to thank all current and former members of AG Over for providing me a relaxing group atmosphere, great help in experiment and life and good cooperation over the last few years. I specially thank Phillip Timmer for constructing the propane oxidation apparatus and helpful data analysis. I also thank Alexander Spriewald Luciano for his kind help in building the HCl oxidation apparatus, CO pulse adsorption apparatus and modification of the

"Kurzzusammenfassung". I thank Dr. Tim Weber and Lorena Glatthaar for their support in XPS and eletrocatalysis measurements. I specially thank Dr. Tim Weber for proofreading the present thesis. I would like to thank Dr. Chenwei Li, Dr. Yu Sun, Dr. Zheng Wang and Dr. Omeir Khalid for their helpful guidance and fruitful discussions. I would also like to thank Yu Wang, Volkmar Koller and Florian Rink for their friendly help and discussion. Special highlight to Gabi Scheller for her support with all the organizational issues.

I would like to thank all the other professors from the Research Institute of Industrial Catalysis, such as Prof. Yanglong Guo, Prof. Wangcheng Zhan, and Prof. Li Wang.

Many thanks to all the other colleagues who offered me the instrumental supports in my scientific experiments from both universities. I would like to thank Dr. Rafael Meinusch, Dr. Jaime Gallego, Dr. Sebastian Werner, Usman Ali, Felix Boll, Raoul Brand, Matteo Crisci, Paul Debes, Fabian Schmitz, Lysander Wagner, Aline Trommer and Antonella D'Ambrosio from AG Smarsly. I thank Dr. Boris Mogwitz, Dr. Bjoern Luerßen, and Dr. Klaus Peppler for their technical support. I thank Hao Lu from AG Klar for Raman measurements and helpful discussion. Many thanks to Yongkai Shi, Dr. Jian Zhou, Dr. Wenchao Hua, Dr. Yu Fu, Mingqi Li, Dongsheng Ye, Xiaohan Guo, Dr. Xuan Tang, Shasha Ge, Jihang Yu, Min Ding.

I gratefully acknowledge the China Scholarship Council (CSC) for the financial support during my two-year research period (from November 2020 to November 2022) at the Institute of Physical Chemistry of Justus Liebig University Giessen. I thank Prof. Herbert Over again for his financial support to continue my research work and finish the thesis.

Finally, I extend my heartfelt thanks to my family members and friends, who have shown me love, encouragement and full support during my whole period of study.

Kurzzusammenfassung

Mischoxid-Katalysatoren spielen sowohl in der Grundlagenforschung als auch bei industriellen Anwendungen eine zentrale Rolle, da sie in der Lage sind, vorteilhafte Eigenschaften der enthaltenen Elemente zu integrieren. Unter diesen ist $Ru_xTi_{1-x}O_2$ ein herausragendes Mischoxid, da es günstige elektro- und thermokatalytische Eigenschaften aufweist. Es gibt eine Vielzahl von Studien zur Synthese und Charakterisierung von Ru-Ti-Mischoxiden. Wobei die Löslichkeit von Ruthenium und Titan in der jeweils anderen Oxidphase und deren Phasenreinheit noch nicht geklärt wurde. Daher ist es notwendig, $Ru_xTi_{1-x}O_2$ herzustellen, die Ru- und Ti-Zusammensetzung in einem weiten Bereich zu variieren und durch umfassende Charakterisierung Einblicke in ihre physikalischen und chemischen Eigenschaften zu gewinnen. Wasserstoffinduziertes Katalysator-Engineering wurde kürzlich als vielversprechende Strategie zur Erzielung einer überlegenen katalytischen Leistung sowohl bei Hydrierungs- als auch Dehydrierungsreaktionen beschrieben und nachgewiesen. Der Einbau von Wasserstoff in das Gitter des Oxidmaterials führt in der Regel zur Bildung einer Hydridspezies oder Hydroxylgruppen, begleitet von Gitterverspannungen, die das katalytische Verhalten des Materials beeinflussen können. Bei Ru-Ti-Mischoxiden ist noch nicht klar, ob Wasserstoff in den Bulk-Bereich eingeführt werden kann. Darüber hinaus wurde in der Literatur noch nicht über die Auswirkungen der Einbringung von Wasserstoff in die Bulk-Oxide bei der thermischen Katalyse berichtet. Daher besteht das Hauptziel der vorliegenden Arbeit darin, die potenzielle Anwendung von wasserstoffinkorporierten Ru-Ti-Mischoxiden in der Oxidationskatalyse, anhand der HCl-Oxidationsreaktion und der Propanverbrennung, zu untersuchen.

In der vorliegenden Arbeit werden $Ru_xTi_{1-x}O_2$ in der Rutil-Phase durch die konventionelle Sol-Gel-Methode synthetisiert und zeigen eine deutliche Mischbarkeitslücke in einem breiten Zusammensetzungsbereich ($0{,}2 \leq x \leq 1$). Die Einwirkung von H_2 bei 250 °C (250R) führt zu einem Wasserstoffeinbau, der mit einer Gitterverspannung einhergeht, was wiederum die Oxidationskatalyse der Propanverbrennung erheblich fördert. Von allen Katalysatoren ist $Ru_{0.6}Ti_{0.4}O_2$_250R der katalytisch aktivste. Darüber hinaus wurde $Ru_{0.3}Ti_{0.7}O_2$ ausgewählt, um die strukturelle und elektronische Entwicklung bei der Behandlung mit H_2 bei erhöhten Temperaturen zu untersuchen. 17,6 mol% Wasserstoff können in das Mischoxid $Ru_{0.3}Ti_{0.7}O_2$ eingebaut werden, während dies bei reinem Rutil-RuO_2 und -TiO_2 nicht möglich ist, da es entweder zu metallischem Ru reduziert wird oder keine Wasserstoffaufnahme zulässt. Es wird gezeigt, dass mit Wasserstoff inkorporiertes $Ru_{0.3}Ti_{0.7}O_2$ die katalytische Leistung bei Oxidationsreaktionen wie der vollständigen Oxidation von Propan und der HCl-Oxidationsreaktion erheblich verbessert. Die wasserstoffinduzierte Gitterverspannung in $Ru_{0.3}Ti_{0.7}O_2$, die mit veränderten elektronischen Eigenschaften einhergeht, ist wahrscheinlich der Grund für die beobachtete verbesserte katalytische Aktivität. Die Bildung einer festen Lösung eines reduzierbaren Oxids mit einem weniger (oder nicht) reduzierbaren Oxid könnte die Möglichkeit eröffnen, erhebliche Mengen an Wasserstoff durch Einwirkung von H_2 bei erhöhten Temperaturen einzubringen, was einen zusätzlichen Parameter zur Feinabstimmung der katalytischen Leistung in verschiedenen katalytischen Reaktionen in situ darstellt.

Abstract

Mixed oxide catalysts play a pivotal role in both fundamental research and industrial applications due to their ability to integrate advantageous properties from the different elements contained. Among all, $Ru_xTi_{1-x}O_2$ is a kind of highly regarded mixed oxide material since it exhibits favorable electro and thermocatalytic properties. There is a variety of studies on the synthesis and characterization of the Ru-Ti mixed oxides, while the solid solution limit or solubility of the ruthenium and titanium into each other's oxide phase is still ambiguous and the phase purity has not been clarified yet. Therefore, it is necessary to prepare $Ru_xTi_{1-x}O_2$ varying the Ru and Ti compositions at full range and subsequently gain comprehensive insights into their physical and chemical properties via dedicated characterization methods. Hydrogen induced catalyst engineering has been recently reported and demonstrated as a promising strategy to obtain superior catalytic performance in both hydrogenation and dehydrogenation reactions. The incorporation of hydrogen into the lattice of the oxide material will normally result in the formation of a hydride species or hydroxyl groups, accompanied by changes of the lattice strain, which as a consequence may influence the catalytic behavior of the material. For Ru-Ti mixed oxides, it is not clear yet whether hydrogen can be inserted into the bulk region. Moreover, the effect of hydrogen insertion into the bulk oxides in thermal catalysis has not yet been reported from the literature. Hence, the main objective of the present thesis is to explore the potential application of hydrogen-incorporated Ru-Ti mixed oxides in oxidation catalysis, such as propane combustion and HCl oxidation reactions.

In the present research, rutile-phase $Ru_xTi_{1-x}O_2$ are synthesized via the conventional sol-gel method and reveal a clear miscibility gap in a wide composition range ($0.2 \leq x \leq 1$). Hydrogen exposure at 250 °C (250R) results in hydrogen incorporation accompanied with lattice strain, which in turn significantly promotes the oxidation catalysis of propane combustion. Among all, $Ru_{0.6}Ti_{0.4}O_2$_250R represents the catalytically most active catalyst. Furthermore, $Ru_{0.3}Ti_{0.7}O_2$ sample is chosen to investigate the structural and electronic evolution upon hydrogen treatment at elevated temperatures. 17.6 mol% of hydrogen can be incorporated into the mixed oxide $Ru_{0.3}Ti_{0.7}O_2$, while this is not possible for pure rutile RuO_2 and TiO_2 that is either reduced to metallic Ru or does not allow for hydrogen absorption, respectively. It is demonstrated that hydrogen-incorporated $Ru_{0.3}Ti_{0.7}O_2$ improves substantially the catalytic performance in oxidation reactions such as the total oxidation of propane and HCl oxidation reaction. Hydrogen-induced lattice strain in $Ru_{0.3}Ti_{0.7}O_2$ accompanied by altered electronic properties is likely to be the reason for the observed enhanced catalytic activity. The formation of a solid solution of a reducible oxide with a (non or) less reducible oxide may open the way to incorporate substantial amounts of hydrogen via simple exposure to H_2 at elevated temperatures, providing an additional parameter to fine-tune in situ the catalytic performance in various catalytic reactions.

Table of Content

1. Introduction and Motivation

1.1 Catalysts in Chemical Processes

Since the Second Industrial Revolution, the rapid development of modern science and technology has enabled the traditional industries to greatly thrive, leading to significant changes in human society. Chemical industry, as the center of the modern science and technology, mainly involves the conversion of raw materials such as oil, natural gas, water, metals, and minerals into industrial and consumer goods, which are widely used in our daily life. In chemical industry, catalysts are widely utilized in most chemical processes, such as Haber-Bosch, Fischer-Tropsch or Deacon process etc. to accelerate the reaction rate and increase the production efficiency. A catalyst usually comes out of the catalytic cycle without being altered [**1**].

In chemical processes, undesired or hazardous compounds or byproducts can also be inevitably produced, which may cause negative impact on human health and environment. For example, the combustion in a combustion engine using gasoline or diesel as fuel, on the one hand significantly promotes the energy efficiency, but on the other hand emits harmful exhausts such as particulate matter (PM), nitrogen oxides (NO_x), carbon monoxide (CO) and hydrocarbons (HC) which causes severe air pollution [**2, 3**]. The elimination of these pollutants and the curtailment of the undesired byproducts can also be boosted through catalytic processes. From these aspects, catalysts have been pivotal elements of technology in the past and will continue to be so in the future.

In the past few decades, many efforts have been devoted for the development of catalysts which are sufficiently active and durable to be applied under practical conditions. In order to optimize its performance and the stability, rational design of a catalyst is of paramount importance. In recent years, catalyst modulation at the atomic scale could be achieved by the continuous development of nanomaterial synthesis techniques. As a result, precise and controllable synthesis of nanoscale catalysts has become a hot topic in research.

1.1.1 Mixed Oxides Catalysts: Better Mixed than Bare

Metal oxides are a kind of important catalyst materials, which have been utilized in a wide range in heterogeneous catalysis, with the purpose to combine beneficial properties of different elements [**4–6**]. Mixed oxides materials normally exhibit improved physiochemical properties

compared to the corresponding pure oxides. Here, an example is CeO_2-based materials: ceria is extensively used in three-way catalysis because of its remarkable oxygen storage capacity (OSC) [**7, 8**], it can store and release oxygen under rich and lean conditions. However, CeO_2 suffers sintering when the temperature is higher than 800 °C. A commonly adapted solution to increase its thermal stability is to incorporate foreign ions such as zirconium or praseodymium [**9–11**]. The $Ce_xZr_{1-x}O_2$ solid solution is not only more stable upon high-temperature annealing, but also shows even higher OSC, thus being a more suitable candidate in real applications [**12**].

Another example is RuO_2, a characteristic rutile-phase oxide with a tetragonal crystallographic structure, classified under the space group $P4_2/mnm$ (No. 136). RuO_2-based materials are promising catalysts in various important reactions [**13**]. In thermal catalysis, RuO_2 has been proven the most active catalyst at low temperature in the HCl oxidation reaction, namely the Deacon process [**14**]. A supported RuO_2/rutile-TiO_2 catalyst has been developed and commercialized by Sumitomo Chemicals since 1999 [**15**]. In electrocatalysis, RuO_2 is regarded as the most active catalyst in oxygen evolution reaction (OER) [**16–18**]. Despite its excellent catalytic performance in both thermal and electro-catalysis, RuO_2 suffers not only from thermal instability by transformation into volatile RuO_4 at higher temperature, but also from corrosion in both acid and base electrolyte [**17**]. To improve the stability of RuO_2 both in thermal and electro-catalysis, the formation of a mixed oxide with other rutile-structured oxides such as TiO_2 and IrO_2 is the simplest and most efficient approach. RuO_2-TiO_2 mixed oxide electrodes principally serve as the benchmark dimensionally stable anodes (DSAs) with high conductivity and corrosion resistance in the large scale chloralkali process [**19**]. In the Deacon process, mixing ruthenium with titanium can result in higher stability while preserving high activity. In case of RuO_2 nanofibers severe sintering was observed after applying harsh reaction conditions, while mixed $Ru_{0.15}Ti_{0.85}O_2$ fibers do not reveal any morphological changes upon reaction, showcasing that titanium can stabilize the active RuO_2 phase of the catalyst material [**20**]. More importantly, mixing with less expensive Ti can reduce the input of Ru, since ruthenium is still a relatively high-priced noble metal (the average price of ruthenium is around $15,000 per kg from September 1st to October 1st 2023; for comparison, the average price of titanium is about $6 per kg from September 1st to October 1st 2023) [**21**].

1.1.2 Synthesis of Mixed Ruthenium-Titanium Oxides

RuO_2 and rutile TiO_2 share the similar tetragonal unit cells with virtually the same unit cell volumes (62.70 Å^3 for RuO_2 and 62.43 Å^3 for TiO_2), while the ionic radii of Ru^{4+} and Ti^{4+} are also very similar with 0.67 Å and 0.68 Å, respectively [**22**]. Even though the octahedral

structures are slightly different (as shown in **Figure 1.1**), a well-mixed RuO_2-TiO_2 at atomic scale is expected to be achieved by dedicated synthesis strategies. In doing so, various preparation methods have been reported in the literature in order to synthesize the binary $Ru_xTi_{1-x}O_2$ mixed oxides.

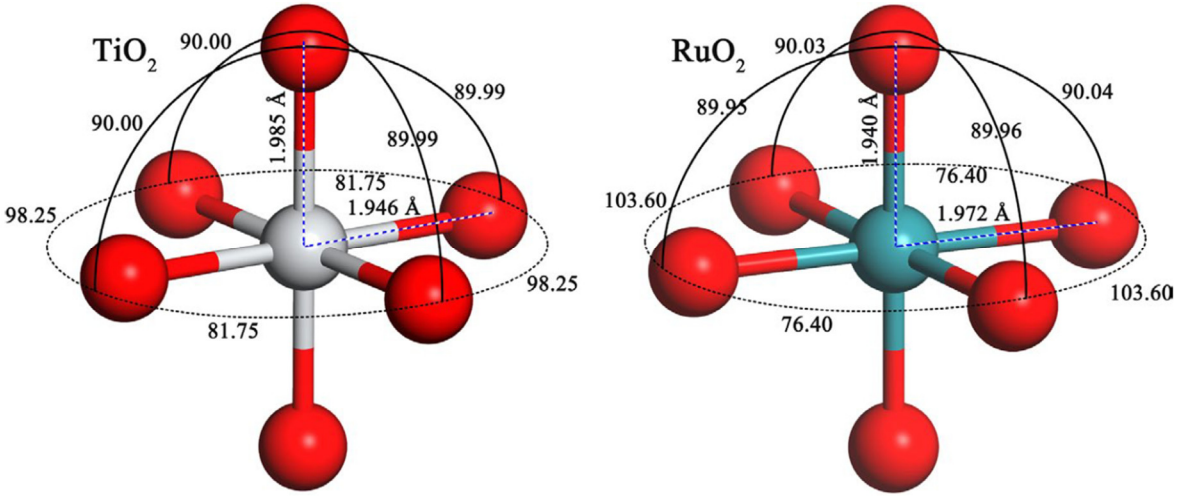

Figure 1.1. Octahedral structures in rutile TiO_2 (left) and RuO_2 (right). Reprinted with permission from reference [**22**]. Copy right 2019 John Wiley and Sons.

A RuO_2-TiO_2 electrode coating is usually synthesized by thermal decomposition of the metal chloride ($RuCl_3 \cdot xH_2O$) or alkoxide after painting corresponding suspension on metal substrates. In 1977, Gerrard *et al.* prepared RuO_2-TiO_2 coatings with varied Ru nominal ratios on flat titanium/silica substrates, using $RuCl_3$ and $TiCl_4$ as precursors. Calcination at 400 °C ~ 450 °C produces a metastable RuO_2-TiO_2 solid solution or a finely dispersed mixture of the two phases, the rutile d-spacings of the (110) and (211) reflections as a function of composition exhibit a marked deviation from Vegard's law. At higher annealing temperatures (700 ~ 800 °C) it appears that only almost pure rutile TiO_2 and RuO_2 phases co-exist with only very limited solid solubility [**23**]. $Ru_xTi_{1-x}O_2$ coatings prepared by Duvigneaud *et al.* also indicate the lattice parameters *a*/*b*, *c* to not follow Vrgard's law. They conclude ruthenium and titanium can form partial solid solutions at temperatures above 1000 °C, while complete miscibility is possible in the temperature range of 350 °C ~ 600 °C [**24**]. Guglielmi *et al.* prepared a RuO_2/TiO_2 layer coating with a molar ratio of 30/70 from a mixture of titanium iso-propoxide and different ruthenium precursors: ruthenium(III) nitrosyl nitrate, ruthenium(III) chloride and ruthenium(III) acetylacetonate. X-ray diffraction (XRD) data indicates after calcination at 400 °C that a rutile

solid solution can be obtained and the types of ruthenium precursors do not affect the phase purity [**25**].

The sol-gel method is widely applied for the synthesis of mixed oxide materials. Kameyama *et al.* prepared isolated RuO_2-TiO_2 oxide particles via a sol-gel method consisting of hydrolysis and condensation of metal alkoxides. They claim that a perfect Ru-Ti solid solution is formed at high ruthenium doping levels, while in Ti-rich samples a clear phase separation was observed [**26**]. Osman *et al.* also synthesized RuO_2-TiO_2 gels and powders via the hydrolysis of ruthenium alkoxide/titanium tetra-ethoxide mixtures. The ruthenium: titanium ratio was kept at 4:1 for all samples. For uncalcined gels, X-ray fluorescence (XRF) data reveals significant disparities from the nominal ratio, which is due to ruthenium precipitating out of the system before the titanium precursor is added, as the authors hypothesize. This seems to be an unavoidable result of the high concentrations of $RuCl_3$ required [**27**]. Málek *et al.* assume that $Ru_xTi_{1-x}O_2$ by sol-gel preparation is a single-phase rutile-type solid solution for $0 \leq x \leq 0.7$. However, the lattice parameters of the as-synthesized sample shows a deviation from Vegard's law [**28**]. Investigations of Colomer *et al.* indicate that the calcination temperature of the $Ru_xTi_{1-x}O_2$ xerogels plays an important role for the final state of the crystalline phase distribution. Low temperature calcination at 300 ~ 400 °C results in the solid solubility of $x \leq 0.3$ for RuO_2 incorporated into rutile-TiO_2. Calcination at 500 °C leads to decreased solubility within the range of $0.05 \leq x < 0.1$, probably due to the meta-stability properties of the rutile solid solutions containing RuO_2 at above 400 °C. However, Ru and Ti-rich rutile $Ru_xTi_{1-x}O_2$ solid solution co-exist after calcination at 700 °C [**29**].

In addition to the conventional thermal decomposition and sol-gel methods, researchers explore alternative approaches for synthesizing Ru-Ti mixed oxides. Morais *et al.* prepared $Ru_{0.9}Ti_{0.1}O_2$ and $Ru_{0.1}Ti_{0.9}O_2$ mixed oxide catalysts by a one-pot hydrothermal method. X-ray diffraction (XRD) pattern reveals a clear phase-separation after incorporation of TiO_2 for both samples, for $Ru_{0.1}Ti_{0.9}O_2$ even an anatase TiO_2 phase appears while shifts of the reflections indicate only limited inclusion of titanium ions within the RuO_2 matrix. X-ray photoelectron spectroscopy (XPS) also points to a higher concentration of Ti on the surface compared to the nominal one [**30**]. Christian *et al.* synthesized $Ru_xTi_{1-x}O_2$ ($0.02 < x < 0.5$) nanofibers by an electrospining method and subsequent calcination at 475 °C. For $x \leq 0.05$, anatase phase of nanofibers is predominant while for $x \geq 0.1$ rutile $Ru_xTi_{1-x}O_2$ solid solution is obtained exclusively [**20**]. Dória *et al.* applied both Pechini and ionic liquid method to synthesize a $Ru_{0.3}Ti_{0.7}$ coating on a metallic titanium plate. The splitting of the (101) reflection in XRD also reveals a metastable solid solution of the two components can be formed [**31**].

Hrovat *et al.* explore the extent of solid solubility in the RuO_2-TiO_2 system, they apply solid-phase synthesis by mixing RuO_2 and TiO_2 and then subsequent annealing at varying temperatures up to 1350 °C. The highest temperature is set at 1350 °C due to thermal decomposition of RuO_2 into metallic ruthenium and oxygen (cf. **Figure 1.2a**). According to wavelength-dispersive X-ray spectroscopy (WDS) analysis, solid solubility at 1350 °C is determined to be 16.5% of TiO_2 in RuO_2 and 13.5% of RuO_2 in TiO_2 [**32**]. Jacob *et al.* further refine the phase diagram for the RuO_2-TiO_2 system in air, based on similar experimental protocols as Hrovat *et al.* They find that at 1120 °C, a two-phase mixture containing RuO_2-rich solid solution (ss) and TiO_2-rich solid solution (ss) is encountered in a wide range with limited solubility of around 10 mol%. The solubility of TiO_2 in RuO_2 increases with increasing temperature, which means the miscibility gap is reduced upon high-temperature calcination (cf. **Figure 1.2b**) [**33**].

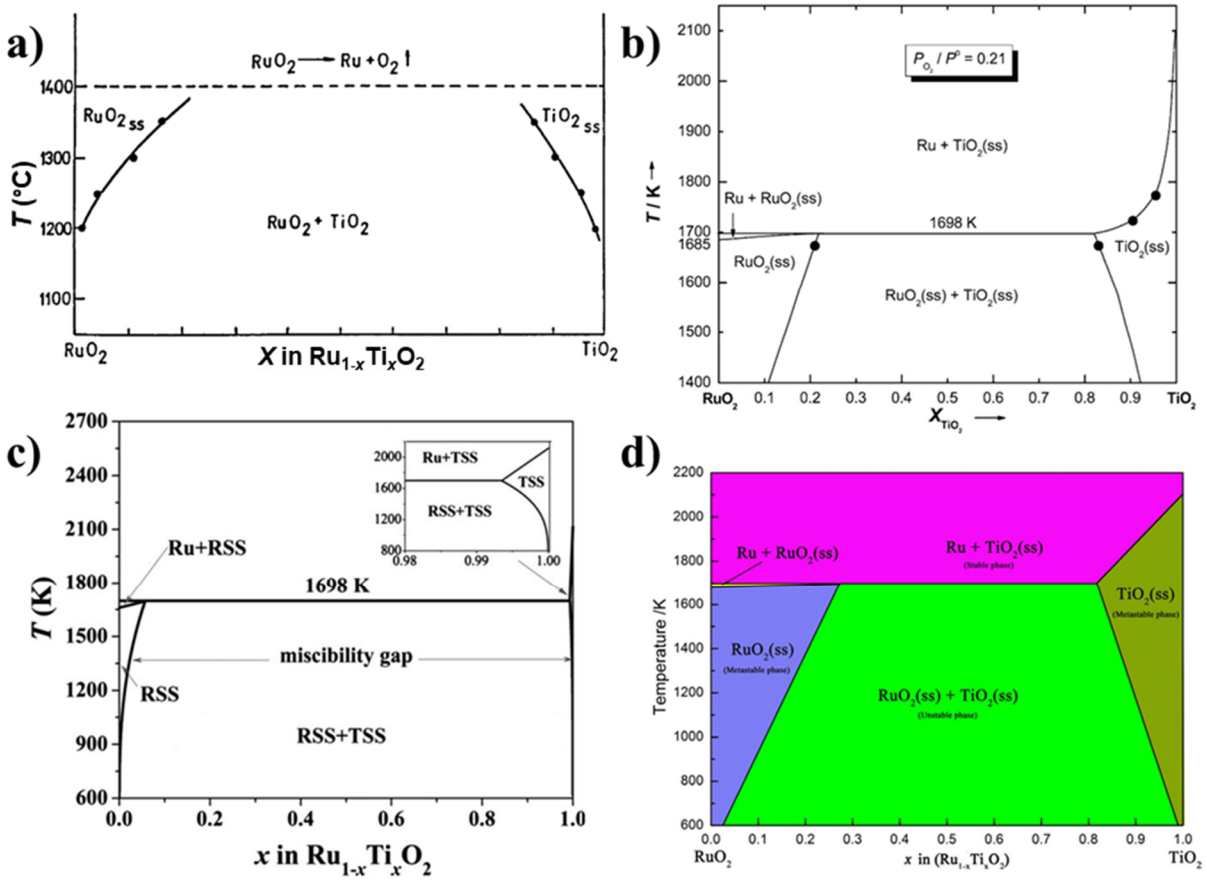

Figure 1.2. The RuO_2-TiO_2 phase diagram as proposed by different studies. a) is reprinted with permission from reference [**32**]. Copy right 2011 Springer Nature; b) is adapted with permission from reference [**33**]. Copy right 2007 Springer Nature; c) is adapted with permission from reference [**34**]. Copy right 2015 John Wiley and Sons; d) is reprinted with permission from reference [**22**]. Copy right 2019 John Wiley and Sons.

In order to gain a more fundamental understanding of this oxide system, density functional theory (DFT) calculations are recently utilized by some researchers. Wang *et al.* study the $Ru_xTi_{1-x}O_2$ solid solution combining both DFT calculation and experimental data. After comparison they find that conventional phase analysis based on Vegard's law leads to 8% - 32% deviation in total composition from the actual value of the $Ru_xTi_{1-x}O_2$ samples as derived from DFT computations. The catalysts prepared by sol-gel method contain three different phases: TSS (TiO_2 solid solution), RSS (RuO_2 solid solution), and ISS (intermediate solid solution) (cf. **Figure 1.2c**). The authors finally conclude that the regular experimental conditions and compositions are located in the broad spinodal regime. Therefore, complete miscibility of RuO_2 and TiO_2 is not likely under regular sample preparation conditions and mixtures of Ru-rich and Ti-rich solid solution phases dominate [**34**]. Yang *et al.* further investigate the structural and electronic properties of rutile solid solutions by DFT calculations. The computed phase diagram indicates that the limit of dissolution for Ti in RuO_2 is located at 0.27 (Ru-rich) and 0.81 (Ti-rich) at a temperature of 1425 °C (cf. **Figure 1.2d**). The main reason for the phase separation is attributed to the different local octahedral structure of RuO_2 and TiO_2, and the different interaction of valence electrons [**22**].

According to the above-mentioned literature, it seems that there is still controversy about the exact solid solubility of ruthenium and titanium. The preparation method and the calcination temperature jointly play an important role in determining the phase formation and the stability. Moreover, most of the publications do not provide systematic information at a full composition range, hence some of the conclusions lack sufficient evidence. Therefore, synthesis and characterization of the $Ru_xTi_{1-x}O_2$ solid solution with varying the composition x in the full range, while keeping the preparation and calcination temperature constant is important for gaining an overview of the structural evolution of and may provide additionally detailed knowledge of the $Ru_xTi_{1-x}O_2$ solid solution.

1.2 Hydrogen-Induced Catalyst Engineering

1.2.1 Strong Metal Support Interaction (SMSI)

Fine-tuning of a catalyst is of great importance for further improvement its catalytic activity. Among the varying strategies of catalyst engineering, hydrogen-induced modulation of the catalytic properties is gaining more and more interest in recent years. For a supported catalyst, nanoparticles on the surface of the support generally exhibit a high fraction of undercoordinated atoms, which makes it easier to react with molecular hydrogen and as a result cause a

reconstruction of active sites [**35, 36**]. For example, in the case of supported platinum catalysts such as Pt/TiO_2 or Pt/Al_2O_3, hydrogen treatment at elevated temperature is one of the simplest approach for the re-dispersion of Pt nanoparticles. For Pt/Al_2O_3, DFT studies indicate that annealing temperature and H_2 pressure strongly affect the state of Pt_{13} particles: high temperature and low H_2 pressure will lead to a biplanar geometry in which Pt strongly interacts with the support's surface, whereas a decrease in temperature or an increase of H_2 pressure results in a morphological reconstruction from biplanar to a cuboctahedric Pt cluster, since the cuboctahedric structure can adsorb high amounts of hydrogen to form surface hydride species at cost of moderate deformation, thereby weakening the interaction with the support [**37**]. Hydrogen reduction is also one of the means to introduce strong metal support interaction (SMSI) on supported catalyst [**38**]. SMSI describes an interaction of the metal and support, which will lead to the encapsulation of the active component by forming an overlayer via the migration of the supporting material under reducing conditions [**39**]. The SMSI is originally reported by Tauster *et al.* on TiO_2-supported group VIII precious metals: they find that upon higher-temperature reduction treatment (> 500 °C), the chemisorption capacity of H_2 and CO will dramatically decrease to even near zero, due to the migration of reduced titanium oxide onto the metal [**40–42**].

SMSI is also reported for RuO_2-TiO_2-based systems and has been extensively studied by different researchers. Zhang *et al.* prepared RuO_2/TiO_2 catalysts with varying Ru loadings (0.5, 1, 2, 4 wt. %) using an impregnation method, with the aim of investigating the size-dependent metal support interaction in Fischer-Tropsch synthesis. All the catalysts were calcined in air at 300 °C prior to a reduction treatment under H_2 at 450 °C which results in SMSI of Ru/TiO_2 via the formation of a TiO_x coating on the Ru nanoparticles (NPs). By different characterization methods, it is revealed that with increasing Ru loading, the sizes of the Ru NPs slightly increase from 1.58 to 2.24 nm, and the proportion of TiO_x coating gradually decrease, which makes the reduction of the Ru NPs easier. The activity data indicates that the enhanced degree of reduction for large Ru NPs renders the methanation facile, while in case of small Ru NPs, accompanied by an extended TiO_x coating, a preference toward carbon chain growth (C_{5+} hydrocarbons) can be found [**43**]. Subsequently, they explore the effect of reduction temperature on the SMSI and find that SMSI of Ru and TiO_2 controls the surface exposure of Ru NPs. Here, 2.2 wt. % Ru/TiO_2 catalysts are reduced at varying temperatures in H_2 (from 200 to 600 °C). With increasing reduction temperature, the TiO_x thin layer begins to migrate and coat the Ru surface, resulting in a shrinkage of accessible metallic Ru surface, thus leading to a decreased activity in Fischer-Tropsch synthesis [**44**]. In the latest study of the same research group, a new

mechanism for the SMSI formation is proposed (cf. **Figure 1.3**). The conventional way to form SMSI involves metallic Ru NPs being obtained at a low reduction temperature, and then migration of the TiO_x overlayer on the Ru surface upon high-temperature reduction. They claim high-temperature pre-calcination in air of Ru/TiO_2 leads to epitaxial growth of RuO_2 on the rutile TiO_2 support to form a $Ru_xTi_{1-x}O_2$ mixed oxide interphase. Subsequent H_2 treatment pronouncedly facilitates the co-reduction of Ru and Ti, which leads to an enhancement of the TiO_x overlayer on the Ru NPs. Therefore low-temperature reduction of Ru/TiO_2-xAir ($x \geq$ 300 °C) can also lead to SMSIs due to facile co-reduction of the $Ru_xTi_{1-x}O_2$ interphase [**45**]. Zhou *et al.* apply anatase (A-TiO_2) and rutile TiO_2 (R-TiO_2) as supports to investigate the SMSI behavior of Ru/TiO_2 catalysts under varying calcination conditions. It is found that annealing $Ru/R\text{-}TiO_2$ in air can incorporate Ru atoms into the surface lattice of R-TiO_2 to form epitaxial RuO_x species due to the lattice matching between RuO_2 and R-TiO_2. Such interfacial RuO_x species can act as anchoring layers to strongly bind Ru nanoparticles onto R-TiO_2 supports after reduction in hydrogen. Catalytic activity data in CO_2 hydrogenation reaction points to $Ru/R\text{-}TiO_2$-air-H_2 (pre-calcined in air at 400 °C and then reduced in H_2 at 300 °C) exhibiting a much higher activity than $Ru/R\text{-}TiO_2$-H_2 (directly reduced in H_2 at 300 °C). For $RuO_2/A\text{-}TiO_2$, pre-calcination under air and then reduction under hydrogen results a noticeable SMSI, leading to almost no activity in CO_2 conversion [**46**].

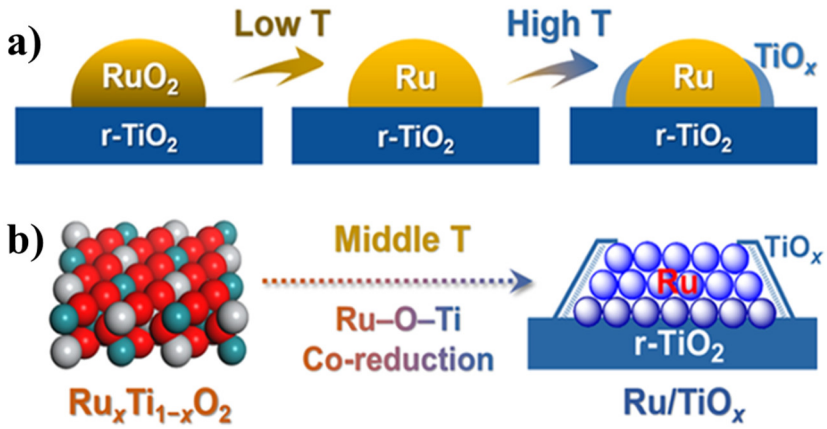

Figure 1.3. (a) Classic support migration mechanism for SMSI formation. (b) Proposed Ru−O−Ti co-reduction mechanism for the facile formation of SMSI. Reprinted with permission from reference [**45**]. Copy right 2022 American Chemical Society.

From the above-mentioned literature, hydrogen treatment and the resulting SMSI provide an additional way to regulate the activity and selectivity of catalysts, thus being a promising approach for real applications. The formation of SMSI normally requires high reduction

temperature, while the interaction between hydrogen and mixed oxides like $Ru_xTi_{1-x}O_2$ at mild temperature (< 300 °C) is still unclear and awaiting to be uncovered.

1.2.2 Interaction of Hydrogen with/on Metal and Metal Oxide

In addition to induce reduction reactions of the metal oxide, the adsorption of hydrogen is also a very important phenomenon which has attracted increasing attention from many researchers. Owing to the small size of H, there is a variety of possible incorporation sites for H. Hence, there are different incorporated species which are (most commonly) discussed in literature: hydride (H^-), proton (H^+) and neutral hydrogen (H^0) [**47, 48**].

Especially, the hydrogen incorporation on metal or metal oxides on the surface/bulk can form stable compounds which hydrogen stays in form of anion (H^-), namely the hydride. In recent decades, (molecular) hydrogen itself is considered to be a cleaner alternative to the traditional fossil fuel, since the latter will cause severe pollutions and global climate change. However, the efficient storage of hydrogen is still a remaining issue for its large-scale application. In this scenario, metal hydrides are widely investigated due to their great potential in energy storage applications [**49, 50**]. Moreover, hydrides have also a wide range of applications in catalytic processes such as hydrogenation/dehydrogenation or reforming reactions. Johnson *et al.* investigate the chemistry of bulk hydrogen in the hydrogenation reaction of CH_3 to CH_4 on a nickel catalyst under ultra-high vacuum (UHV) condition. Via deuterium isotope labelling experiments they demonstrate the hydrogen embedded in the bulk to be the reactive species, while the hydrogen species bound to the surface are unreactive [**51**]. Their finding is further supported by Ledentu *et al.*, whose theoretical study indicates the higher reactivity of the subsurface species to be due to the higher potential energy of the metastable state, resulting in a lower activation barrier for the hydrogenation of the surface adsorbates [**52**]. Palladium hydride complexes are also extensively studied in hydrogenation reactions, for example Teschner *et al.* devise prompt gamma activation analysis (PGAA) to quantify the solubility of hydrogen in a Pd catalyst. The experimental results show that after alkyne hydrogenation reaction the solubility of hydrogen is higher than before the reaction ($PdH_{0.87}$ vs. $PdH_{0.75}$, respectively), which corroborates bulk-dissolved and subsurface hydrogen to be very reactive and participate in unselective hydrogenation as β-hydride species PdH_x ($x > 0.58$) [**53**]. Research by Wilde *et al.* indicates that the hydrogenation of the olefinic double bond requires the presence of weakly bound H species absorbed in the Pd particle volume. Carbon deposition strongly affects the H depth distribution in the Pd particles and promotes persistent hydrogenation activity. The promotion of the sustained hydrogenation by the carbonaceous

deposits is attributed to the facilitation of hydrogen diffusion from the surface into the bulk of the Pd particles, which allows a fast replenishing of the volume-absorbed hydrogen atoms [**54**]. The above research clearly indicates that the adsorbed hydrogen could play a critical role in the catalytic process, while the exact position of the inserted hydrogen still unclear. Usually, owing to its small atomic radius, the absorbed hydrogen occupies the interstitial sites of the parent metal lattice. For Pd hydride, it is assumed that the hydrogen occupies the octahedral interstices (O-sites) in the bulk region [**55, 56**]. However, employing the neutron powder diffraction (NPD) Akiba *et al.* uncovered that there is also a part of hydrogen located at the tetrahedral interstices (T-sites) which probably only limited in the subsurface region [**57, 58**]. Subsequently, Lin *et al.* applied advanced integrated and differentiated differential phase contrast (iDPC and dDPC, respectively), a new imaging technique within aberration-corrected scanning transmission electron microscope (SETM), to acquire a clear view on the hydrogen positions in Pd hydride. The enhanced image contrast directly identifies the hydrogen to atoms occupy the T-sites at the near- surface region of Pd hydrides, while the occupation site gradually changes to the O-site in the bulk, with the transition extended over several atomic layers [**59**].

Contrary to the facile formation of Pd hydrides even at ambient temperature and atmospheric pressure, the ruthenium hydrides demand more critical synthesis conditions: Kuzovnikov *et al.* successfully synthesize Ru monohydride at a hydrogen pressure of about 14 GPa, the hydride formation is accompanied by a phase transition from the original hcp structure of the pristine metal to the fcc structure [**60**]. Besides, some ruthenium hydride complexes are fabricated in organic and aqueous media and applied in homogeneous H_2-hydrogenation reactions [**61–63**].

The interaction of hydrogen with oxides is even more complex than with metals. Hydrogen exposure leads frequently to the formation of surface hydroxyl groups, but can also result in hydrogen incorporation into bulk oxide as proton or hydride species [**47, 49**]. A special case for oxide material to form hydride is CeO_2. For CeO_2, it is widely accepted that dissociatively adsorbed H_2 on ceria will form two surface OH groups which further desorb as water while creating an oxygen vacancy (Ce^{3+}) [**64**]. In 2001 Sohlberg *et al.* carried out first-principles calculations to study the possible uptake of hydrogen by ceria. The calculations suggest that the uptake of hydrogen by ceria to form HCe_4O_8 becomes thermodynamically spontaneous below 665 K. This uptake produces a lattice volume expansion of about 1.5%. The incorporated hydrogen forms hydroxyl structures within the ceria bulk. A “hydride” form where the H is octahedrally coordinated by Ce is assumed to be energetically unstable [**65**]. DFT calculations from García-Melchor *et al.* suggest a heterolytic H_2 dissociation to be kinetically favored on the $CeO_2(111)$ surface to form a Ce–H and a Ce–OH species. The formed Ce–H species further

evolve to the thermodynamically more stable OH species, accompanied by the reduction of Ce^{4+} to Ce^{3+} [**66**]. Based on the above studies, the dissociation of H_2 over CeO_2 could generally involve two mechanisms: one is the homolytic cleavage to form two Ce–OH groups, and the other is heterolytic cleavage to produce Ce–H and Ce–OH [**67**].

In 2012, Vilé *et al.* reported for the first time the hydrogenation reaction of alkynes to olefins over a bulk CeO_2 catalyst. It turns out that that pre-reduced CeO_2 leads to a dramatic decrease in alkyne conversion and alkene selectivity, indicating an excessive degree of surface reduction having a detrimental influence on the catalytic performance. They infer that the oxygen species involved in hydride transfer might differ from the more mobile oxygen species involved in oxidation reactions [**68**]. Subsequently, they investigate the shape-dependent activity of ceria in both CO oxidation and C_2H_2 hydrogenation reaction. The catalytic performance in the oxidation reaction and the hydrogenation reaction show quite inverse structural sensitivities. Ceria exposing the (111) facet reveals a higher hydrogenation activity while the (100) surface dominates in the oxidation reaction. The easier formation of oxygen vacancies of (100) facets might have detrimental influence on the hydrogenation reaction. The authors speculate that the higher hydrogenation activity of the (111) facet could be related to a better stabilization of reactive intermediates [**69**]. To further clarify the origin of outstanding activity and selectivity observed on CeO_2 and to elucidate whether CeO_2 can also store hydrogen below the surface, Werner *et al.* conduct infrared reflection absorption spectroscopy (IRAS) measurements on CeO_2(111) thin films under the exposure of hydrogen molecules in the mbar regime. The data reveals that hydrogen is only located at the surface of stoichiometric CeO_2(111), whereas H incorporates as a volatile species into the volume of partially reduced CeO_{2-x}(111) thin films. Combined with the DFT calculations (cf. **Figure 1.4**), they conclude that oxygen vacancies can facilitate the hydrogen incorporation into the ceria bulk [**70, 71**]. A similar conclusion was also obtained by Wu *et al.*, who observe directly the cerium hydride species (Ce–H) through *in situ* inelastic neutron scattering (INS) spectroscopy. By comparing the INS spectra of the hydrogen treated CeO_2 nanorods with bulk CeH_3 and CeH_2 hydrides as well as the surface hydride on reduced ceria (111), (110), and (100) facets, they conclude that both surface and bulk hydrides co-exist in the reduced CeO_2. These Ce–H species are quite unstable under oxidative conditions and readily react with adsorbed O_2 species to form water. However, the cerium hydrides could be preserved during hydrogenation reaction using high concentration of H_2, maybe serving as active sites evolving in the reaction process [**72**]. Since the Ce–H species are unstable and prone to transform into more stable OH groups or water, the inelastic neutron scattering or neutron

powder diffraction analysis are currently the most effective methods for their characterization [**73**].

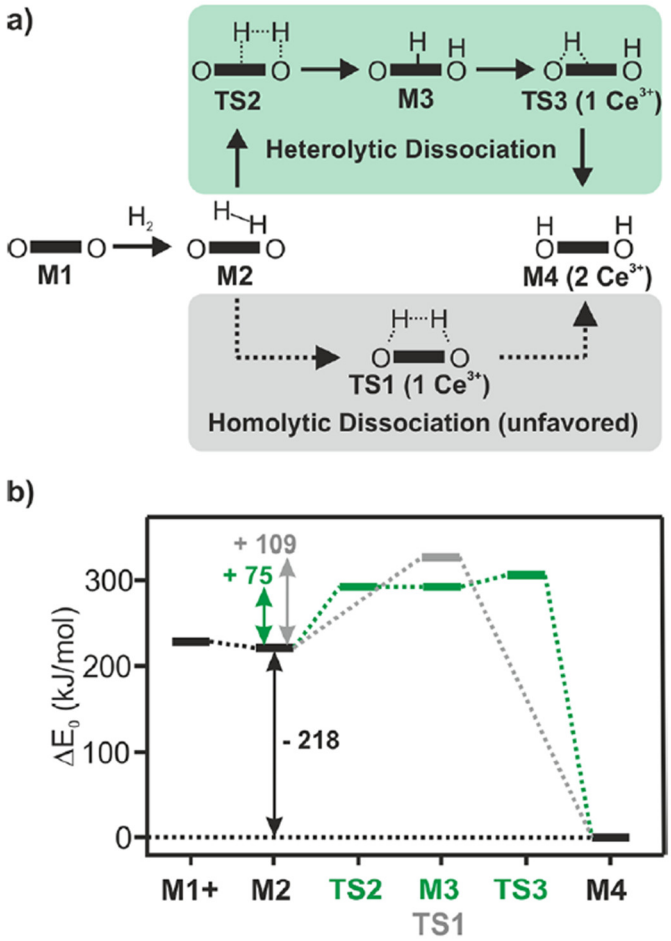

Figure 1.4. (a) Schematic representation of possible homolytic/heterolytic hydrogen dissociation pathways. The bold lines represent Ce ions on the surface, dashed lines represent delocalized electrons. Ce ions are in oxidation state +4 if not stated otherwise. (b) Corresponding energy profile of hydrogen incorporation. The plus sign (M1+) indicates that the reported energy includes gas phase H_2. Reprinted with permission from reference [**70**]. Copy right 2017 American Chemical Society.

Quite in contrast, exposing RuO_2 to hydrogen does not lead to the formation of hydrous RuO_2 or solid suboxides. Thermal treatment under hydrogen at temperatures above 130 °C instead results in the chemical reduction of RuO_2 accompanied by a phase separation into RuO_2 and metallic ruthenium on the nanoscale [**74, 75**]. However, in electrocatalysis hydrogen is assumed to be incorporated as protons to form hydroxide or hydrate species. Krause *et al.* report that anodic polarization of Ru(0001) can form hydrous RuO_2 layers, which will transform into flat metallic Ru islands and RuO_2 particles after annealing at 200 °C [**76**]. Hu *et al.* also fabricate hydrous RuO_2 ($RuO_2{\cdot}xH_2O$) nanotubes by electrodeposition using hydrothermally synthesized

$RuO_2 \cdot xH_2O$ nanocrystallites as precursor [**77**]. Näslund *et al.* report that RuO_2 coatings can transform into ruthenium oxyhydroxide ($RuO(OH)_2$) species under industrial hydrogen evolution conditions, which could be the main reason for the destabilization of the RuO_2 coating [**78**]. Based on DFT calculations, Karlsson *et al.* find that during hydrogen evolution the hydrogen enters the rutile RuO_2 lattice and converts oxygen groups into hydroxyl groups [**79**]. Weber *et al.* discover that cathodic polarization of a single-crystalline RuO_2(110) in an acidic environment will cause proton insertion into the lattice, which ultimately transform RuO_2(110) into a hydrous RuO_2 layer [**80**]. Recently, Yang *et al.* accomplish hydrogen insertion into RuO_2 by a dedicated soft chemical approach based on the water gas shift reaction at temperatures below 200 °C. This approach leads to a monoclinic H_xRuO_2 phase upon insertion of hydrogen into the rutile RuO_2 matrix with superior activity in hydrogenation reactions [**81**]. Dahal *et al.* present a scanning tunneling microscopy (STM) study about the hydrogen adsorption on RuO_2 (110), they observe heterolytical dissociation of hydrogen to hydride-hydroxyl pairs even at 5 K under ultra-high vacuum (UHV) conditions. Low temperature annealing (120 ~ 295 K) will lead hydride species to form bridging hydroxyls, which will ultimately form water under high temperature annealing (450 ~ 600 K) [**82**].

Based on the above literature review, the actual state of incorporated hydrogen among various metal oxides still remains elusive. To establish a clear and comprehensive scaling rule, Ao conducts systematic first-principles calculation to investigate the behavior of uncharged hydrogen in more than 100 different metal oxides. In his calculation, three main hydrogen incorporation sites, namely, interstitial sites, OH groups, and oxygen vacancies, are taken into consideration. H prefers to form OH groups in reducible oxides but occupy interstitial site in the irreducible ones. Furthermore, hydrogen plays a double role by stabilizing oxygen vacancies and promoting the formation of metal hydride species. Therefore, oxygen vacancy formation energy could be identified as the descriptor to scale the present state of hydrogen due to its linear correlation with the H formation energies [**83**].

The hydrogen incorporation behavior would be even more intricate in a binary or ternary metal oxide system, since multiple factors such as redox properties, bonding behavior, or electron state of each component could collectively affect the hydrogen incorporation process, which further exert influence on the catalytic performance of the materials. The hydrogen incorporation in mixed oxides system has rarely been reported in the literature. In this context, exploring the incorporation of hydrogen into mixed oxides, such as Ru-Ti mixed oxides, is of great interest.

1.3 Ruthenium Based Catalyst in Oxidation Catalysis

1.3.1 Application 1: Ru-based Propane Oxidation Catalyst

Catalytic propane oxidation plays a pivotal role in the post-combustion treatment of liquid petroleum gas (LPG) powered engines' exhaust. Ruthenium is known to be one of the most active elements in the activation of C–H and C–C bonds, offering significant potential as a cost-effective alternative to the current commercial Pt-based catalysts due to its lower cost (the average price of ruthenium is around $15,000 per kg from September 1st to October 1st 2023; for comparison, the average price of platinum is about $29,000 per kg from September 1st to October 1st 2023). [**21, 84, 85**].

Okal *et al.* first discovered that a Ru/γ-Al_2O_3 catalyst prepared by high-temperature (> 500 °C) hydrogen reduction exhibits excellent propane oxidation activity, achieving complete propane conversion at 200 °C. They propose that the active component responsible for propane oxidation is non-stoichiometric Ru_xO_y nanoparticles or large metallic Ru particles coated with RuO_2 nanolayers [**86–88**]. Compared to the inert carrier γ-Al_2O_3, CeO_2 exhibits superior oxygen storage capacity with a rapid Ce^{3+}/Ce^{4+} redox cycle, making it a more active alternative. Consequently, Hu *et al.* prepared a Ru/CeO_2 catalyst which achieves full propane conversion at 210 °C. Quite in contrast, under the same experimental conditions, the Ru/Al_2O_3 catalyst requires a higher temperature of 275 °C to reach 100% propane conversion. Characterizations by XPS, CO-TPR and O_2-TPR indicate that the abundant oxygen defects at the Ru-CeO_2 interface facilitate the adsorption and activation of propane molecules, creating an additional pathway for propane combustion and thereby significantly enhancing propane combustion activity [**89**]. Based on these results, Wang *et al.* further increase the oxygen defect concentration at the Ru-CeO_2 interface by optimizing the morphology/facets of the CeO_2 supports (including nanorods, cubes, and octahedrons). Among all, the Ru/CeO_2 nanorods exhibit the highest activity, reducing the total propane conversion temperature even further to 195 °C, surpassing the performance of currently reported Pt-based catalysts [**90**].

However, within oxygen-rich reaction conditions, highly active small RuO_x clusters will be gradually oxidized and sintered, transforming into crystalline, less active RuO_2 particles, ultimately leading to catalyst deactivation [**86**]. Therefore, several researchers have explored and proposed the strategy of introducing a third component in order to stabilize Ru-based catalysts. For example, Ledwa *et al.* employed the reverse micro-emulsion method to synthesize $Ru_xCe_{1-x}O_{2-y}$ particles, which are subsequently loaded onto a γ-Al_2O_3 support. Activity tests

demonstrate that the RuO_x active species can be effectively stabilized at 800 °C [**91, 92**]. Sun *et al.* also prepared unsupported Ru-Ce mixed oxides to increase the stability of the Ru active sites [**93**]. Similarly, Okal et al. synthesized a series of Ru_x-Re_y/γ-Al_2O_3 catalysts, which can achieve 95% propane conversion at 173 °C while maintain stable over 25 hours. It is shown that the strong interaction between the ReO_x species and γ-Al_2O_3 can sufficiently inhibit the agglomeration and sintering of RuO_x species via the physical isolation effect [**94, 95**].

In summary, the sintering and the volatility are obstacles for the industrialization of RuO_2-based catalyst, while the introduction of mixed oxides is a general and low-cost approach to stabilize ruthenium in various combustion reactions which need high temperatures (like propane combustion). In this regard, Ru-Ti mixed oxides emerge as promising catalysts, demonstrating both high activity in various catalytic oxidation reactions and exceptional stability.

1.3.2 Application 2: Ru-based HCl Oxidation Catalyst

The Deacon process, established by Henry Deacon in 1874, is a procedure to recycle the undesired by-product HCl by re-oxidation to chlorine in the chlorine industry where chlorine is used as reactant. Among different catalyst systems, RuO_2-based materials exhibit superior catalytic activity and stability at low temperature. The first report of ruthenium-based catalysts in HCl oxidation can be traced back to the patent from Shell plc in 1964, in which silica gel, alumina, and pumice are selected as supports and loaded with the active ruthenium species, but there was no further pilot test or industrialization reported thereafter [**96**]. Seki from Sumitomo Chemical Industries Co., Ltd. prepared RuO_2 catalysts on different supports (Al_2O_3, SiO_2, anatase-TiO_2 and rutile-TiO_2) via an impregnation method, and evaluated their performance in HCl oxidation reaction. The results show that the structural properties of the support have a significant influence on the catalytic performance. Among them, the RuO_2/ rutile-TiO_2 catalyst shows the best catalytic activity because RuO_2 can epitaxially grows as a thin layer on the surface of rutile TiO_2, thus effectively promoting the catalytic activity. To enhance the thermal stability and prevent the sintering of Ru species of the RuO_2/rutile-TiO_2 catalyst, SiO_2 and RuO_2 were co-impregnated onto the surface of rutile TiO_2. The resulting catalyst exhibits remarkable thermal stability at ~85% conversion over 16,000 hours. It is hypothesized that the inclusion of SiO_2 effectively hinders the growth of Ru particles [**97**]. Xiang *et al.* conduct further research on the RuO_2/TiO_2 catalyst system and discuss the morphology evolution process of RuO_2 nanoparticles on the P25-TiO_2 surface. The experimental results show that there is a size effect in the growth of RuO_2 on TiO_2. RuO_2 particles with a size smaller than 2 nm can transfer to an epitaxial growth layer under Deacon reaction condition, while the larger RuO_2 particles are less

prone to changing their size. Based on thermodynamic simulation, it is speculated that this phenomenon is caused by the surface tension and interfacial lattice matching between the RuO_2 and the TiO_2 [**98**]. Kondratenko *et al.* prepared RuO_2/ rutile-TiO_2 catalyst with much lower Ru content (0.16 wt.%) by an ethylene glycol assisted precipitation method. The obtained catalyst shows comparable activity to the industrially applied 2 wt.% RuO_2/rutile TiO_2 catalysts, while the usage of Ru is significantly reduced, thus lowering the cost of the catalyst. However, due to the complexity of the preparation process, it is challenging to implement it for industrial applications [**99**].

Seitsonen *et al.* established a model of $RuO_2(110)/TiO_2(110)$ and study the reaction mechanism of the RuO_2/TiO_2 catalyst system by DFT calculations. The results show that $RuO_2(110)/TiO_2(110)$ follows the one-dimensional Langmuir-Hinshelwood (L-H) mechanism in HCl oxidation reaction. HCl reacts with oxygen species adsorbed on the TiO_2 surface to generate Cl_2 and H_2O. The recombination of two adsorbed chlorine species to form gaseous Cl_2 is the rate-determining step. When the thickness of RuO_2 is one atomic layer, the Ti in the surface layer of O–Ti–O can be replaced by Ru. The addition of Ru promotes the dissociation of oxygen adsorbed on the TiO_2 surface, thus promoting the activity to a certain extent [**100**]. López *et al.* also study the reaction mechanism of RuO_2/TiO_2 catalyst through DFT calculations and Temporal Analysis of Products (TAP). The results show that the reaction mainly follows the L-H mechanism, the $RuO_{2-x}Cl_x$ generated during the reaction is the active species and the generation of chlorine is the rate-determining step of the reaction, and the production of chlorine is closely related to the coverage of Cl and O on the surface. It is also found that under low O coverage, a trace amount of chlorine can still be produced indicating that surface lattice oxygen can also participate in the reaction through the Mars van Krevelen (M-K) mechanism [**101, 102**].

Pérez-Ramírez *et al.* and Bayer Material Science (BMS) jointly developed a RuO_2/SnO_2-Al_2O_3 catalyst (Ru loading of 2 wt.%) for the HCl oxidation reaction. SnO_2 also reveals a rutile tetragonal phase, the lattice matching between RuO_2 and SnO_2 fosters the epitaxial growth of a film-like RuO_2, resulting in a catalyst that is both highly active and exceptionally durable. The addition of Al_2O_3 hinders the interaction of formed Ru–OH species in the reaction and suppresses the sintering of active phase, further enhancing catalytic stability. Under the experimental conditions of feed gas $HCl:O_2$ = 2:1, W/F_{HCl} = 36.4 g·h/mol (W represents the catalyst mass, F_{HCl} represents the molar flow rate of HCl in the feed gas), T = 553–653 K, the RuO_2/SnO_2-Al_2O_3 catalyst shows a finalized HCl conversion of about 36% and is stable for more than 10,000 hours, thus revealing great potential for practical application [**103, 104**].

Teschner *et al.* combine in situ PGAA, TAP and DFT calculations to study the surface properties of the RuO_2/SnO_2-Al_2O_3 catalyst and the related reaction mechanism. The high-resolution TEM images show that there are two kinds of Ru species, one is RuO_2 particles within 2–4 nm in diameter, and the other is a RuO_2 thin layer with a thickness of 1–3 monolayers. PGAA and TAP experimental results show that the RuO_2/SnO_2-Al_2O_3 catalyst follows the L-H mechanism in the reaction, in which the activation of oxygen is the rate-determining step of the reaction. During the reaction process, the chlorine species adsorbed on the surface of the catalyst can combine with oxygen to form active oxychlorine compounds, so the activity of the reaction is directly related to the oxygen coverage of the catalyst. The DFT results also prove that HCl oxidation reaction is structure sensitive. The activity of a RuO_2 monolayer is higher than that of bilayer $RuO_2(110)/SnO_2(110)$ [**105–108**].

In the Deacon process, the chlorination of the catalyst leads to a severe loss of activity, as observed in copper and ceria-based catalysts. To better predict the catalyst stability under harsh reaction conditions, Hess applies computational models to investigate the catalyst degradation behaviors of 66 elements. Two descriptors including chlorination and volatility of the metal oxides are utilized for screening. It is found that most oxides operated at low conversion are unstable toward chlorination and the formation of volatile compounds, while operated at higher conversion rates, their overall stability is enhanced. However, there is an exception with RuO_2-based catalysts, which are stable (less prone to chlorination or volatilization) even under harsh conditions [**109**]. Over et al. applied a single-crystalline $RuO_2(110)$ model to elucidate the remarkable stability of ruthenium species during HCl oxidation at the atomic level. The results, as derived by high-resolution core-level shift (HRCLS) spectra, thermal desorption spectra (TDS), low-energy electron diffraction (LEED), and temperature-programmed CO oxidation experiments, collectively affirm that the $RuO_2(110)$ surface undergoes chlorination, forming $RuO_{2-x}Cl_x(110)$, when exposed to HCl oxidation conditions. This chlorination process involves the partial replacement of bridging surface oxygen species (O_{br}) with bridging chlorine species (Cl_{br}). Notably, the incorporation of chlorine ceases when Cl_{br} atoms replace most of the O_{br} atoms. Consequently, the chlorination process of RuO_2 (110) appears to be self-limiting. The resulting $RuO_{2-x}Cl_x(110)$ surface, generated by this unique chlorination process, significantly contributes to the exceptional activity and stability of ruthenium-based catalysts in the HCl oxidation reaction [**110–117**].

From the above-mentioned studies, RuO_2 is found to be not bulk-chlorinated under reaction conditions and to have a not very volatile chloride, while the only remaining issue is that RuO_2 is prone to form volatile RuO_4 at high temperatures and highly oxidizing conditions. Leaching

of RuO_4 has been proposed to deactivate RuO_2-based Deacon catalysts at high reaction temperatures. The volatilization of RuO_2 may possibly begin with morphological changes such as mobilizing or sintering on the support surface, here, a good approach to stabilize ruthenium is the formation of mixed oxides such as $Ru_xTi_{1-x}O_2$. Kanzler *et al.* prepared pure RuO_2 and RuO_2-TiO_2 nanofibers via electrospinning. They observe that pure RuO_2 nanofibers suffer from severe sintering and intergrowth of the fibers, concomitant with a complete loss of the fiber geometry after 10 hours of the stability test in mild condition (cf. **Figure 1.5)**. Nevertheless, mixed $Ru_{0.15}Ti_{0.85}O_2$ with the same fiber geometry does not show any degradation and morphological variation while exhibiting comparable activity under the same conditions [**20**]. A possible explanation is that the bridging chlorine atoms may be stabilized if the attached Ru atoms are replaced by Ti [**115, 118**].

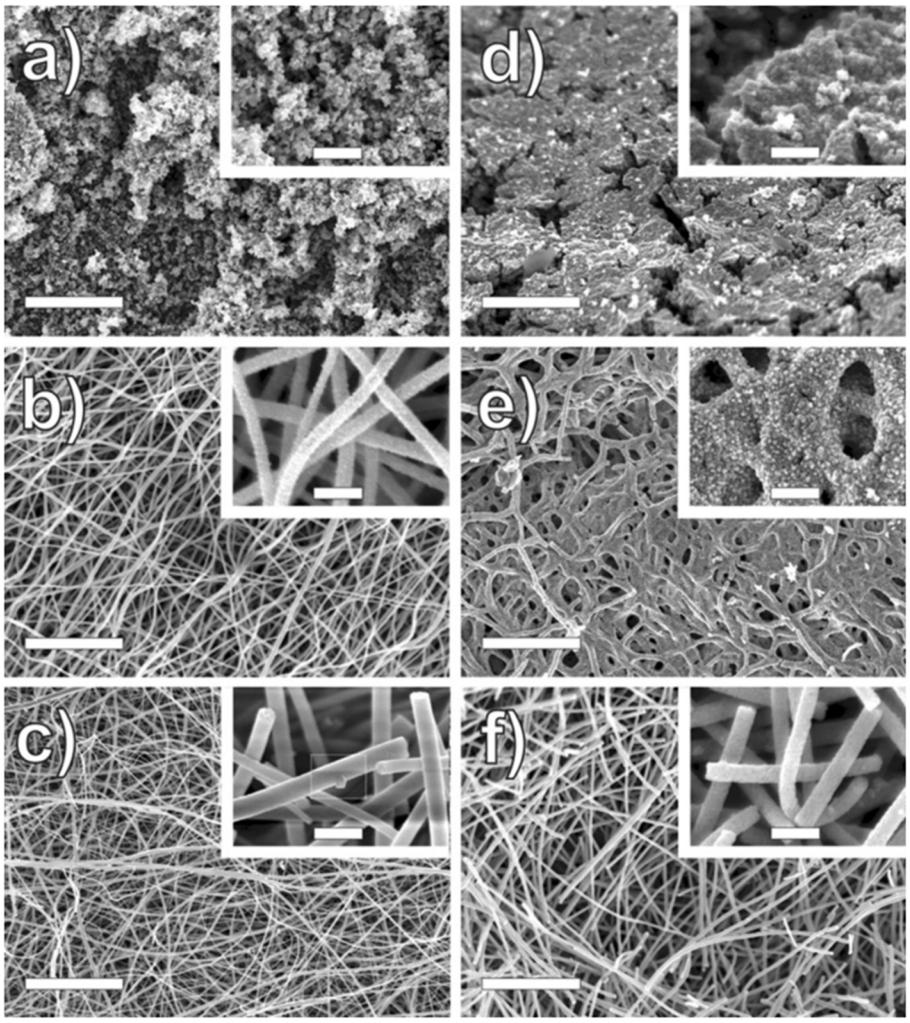

Figure 1.5. Comparison of morphological changes of three different RuO_2 catalysts under atmospheric pressure Deacon reaction conditions at 573 K and a reaction feed $HCl/O_2/Ar$ = 2:2:6 at a flow rate of 15 mL/min. Left column: model catalysts as prepared (a-c), right column: after reaction (d-f); a, d) RuO_2 powder; b, e) Electrospun RuO_2 nanofibers; c, f) Electrospun $Ru_{0.15}Ti_{0.85}O_2$ mixed oxide nanofibers. Large scale bars 5 μm, small scale bars in the insets 0.5 μm. Reprinted with permission from reference [**20**]. Copy right 2013 John Wiley and Sons.

In this context, ruthenium-based catalysts exhibit outstanding activity and durability in HCl oxidation. Moreover, the mechanisms behind industrial RuO_2/SiO_2/rutile-TiO_2 and RuO_2/SnO_2-Al_2O_3 catalysts have been thoroughly elucidated. Nevertheless, ruthenium-based systems continue to deal with several complex challenges, one of which is the persisting stability issue arising from the potential formation of volatile RuO_4 at elevated hot-spot temperatures during the practical conditions. Hence, further optimization of ruthenium-based catalysts is still required.

1.4 Motivation

As mentioned in **section 1.1.2**, there are contradictory reports on the synthesis of the phase pure Ru-Ti mixed oxides, the solid solution limit/solubility of ruthenium and titanium into each other's oxide phase has also not been clarified yet. Besides, it is indicated that the synthesis method also plays an important role in the final state of the Ru-Ti mixed oxides as well. From these perspectives, we first prepare the Ru-Ti mixed oxides with varying compositions at full range by the conventional sol-gel method which is mostly reported in the literature. State-of-the-art characterization techniques such as N_2 physisorption experiments, XRD, XPS, TG-MS and HR-TEM are then applied in order to acquire the structural and electronic changes when varying the Ru and Ti compositions. Subsequently, we choose the propane oxidation reaction to explore the potential application of the Ru-Ti mixed oxides in thermal catalysis. According to the activity results, the relationship between the composition x and the catalytic propane oxidation activity is obtained. We further examine the hydrogenation behavior over $Ru_xTi_{1-x}O_2$ at 250 °C and compare the catalytic propane oxidation activity with that of the corresponding hydrogenated catalysts. We quantitatively obtain the amount of hydrogen incorporated into the lattice of $Ru_xTi_{1-x}O_2$ via TG-MS. More details are presented in **Chapter 2.1**.

Neither RuO_2 nor rutile-TiO_2 is able to incorporate hydrogen into the lattice just by hydrogen exposure at elevated temperatures. RuO_2 is thermally unstable and will transfer into metal under hydrogen treatment, while TiO_2 is less reducible under hydrogen exposure, unless the temperature is higher than 600 °C, with the formation of titanium suboxides (Ti_nO_{2n-1}), namely the Magneli phases. However, the hydrogen incorporation behavior is still under debate for the Ru-Ti mixed oxides, which a reducible oxide with a (non or) less reducible oxide may possibly incorporate substantial amounts of hydrogen by the simple exposure to H_2 at mild temperatures. Using advanced techniques such as XRD, XPS, aberration-corrected HAADF-STEM, and TG-MS, we investigate the structural and electronic changes that occur when pretreating the Ru-Ti mixed oxides under hydrogen/air at elevated temperatures. Additionally, we quantitatively determine the amount of hydrogen that is incorporated into the lattice. Furthermore, the effect of hydrogen insertion on the propane oxidation and HCl oxidation reactions was also tested. More details are presented in **Chapter 2.2**.

1.5 Reference

1. Misono, M., Heterogeneous Catalysis of Mixed Oxides: Perovskite and Heteropoly Catalysts. Newnes: 2013.
2. Wallington, T.; Kaiser, E.; Farrell, J., Automotive Fuels and Internal Combustion Engines: A Chemical Perspective. Chemical Society Reviews 2006, 35, 335–347.
3. Twigg, M. V., Progress and Future Challenges in Controlling Automotive Exhaust Gas Emissions. Applied Catalysis B: Environmental 2007, 70, 2–15.
4. Wachs, I. E., Recent Conceptual Advances in the Catalysis Science of Mixed Metal Oxide Catalytic Materials. Catalysis Today 2005, 100, 79–94.
5. Védrine, J. C., Heterogeneous Catalysis on Metal Oxides. Catalysts 2017, 7, 341.
6. Wachs, I. E.; Routray, K., Catalysis Science of Bulk Mixed Oxides. ACS Catalysis 2012, 2, 1235–1246.
7. Golunski, S. E.; Hatcher, H. A.; Rajaram, R. R.; Truex, T. J., Origins of Low-temperature Three-way Activity in Pt/CeO_2. Applied Catalysis B: Environmental 1995, 5, 367–376.
8. Kašpar, J.; Fornasiero, P.; Graziani, M., Use of CeO_2-based Oxides in the Three-way Catalysis. Catalysis Today 1999, 50, 285–298.
9. Andana, T.; Piumetti, M.; Bensaid, S.; Russo, N.; Fino, D.; Pirone, R., Nanostructured Ceria-praseodymia Catalysts for Diesel Soot Combustion. Applied Catalysis B: Environmental 2016, 197, 125–137.
10. Fernández-Garcıa, M.; Martınez-Arias, A.; Iglesias-Juez, A.; Hungrıa, A.; Anderson, J.; Conesa, J.; Soria, J., New $Pd/Ce_xZr_{1-x}O_2/Al_2O_3$ Three-way Catalysts Prepared by Microemulsion: Part 1. Characterization and Catalytic Behavior for CO Oxidation. Applied Catalysis B: Environmental 2001, 31, 39–50.
11. Li, C.; Sun, Y.; Hess, F.; Djerdj, I.; Sann, J.; Voepel, P.; Cop, P.; Guo, Y.; Smarsly, B. M.; Over, H., Catalytic HCl Oxidation Reaction: Stabilizing Effect of Zr-doping on CeO_2 Nano-rods. Applied Catalysis B: Environmental 2018, 239, 628-635.
12. Trovarelli, A., Catalysis by Ceria and Related Materials. World Scientific: 2002; Vol. 2.
13. Over, H., Surface Chemistry of Ruthenium Dioxide in Heterogeneous Catalysis and Electrocatalysis: From Fundamental to Applied Research. Chemical Reviews 2012, 112, 3356–3426.
14. Seki, K.; Hibi, T.; Issoh, K.; Suzuta, T.; Nakada, M.; Mori, Y.; Abe, T., The Development of Improved Hydrogen Chloride Oxidation Process. Sumitomo Kagaku 2004, 2004, 1–11.
15. Hibi, T.; Nishida, H.; Abekawa, H., Process for Producing Chlorine. US5871707. 1999.
16. Suen, N.-T.; Hung, S.-F.; Quan, Q.; Zhang, N.; Xu, Y.-J.; Chen, H. M., Electrocatalysis for the Oxygen Evolution Reaction: Recent Development and Future Perspectives. Chemical Society Reviews 2017, 46, 337–365.
17. Wang, C.; Jin, L.; Shang, H.; Xu, H.; Shiraishi, Y.; Du, Y., Advances in Engineering RuO_2 Electrocatalysts towards Oxygen Evolution Reaction. Chinese Chemical Letters 2021, 32, 2108–2116.

18. Over, H., Fundamental Studies of Planar Single-crystalline Oxide Model Electrodes (RuO_2, IrO_2) for Acidic Water Splitting. ACS Catalysis 2021, 11, 8848–8871.
19. Trasatti, S., Electrocatalysis: Understanding the Success of DSA®. Electrochimica Acta 2000, 45, 2377–2385.
20. Kanzler, C. H.; Urban, S.; Zalewska-Wierzbicka, K.; Hess, F.; Rohrlack, S. F.; Wessel, C.; Ostermann, R.; Hofmann, J. P.; Smarsly, B. M.; Over, H., Electrospun Metal Oxide Nanofibres for the Assessment of Catalyst Morphological Stability under Harsh Reaction Conditions. ChemCatChem 2013, 5, 2621–2626.
21. Johnson Matthey. *PGM management*. https://matthey.com/products-and-markets/pgms-and-circularity/pgm-management (accessed 2023-10-19).
22. Yang, C.; Zhao, Z. Y., Stable Structure and Electronic Properties of $Ru_{1-x}Ti_xO_2$ Rutile Type Solid Solutions from DFT Calculations. Journal of the American Ceramic Society 2019, 102, 4976–4989.
23. Gerrard, W.; Steele, B., Microstructural Investigations on Mixed RuO_2-TiO_2 Coatings. Journal of Applied Electrochemistry 1978, 8, 417–425.
24. Duvigneaud, P.-H.; Coussement, A., Effect of Chlorine on Solid Solution Formation in Ruthenium Titanium Dioxide Coatings. Journal of Solid State Chemistry 1984, 52, 22–31.
25. Guglielmi, M.; Colombo, P.; Rigato, V.; Battaglin, G.; Boscolo-Boscoletto, A.; DeBattisti, A., Compositional and Microstructural Characterization of RuO_2-TiO_2 Catalysts Synthesized by the Sol-gel Method. Journal of the Electrochemical Society 1992, 139, 1655.
26. Kameyama, K.; Shohji, S.; Onoue, S.; Nishimura, K.; Yahikozawa, K.; Takasu, Y., Preparation of Ultrafine RuO_2-TiO_2 Binary Oxide Particles by a Sol-gel Process. Journal of the Electrochemical Society 1993, 140, 1034.
27. Osman, J. R.; Crayston, J. A.; Pratt, A.; Richens, D. T., RuO_2-TiO_2 Mixed Oxides Prepared from the Hydrolysis of the Metal Alkoxides. Materials Chemistry and Physics 2008, 110, 256–262.
28. Málek, J.; Watanabe, A.; Mitsuhashi, T., Sol-gel Preparation of Rutile Type Solid Solution in TiO_2-RuO_2 System. Journal of Thermal Analysis and Calorimetry 2000, 60, 699–705.
29. Colomer, M.; Velasco, M. J.; Jurado, J., Synthesis and Thermal Evolution of TiO_2-RuO_2 Xerogels. Journal of Sol-gel Science and Technology 2006, 39, 211–222.
30. Morais, E.; O'Modhrain, C.; Thampi, K. R.; Sullivan, J. A., RuO_2/TiO_2 Photocatalysts Prepared via a Hydrothermal Route: Influence of the Presence of TiO_2 on the Reactivity of RuO_2 in the Artificial Photosynthesis Reaction. Journal of Catalysis 2021, 401, 288–296.
31. Dória, A. R.; Gonzaga, I. M.; Santos, G. O.; Pupo, M.; Silva, D. C.; Silva, R. S.; Rodrigo, M. A.; Eguiluz, K. I.; Salazar-Banda, G. R., Ultra-fast Synthesis of Ti/$Ru_{0.3}Ti_{0.7}O_2$ Anodes with Superior Electrochemical Properties Using an Ionic Liquid and Laser Calcination. Chemical Engineering Journal 2021, 416, 129011.

32. Hrovat, M.; Holc, J.; Samardžija, Z.; Dražič, G., The Extent of Solid Solubility in the RuO_2-TiO_2 System. Journal of materials research 1996, 11, 727–732.
33. Jacob, K.; Subramanian, R., Phase Diagram for the System RuO_2-TiO_2 in Air. Journal of Phase Equilibria and Diffusion 2008, 29, 136–140.
34. Wang, X.; Shao, Y.; Liu, X.; Tang, D.; Wu, B.; Tang, Z.; Wang, X.; Lin, W., Phase Stability and Phase Structure of Ru–Ti–O Complex Oxide Electrocatalyst. Journal of the American Ceramic Society 2015, 98, 1915–1924.
35. Yakovina, O. A.; Lisitsyn, A. S., Probing the H_2-induced Restructuring of Pt Nanoclusters by H_2-TPD. Langmuir 2016, 32, 12013–12021.
36. Vottero, E.; Carosso, M.; Ricchebuono, A.; Jiménez-Ruiz, M.; Pellegrini, R.; Chizallet, C.; Raybaud, P.; Groppo, E.; Piovano, A., Evidence for H_2-induced Ductility in a Pt/Al_2O_3 Catalyst. ACS Catalysis 2022, 12, 5979–5989.
37. Mager-Maury, C.; Bonnard, G.; Chizallet, C.; Sautet, P.; Raybaud, P., H_2-induced Reconstruction of Supported Pt Clusters: Metal-support Interaction versus Surface Hydride. ChemCatChem 2011, 3, 200–207.
38. Pu, T.; Zhang, W.; Zhu, M., Engineering Heterogeneous Catalysis with Strong Metal-support Interactions: Characterization, Theory and Manipulation. Angewandte Chemie International Edition 2023, 62, e202212278.
39. Tauster, S., Strong Metal-support Interactions. Accounts of Chemical Research 1987, 20, 389–394.
40. Tauster, S.; Fung, S.; Baker, R.; Horsley, J., Strong Interactions in Supported-metal Catalysts. Science 1981, 211, 1121–1125.
41. Tauster, S.; Fung, S.; Garten, R. L., Strong Metal-support Interactions. Group 8 Noble Metals Supported on Titanium Dioxide. Journal of the American Chemical Society 1978, 100, 170–175.
42. Tauster, S.; Fung, S., Strong Metal-support Interactions: Occurrence among the Binary Oxides of Groups IIA–VB. Journal of Catalysis 1978, 55, 29–35.
43. Zhang, Y.; Su, X.; Li, L.; Qi, H.; Yang, C.; Liu, W.; Pan, X.; Liu, X.; Yang, X.; Huang, Y., Ru/TiO_2 Catalysts with Size-dependent Metal/Support Interaction for Tunable Reactivity in Fischer-Tropsch Synthesis. ACS Catalysis 2020, 10, 12967–12975.
44. Zhang, Y.; Yang, X.; Yang, X.; Duan, H.; Qi, H.; Su, Y.; Liang, B.; Tao, H.; Liu, B.; Chen, D., Tuning Reactivity of Fischer-Tropsch Synthesis by Regulating TiO_x Overlayer over Ru/TiO_2 Nanocatalysts. Nature Communications 2020, 11, 3185.
45. Zhang, Y.; Yan, W.; Qi, H.; Su, X.; Su, Y.; Liu, X.; Li, L.; Yang, X.; Huang, Y.; Zhang, T., Strong Metal-Support Interaction of Ru on TiO_2 Derived from the Co-Reduction Mechanism of $Ru_xTi_{1-x}O_2$ Interphase. ACS Catalysis 2022, 12, 1697–1705.
46. Zhou, J.; Gao, Z.; Xiang, G.; Zhai, T.; Liu, Z.; Zhao, W.; Liang, X.; Wang, L., Interfacial Compatibility Critically Controls Ru/TiO_2 Metal-Support Interaction Modes in CO_2 Hydrogenation. Nature Communications 2022, 13, 327.
47. Norby, T.; Widerøe, M.; Glöckner, R.; Larring, Y., Hydrogen in Oxides. Dalton Transactions 2004, 3012–3018.

48. Van de Walle, C. G.; Neugebauer, J., Universal Alignment of Hydrogen Levels in Semiconductors, Insulators and Solutions. Nature 2003, 423, 626–628.
49. Coperet, C.; Estes, D. P.; Larmier, K.; Searles, K., Isolated Surface Hydrides: Formation, Structure, and Reactivity. Chemical reviews 2016, 116, 8463–8505.
50. Schneemann, A.; White, J. L.; Kang, S.; Jeong, S.; Wan, L. F.; Cho, E. S.; Heo, T. W.; Prendergast, D.; Urban, J. J.; Wood, B. C., Nanostructured Metal Hydrides for Hydrogen Storage. Chemical reviews 2018, 118, 10775–10839.
51. Johnson, A.; Daley, S.; Utz, A.; Ceyer, S., The Chemistry of Bulk Hydrogen: Reaction of Hydrogen Embedded in Nickel with Adsorbed CH_3. Science 1992, 257, 223–225.
52. Ledentu, V.; Dong, W.; Sautet, P., Heterogeneous Catalysis through Subsurface Sites. Journal of the American Chemical Society 2000, 122, 1796–1801.
53. Teschner, D.; Borsodi, J.; Wootsch, A.; Révay, Z.; Havecker, M.; Knop-Gericke, A.; Jackson, S. D.; Schlögl, R., The Roles of Subsurface Carbon and Hydrogen in Palladium-catalyzed Alkyne Hydrogenation. Science 2008, 320, 86–89.
54. Wilde, M.; Fukutani, K.; Ludwig, W.; Brandt, B.; Fischer, J. H.; Schauermann, S.; Freund, H. J., Influence of Carbon Deposition on the Hydrogen Distribution in Pd Nanoparticles and their Reactivity in Olefin Hydrogenation. Angewandte Chemie International Edition 2008, 47, 9289–9293.
55. Worsham Jr, J.; Wilkinson, M.; Shull, C., Neutron-diffraction Observations on the Palladium-hydrogen and Palladium-deuterium Systems. Journal of Physics and Chemistry of Solids 1957, 3, 303–310.
56. Flanagan, T. B.; Oates, W., The Palladium-hydrogen System. Annual Review of Materials Science 1991, 21, 269–304.
57. Ishimoto, T.; Koyama, M., Theoretical Study of Tetrahedral Site Occupation by Hydrogen in Pd Nanoparticles. The Journal of Chemical Physics 2018, 148.
58. Akiba, H.; Kofu, M.; Kobayashi, H.; Kitagawa, H.; Ikeda, K.; Otomo, T.; Yamamuro, O., Nanometer-size Effect on Hydrogen Sites in Palladium Lattice. Journal of the American Chemical Society 2016, 138, 10238–10243.
59. Lin, B.; Wu, X.; Xie, L.; Kang, Y.; Du, H.; Kang, F.; Li, J.; Gan, L., Atomic Imaging of Subsurface Interstitial Hydrogen and Insights into Surface Reactivity of Palladium Hydrides. Angewandte Chemie International Edition 2020, 59, 20348–20352.
60. Kuzovnikov, M.; Tkacz, M., Synthesis of Ruthenium Hydride. Physical Review B 2016, 93, 064103.
61. Shvo, Y.; Czarkie, D.; Rahamim, Y.; Chodosh, D. F., A New Group of Ruthenium Complexes: Structure and Catalysis. Journal of the American Chemical Society 1986, 108, 7400–7402.
62. Ford, P. C., The Water Gas Shift Reaction: Homogeneous Catalysis by Ruthenium and Other Metal Carbonyls. Accounts of Chemical Research 1981, 14, 31–37.
63. Clapham, S. E.; Hadzovic, A.; Morris, R. H., Mechanisms of the H_2-hydrogenation and Transfer Hydrogenation of Polar Bonds Catalyzed by Ruthenium Hydride Complexes. Coordination Chemistry Reviews 2004, 248, 2201–2237.

64. Binet, C.; Daturi, M.; Lavalley, J.-C., IR Study of Polycrystalline Ceria Properties in Oxidised and Reduced States. Catalysis Today 1999, 50, 207–225.
65. Sohlberg, K.; Pantelides, S. T.; Pennycook, S. J., Interactions of Hydrogen with CeO_2. Journal of the American Chemical Society 2001, 123, 6609–6611.
66. García-Melchor, M.; López, N., Homolytic Products from Heterolytic Paths in H_2 Dissociation on Metal Oxides: the Example of CeO_2. The Journal of Physical Chemistry C 2014, 118, 10921–10926.
67. Fernández-Torre, D.; Carrasco, J.; Ganduglia-Pirovano, M. V.; Pérez, R., Hydrogen Activation, Diffusion, and Clustering on CeO_2(111): A DFT+*U* Study. The Journal of Chemical Physics 2014, 141.
68. Vilé, G.; Bridier, B.; Wichert, J.; Pérez-Ramírez, J., Ceria in Hydrogenation Catalysis: High Selectivity in the Conversion of Alkynes to Olefins. Angewandte Chemie International Edition 2012, 124, 8748–8751.
69. Vilé, G.; Colussi, S.; Krumeich, F.; Trovarelli, A.; Pérez-Ramírez, J., Opposite Face Sensitivity of CeO_2 in Hydrogenation and Oxidation Catalysis. Angewandte Chemie International Edition 2014, 53, 12069–12072.
70. Werner, K.; Weng, X.; Calaza, F.; Sterrer, M.; Kropp, T.; Paier, J.; Sauer, J.; Wilde, M.; Fukutani, K.; Shaikhutdinov, S., Toward an Understanding of Selective Alkyne Hydrogenation on Ceria: on the Impact of O Vacancies on H_2 Interaction with CeO_2(111). Journal of the American Chemical Society 2017, 139, 17608–17616.
71. Li, Z.; Werner, K.; Qian, K.; You, R.; Płucienik, A.; Jia, A.; Wu, L.; Zhang, L.; Pan, H.; Kuhlenbeck, H., Oxidation of Reduced Ceria by Incorporation of Hydrogen. Angewandte Chemie International Edition 2019, 58, 14686–14693.
72. Wu, Z.; Cheng, Y.; Tao, F.; Daemen, L.; Foo, G. S.; Nguyen, L.; Zhang, X.; Beste, A.; Ramirez-Cuesta, A. J., Direct Neutron Spectroscopy Observation of Cerium Hydride Species on a Cerium Oxide Catalyst. Journal of the American Chemical Society 2017, 139, 9721–9727.
73. Matsukawa, T.; Iida, K.; Nakamura, M.; Ishigaki, T., Detection of Hydroxyl and Hydride Functional Groups in a Ceria Crystal under Hydrogen Reduction. CrystEngComm 2021, 23, 2355–2359.
74. He, Y.; Knapp, M.; Lundgren, E.; Over, H., Ru(0001) Model Catalyst under Oxidizing and Reducing Reaction Conditions: in-situ High-pressure Surface X-ray Diffraction Study. The Journal of Physical Chemistry B 2005, 109, 21825–21830.
75. Over, H.; Knapp, M.; Lundgren, E.; Seitsonen, A.; Schmid, M.; Varga, P., Visualization of Atomic Processes on Ruthenium Dioxide using Scanning Tunneling Microscopy. ChemPhysChem 2004, 5, 167–174.
76. Krause, P. P.; Camuka, H.; Leichtweiss, T.; Over, H., Temperature-induced Transformation of Electrochemically Formed Hydrous RuO_2 Layers over Ru(0001) Model Electrodes. Nanoscale 2016, 8, 13944–13953.
77. Hu, C.-C.; Liu, M.-J.; Chang, K.-H., Anodic Deposition of Hydrous Ruthenium Oxide for Supercapacitors. Journal of Power Sources 2007, 163, 1126–1131.

78. Näslund, L.-Å.; Ingason, Á. S.; Holmin, S.; Rosen, J., Formation of $RuO(OH)_2$ on RuO_2-Based Electrodes for Hydrogen Production. The Journal of Physical Chemistry C 2014, 118, 15315–15323.
79. Karlsson, R. K.; Cornell, A.; Pettersson, L. G., Structural Changes in RuO_2 during Electrochemical Hydrogen Evolution. The Journal of Physical Chemistry C 2016, 120, 7094–7102.
80. Weber, T.; Abb, M. J. S.; Khalid, O.; Pfrommer, J.; Carla, F.; Znaiguia, R.; Vonk, V.; Stierle, A.; Over, H. In Situ Studies of the Electrochemical Reduction of a Supported Ultrathin Single-Crystalline RuO_2(110) Layer in an Acidic Environment. The Journal of Physical Chemistry C 2019, 123, 3979–3987.
81. Yang, H. J.; Redington, M.; Miller, D. P.; Zurek, E.; Kim, M.; Yoo, C.-S.; Lim, S. Y.; Cheong, H.; Chae, S.-A.; Ahn, D., New Monoclinic Ruthenium Dioxide with Highly Selective Hydrogenation Activity. Catalysis Science & Technology 2022, 12, 6556–6565.
82. Dahal, A.; Mu, R.; Lyubinetsky, I.; Dohnálek, Z., Hydrogen Adsorption and Reaction on RuO_2(110). Surface Science 2018, 677, 264–270.
83. Ao, B., Scaling the Existence state of Hydrogen in Metal Binary Oxides. Acta Materialia 2021, 203, 116463.
84. Wang, Z.; Wang, W.; Khalid, O.; Weber, T.; Spriewald Luciano, A.; Zhan, W.; Smarsly, B. M.; Over, H., Supported $Ru_xIr_{1-x}O_2$ Mixed Oxides Catalysts for Propane Combustion: Resistance against Water Poisoning. ChemCatChem 2022, 14, e202200149.
85. Freyschlag, C. G.; Madix, R. J., Precious Metal Magic: Catalytic Wizardry. Materials Today 2011, 14, 134–142.
86. Okal, J.; Zawadzki, M., Influence of Catalyst Pretreatments on Propane Oxidation Over Ru/γ-Al_2O_3. Catalysis Letters 2009, 132, 225–234.
87. Okal, J.; Zawadzki, M.; Krajczyk, L., Light Alkane Oxidation over Ru Supported on $ZnAl_2O_4$, CeO_2 and Al_2O_3. Catalysis Today 2011, 176, 173–176.
88. Okal, J.; Zawadzki, M., Combustion of Propane over Novel Zinc Aluminate-supported Ruthenium Catalysts. Applied Catalysis B: Environmental 2011, 105, 182–190.
89. Hu, Z.; Wang, Z.; Guo, Y.; Wang, L.; Guo, Y.; Zhang, J.; Zhan, W., Total Oxidation of Propane over a Ru/CeO_2 Catalyst at Low Temperature. Environmental Science & Technology 2018, 52, 9531–9541.
90. Wang, Z.; Huang, Z.; Brosnahan, J. T.; Zhang, S.; Guo, Y.; Guo, Y.; Wang, L.; Wang, Y.; Zhan, W., Ru/CeO_2 Catalyst with Optimized CeO_2 Support Morphology and Surface Facets for Propane Combustion. Environmental Science & Technology 2019, 53, 5349–5358.
91. Ledwa, K. A.; Pawlyta, M.; Kępiński, L., $Ru_xCe_{1-x}O_{2-y}$ Nanoparticles Deposited on Functionalized γ-Al_2O_3 as a Thermally Stable Oxidation Catalyst. Applied Catalysis B: Environmental 2018, 230, 135–144.
92. Ledwa, K. A.; Kępiński, L.; Ptak, M.; Szukiewicz, R., $Ru_{0.05}Ce_{0.95}O_{2-y}$ Deposited on Functionalized Alumina as a Smart Catalyst for Propane Oxidation. Applied Catalysis B: Environmental 2020, 274, 119090.

93. Sun, Y.; Ye, F.; Ding, J.; Li, J.; Guo, Y.; Wang, L.; Guo, Y.; Dai, S.; Zhan, W., Regulating the Spatial Distribution of Ru Nanoparticles on CeO_2 Support for Enhanced Propane Oxidation. ACS Applied Nano Materials 2022, 5, 3937–3945.
94. Baranowska, K.; Okal, J., Bimetallic Ru-Re/γ-Al_2O_3 Catalysts for the Catalytic Combustion of Propane: Effect of the Re Addition. Applied Catalysis A: General 2015, 499, 158–167.
95. Adamska, K.; Okal, J.; Tylus, W., Stable Bimetallic Ru-Mo/Al_2O_3 Catalysts for the Light Alkane Combustion: Effect of the Mo Addition. Applied Catalysis B: Environmental 2019, 246, 180–194.
96. Heemskerk, J.; Stuiver, J. C. M., Process for the Production of Chlorine from Hydrogen Chloride. DE1567788C3. 1964.
97. Seki, K., Development of RuO_2/rutile-TiO_2 Catalyst for Industrial HCl Oxidation Process. Catalysis Surveys from Asia 2010, 14, 168–175.
98. Xiang, G.; Shi, X.; Wu, Y.; Zhuang, J.; Wang, X., Size Effects in Atomic-level Epitaxial Redistribution Process of RuO_2 over TiO_2. Scientific Reports 2012, 2, 801.
99. Kondratenko, E. V.; Amrute, A. P.; Pohl, M.-M.; Steinfeldt, N.; Mondelli, C.; Pérez-Ramírez, J., Superior Activity of Rutile-supported Ruthenium Nanoparticles for HCl Oxidation. Catalysis Science & Technology 2013, 3, 2555–2558.
100. Seitsonen, A.; Over, H., Oxidation of HCl over TiO_2-supported RuO_2: A Density Functional Theory Study. The Journal of Physical Chemistry C 2010, 114, 22624–22629.
101. López, N.; Gómez-Segura, J.; Marín, R. P.; Perez-Ramirez, J., Mechanism of HCl Oxidation (Deacon Process) over RuO_2. Journal of Catalysis 2008, 255, 29–39.
102. Hevia, M. A.; Amrute, A. P.; Schmidt, T.; Pérez-Ramírez, J., Transient Mechanistic Study of the Gas-phase HCl Oxidation to Cl_2 on Bulk and Supported RuO_2 Catalysts. Journal of Catalysis 2010, 276, 141–151.
103. Mondelli, C.; Amrute, A. P.; Krumeich, F.; Schmidt, T.; Pérez-Ramírez, J., Shaped RuO_2/SnO_2-Al_2O_3 Catalyst for Large-Scale Stable Cl_2 Production by HCl Oxidation. ChemCatChem 2011, 3, 657–660.
104. Amrute, A. P.; Mondelli, C.; Schmidt, T.; Hauert, R.; Pérez-Ramírez, J., Industrial RuO_2-Based Deacon Catalysts: Carrier Stabilization and Active Phase Content Optimization. ChemCatChem 2013, 5, 748–756.
105. Teschner, D.; Novell-Leruth, G.; Farra, R.; Knop-Gericke, A.; Schlögl, R.; Szentmiklosi, L.; Hevia, M. G.; Soerijanto, H.; Schomäcker, R.; Perez-Ramirez, J., In situ Surface Coverage Analysis of RuO_2-catalysed HCl Oxidation Reveals the Entropic Origin of Compensation in Heterogeneous Catalysis. Nature chemistry 2012, 4, 739–745.
106. Teschner, D.; Farra, R.; Yao, L.; Schlögl, R.; Soerijanto, H.; Schomäcker, R.; Schmidt, T.; Szentmiklósi, L.; Amrute, A. P.; Mondelli, C., An Integrated Approach to Deacon Chemistry on RuO_2-based Catalysts. Journal of catalysis 2012, 285, 273–284.
107. Amrute, A. P.; Mondelli, C.; Hevia, M. A.; Pérez-Ramírez, J., Temporal Analysis of Products Study of HCl Oxidation on Copper-and Ruthenium-based Catalysts. The Journal of Physical Chemistry C 2011, 115, 1056–1063.

108. Amrute, A. P.; Mondelli, C.; Hevia, M. A.; Pérez-Ramírez, J., Mechanism-performance Relationships of Metal Oxides in Catalyzed HCl Oxidation. ACS Catalysis 2011, 1, 583–590.
109. Hess, F., Is There a Stable Deacon Catalyst? Computational Screening Approach for the Stability of Oxide Catalysts under Harsh Conditions. ACS Catalysis 2021, 497–511.
110. Crihan, D.; Knapp, M.; Zweidinger, S.; Lundgren, E.; Weststrate, C. J.; Andersen, J. N.; Seitsonen, A. P.; Over, H., Stable Deacon Process for HCl Oxidation over RuO_2. Angewandte Chemie International Edition 2008, 47, 2131–2134.
111. 109. Zweidinger, S.; Crihan, D.; Knapp, M.; Hofmann, J.; Seitsonen, A.; Weststrate, C.; Lundgren, E.; Andersen, J. N.; Over, H., Reaction Mechanism of the Oxidation of HCl over RuO_2(110). The Journal of Physical Chemistry C 2008, 112, 9966–9969.
112. Zweidinger, S.; Hofmann, J.; Balmes, O.; Lundgren, E.; Over, H., In situ Studies of the Oxidation of HCl over RuO_2 Model Catalysts: Stability and Reactivity. Journal of Catalysis 2010, 272, 169–175.
113. Hofmann, J. P.; Zweidinger, S.; Knapp, M.; Seitsonen, A. P.; Schulte, K.; Andersen, J. N.; Lundgren, E.; Over, H., Hydrogen-promoted Chlorination of RuO_2(110). The Journal of Physical Chemistry C 2010, 114, 10901–10909.
114. Hofmann, J. P.; Zweidinger, S.; Seitsonen, A. P.; Farkas, A.; Knapp, M.; Balmes, O.; Lundgren, E.; Andersen, J. N.; Over, H., Dynamic Response of Chlorine Atoms on a RuO_2(110) Model Catalyst Surface. Physical Chemistry Chemical Physics 2010, 12, 15358–15366.
115. Over, H., Atomic-scale Understanding of the HCl Oxidation over RuO_2, A Novel Deacon Process. The Journal of Physical Chemistry C 2012, 116, 6779–6792.
116. Hess, F.; Over, H., Rate-determining Step or Rate-determining Configuration? The Deacon Reaction over RuO_2(110) Studied by DFT-based KMC Simulations. ACS Catalysis 2017, 7, 128–138.
117. Hess, F.; Smarsly, B. M.; Over, H., Catalytic Stability Studies Employing Dedicated Model Catalysts. Accounts of Chemical Research 2020, 53, 380–389.
118. Atanasoska, L.; Atanasoski, R.; Pollak, F.; O'Grady, W., Single Crystal RuO_2/Ti and RuO_2/TiO_2 Interface: LEED, Auger and XPS Study. Surface Science 1990, 230, 95–112.

2. Results and Discussions (Scientific Publications)

2.1 Publication 1: Hydrogen Incorporation in $Ru_xTi_{1-x}O_2$ Mixed Oxides Promotes Total Oxidation of Propane

This publication is on the synthesis and the characterization of $Ru_xTi_{1-x}O_2$ mixed oxides with varying the composition *x* in the range of $0.2 \leq x \leq 1$. Employing XRD a mixture of RuO_2 nanoparticles and Ru-Ti solid solutions can be detected throughout the entire investigated composition range, while the Ru-Ti solid solutions fulfill the Vegard's law, thus evidencing that ruthenium and titanium form a solid solution despite phase separation. XPS reveals that the Ru satellite features monotonically shift to lower binding energies with lower ruthenium concentration pointing to a reduced valence electron density. Hydrogen exposure at 250 °C produces a labile hydrogen species in the mixed oxide lattice, accompanied with the development of macro- and micro-strain, which may be responsible for the improved catalytic activity in the propane activity tests.

H. Over and I devised the experimental schedule. I prepared $Ru_xTi_{1-x}O_2$ mixed oxides. I performed XRD, SEM, TG-MS, HR-TEM experiments. T. Weber and L. Glatthaar performed XPS measurements. P. Timmer, A. Spriewald-Luciano, Y. Wang and I contributed the construction of propane oxidation apparatus and preliminary data analysis. H. Over, B. M. Smarsly, Y. Guo and I contributed through scientific discussion of the data. H. Over and I wrote the draft version of the manuscript. All authors revised the manuscript and have given approval to the final version.

Reprinted from Wang, W.; Wang, Y.; Timmer, P.; Spriewald-Luciano, A.; Weber, T.; Glatthaar, L.; Guo, Y.; Smarsly, B. M.; Over, H. Hydrogen Incorporation in $Ru_xTi_{1-x}O_2$ Mixed Oxides Promotes Total Oxidation of Propane. *Inorganics* **2023**, 11, 330. https://doi.org/10.3390/inorganics11080330.

inorganics

MDPI

Article

Hydrogen Incorporation in $Ru_xTi_{1-x}O_2$ Mixed Oxides Promotes Total Oxidation of Propane

Wei Wang [1,2], Yu Wang [1,2], Phillip Timmer [2], Alexander Spriewald-Luciano [2], Tim Weber [2], Lorena Glatthaar [2], Yun Guo [1,*], Bernd M. Smarsly [2,*] and Herbert Over [2,*]

[1] Key Laboratory for Advanced Materials, Research Institute of Industrial Catalysis, School of Chemistry and Molecular Engineering, East China University of Science and Technology, Shanghai 200237, China
[2] Institute of Physical Chemistry, Justus Liebig University, Heinrich-Buff-Ring 17, 35392 Giessen, Germany
* Correspondence: yunguo@ecust.edu.cn (Y.G.); bernd.smarsly@phys.chemie.uni-giessen.de (B.M.S.); herbert.over@phys.chemie.uni-giessen.de (H.O.)

Abstract: A rational synthetic approach is introduced to enable hydrogen insertion into oxides by forming a solid solution of a reducible oxide with a less reducible oxide as exemplified with RuO_2 and TiO_2 (Ru_x, a mixture of x% RuO_2 with (100−x)% TiO_2). Hydrogen exposure at 250 °C to Ru_x (Ru_x_250R) results in substantial hydrogen incorporation accompanied by lattice strain that in turn induces pronounced activity variations. Here, we demonstrate that hydrogen incorporation in mixed oxides promotes the oxidation catalysis of propane combustion with Ru_60_250R being the catalytically most active catalyst.

Keywords: catalyst promotor; mixed oxides; hydrogenated $Ru_xTi_{1-x}O_2$; propane combustion; hydrogen-induced variation in the activity

check for updates

Citation: Wang, W.; Wang, Y.; Timmer, P.; Spriewald-Luciano, A.; Weber, T.; Glatthaar, L.; Guo, Y.; Smarsly, B.M.; Over, H. Hydrogen Incorporation in $Ru_xTi_{1-x}O_2$ Mixed Oxides Promotes Total Oxidation of Propane. *Inorganics* **2023**, *11*, 330. https://doi.org/10.3390/inorganics11080330

Academic Editors: Torben R. Jensen, Roberto Nisticò, Luciano Carlos, Hicham Idriss and Eleonora Aneggi

Received: 14 June 2023
Revised: 31 July 2023
Accepted: 4 August 2023
Published: 7 August 2023

1. Introduction

Strain-induced changes of the catalytic activity of transition metal compounds in thermal catalysis were predicted by theory [1] and attributed to a shift of the metal d band center with strain [2], so that strain engineering has been considered a promising way to tune activity. Strain can be introduced to the catalyst's material in various ways including epitaxial film growth [3], doping such as Li insertion [4], alloying−dealloying [5], formation of core-shell particles [6] and nano-structuring [7]. In fact, strain engineering has turned out to be an important tool to improve activity in electrocatalysis, most notably for water electrolysis [8–12]. Quite in contrast, in thermal catalysis strain engineering is less often encountered [6,7,13,14], due presumably to missing stability of strain-engineered materials at higher reaction temperatures.

Hydrogenation of the catalyst material might be a convenient way to introduce strain into the host lattice and thereby tune the activity of a catalyst as long as the catalyst material is able to incorporate a sufficient amount of hydrogen into the lattice. For instance, Pd-based catalysts [15,16] were reported to form both absorbed and adsorbed hydrogen that may play an important role in hydrogenation catalysis. Hydrogen interaction with oxides is more intricate than with metals [17] since reducible oxides can face stability problems due to partial or even total reduction up to the metal phase. Exposing hydrogen to oxide surfaces frequently forms surface hydroxyl groups, but it can also incorporate hydrogen into the bulk oxide. Hydrogen exposure to CeO_2 was reported to form of hydride species H^- in bulk CeO_2 [18–22], a process that is facilitated by oxygen vacancies. The formation of hydride species H^- in CeO_2 may explain its remarkable catalytic performance in the partial hydrogenation of alkynes to alkenes [23–25].

Recently, we reported that H_2 exposure at 250 °C to mixed $Ru_{0.3}Ti_{0.7}O_2$ is able to incorporate about 20 mol% hydrogen into the rutile lattice, thereby altering slightly the lattice parameters [26]. This was considered a remarkable finding since RuO_2 is not stable

under such conditions and transforms readily to metallic Ru, while TiO_2 is not able to incorporate hydrogen into the lattice, at least not at 250 °C. Hydrogenation of $Ru_{0.3}Ti_{0.7}O_2$ was shown to increase substantially the catalytic oxidation activity in the total oxidation of propane and HCl oxidation reaction.

In the present study, we systematically vary the composition x of the mixed oxide $Ru_xTi_{1-x}O_2$ (Ru_x). For various compositions ranging from x = 0.2 to x = 1.0 in steps of 0.1, we explore the hydrogenation behavior at 250 °C and compare the catalytic activity of $Ru_xTi_{1-x}O_2$ with that of the corresponding hydrogenated catalysts in the total oxidation of propane. Without hydrogen treatment, Ru_x reveals a strict composition−activity correlation of activity in that the higher the Ru concentration the higher the activity; highest activity is achieved with Ru_100. However, when treating Ru_x with hydrogen at 250 °C for 3 h (Ru_x_250R), the highest activity is encountered for compositions where both Ru and Ti have similar concentrations. Ru_60_250R turns out to be the most active propane combustion catalyst exceeding even the activity of Ru_100. The hydrogen-induced activity variation is tentatively attributed to hydrogen-induced strain in the mixed oxide $Ru_xTi_{1-x}O_2$.

2. Experimental Results

2.1. Characterization of the Fresh Ruthenium−Titanium Mixed Oxide Samples

Figure 1a summarizes the X-ray diffraction (XRD) patterns of freshly prepared ruthenium−titanium mixed oxide catalysts Ru_x with different nominal Ru concentrations, x; the diffraction pattern of pure commercial rutile-TiO_2 is overlaid for comparison reasons. The XRD pattern of Ru_100 contains reflections from both a rutile structure and metallic Ru (hcp structure). With the addition of titanium to RuO_2, the rutile structure is preserved, and the (110) and the (101) reflections continuously shift towards the reflection of pure rutile TiO_2. Above a Ti concentration of 20 mol% no reflections from metallic Ru are discernible. In addition, the rutile related diffraction peaks split into two components with increasing Ti concentration.

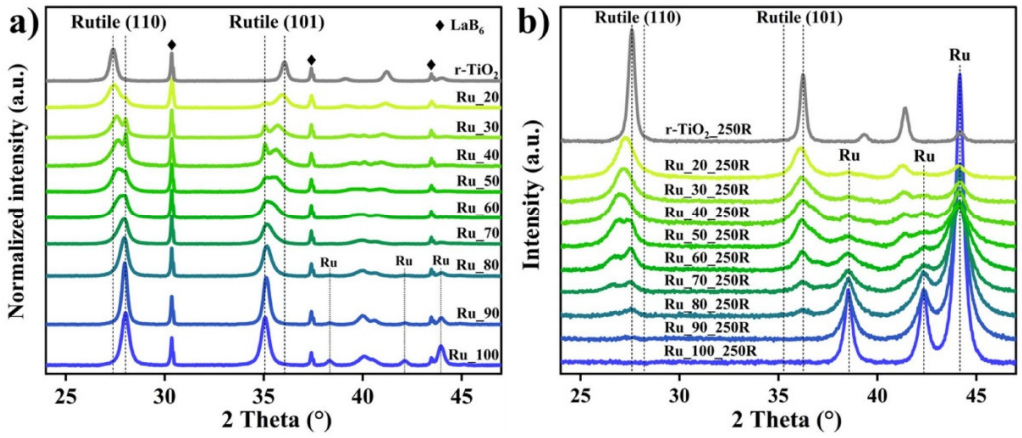

Figure 1. (**a**) X-ray diffraction (XRD) patterns of the ruthenium−titanium mixed oxide catalysts Ru_x; the composition x of Ru ranges from 20 mol% to 100 mol%. Dashed lines indicate the position of pure rutile-TiO_2 and RuO_2. (**b**) XRD patterns of Ru_x_250R catalysts treated in 4 vol% H_2/N_2 at 250 °C for various compositions x ranging from 20% to 100%.

The sharp reflections at 28.02° from rutile (110) and 35.07° from rutile (101) do not vary with the Ti concentration and therefore are assigned to the pure RuO_2 phase. The position of the broader component in XRD shifts continuously towards rutile TiO_2 and

is hence ascribed to solid solution $Ru_xTi_{1-x}O_2$. The coexistence of pure RuO_2 and mixed $Ru_xTi_{1-x}O_2$ in a wide range of compositions evidences a miscibility gap consistent with previous findings based on a similar polymer-assisted preparation method [27] and in agreement with a recent DFT study [28].

In Figure S1, we present the peak deconvolution of the rutile (110) reflection and that of the (101) reflection. For high Ru-content samples like Ru_90, Ru_80 and Ru_70, the (110)/(101) peaks are found to be asymmetric, which clearly points toward a phase separation. For low Ru-content samples this phase separation is pronounced, with two separated reflections corresponding to the RuO_2 phase and $Ru_xTi_{1-x}O_2$ oxide phase, respectively. Therefore, we assume that a pure RuO_2 phase exists in the full composition range of Ru–Ti mixed oxides. In the decomposition of the diffraction patterns, we fix the peak position of pure RuO_2 and assume that the mixed $Ru_xTi_{1-x}O_2$ oxide phase crystallizes in the rutile structure. As a main result of the decomposition, the peak position of Ru–Ti solid solution turns out to linearly shift to lower angles with the increasing Ti concentration (cf. Figure S2), in accordance with Vegard's law [29]. The deconvolution analysis in the present study emphasizes that the prepared samples are not phase pure but facing a miscibility gap.

Together with the analysis of the rutile (101) reflection, we can derive the unit cell parameters *a*/*b* and *c* of the mixed oxide $Ru_xTi_{1-x}O_2$ as a function of the composition *x* that are summarized in Figure 2. The linear shift in *a*/*b* and *c* with the nominal composition indicates the fulfillment of Vegard's law, thus corroborating the formation of a solid solution $Ru_xTi_{1-x}O_2$ with nominal composition *x*. Besides, the calculated unit cell volumes for the Ru_x samples (cf. Figure S3) do not vary significantly with the nominal composition *x*. Note that phase separation becomes more severe for the Ru_20 sample with its solid solution phase starting to deviate from Vegard's law.

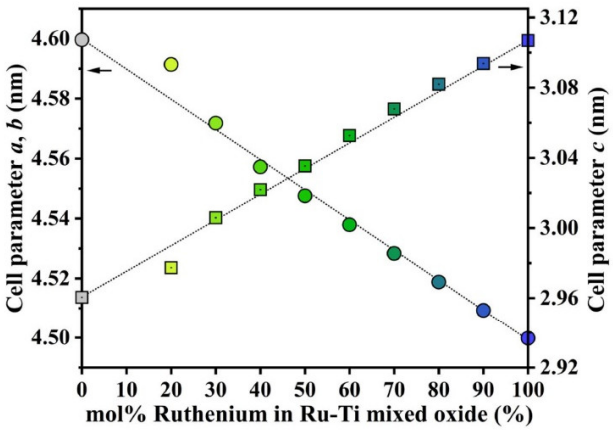

Figure 2. Lattice parameters of rutile $Ti_{1-x}Ru_xO_2$ solid solution as a function of the nominal composition *x* given in mol%, as derived from the peak deconvolution of rutile (110) and rutile (101).

As seen from Figure S1, the FWHM of the RuO_2 peak decreases, while that of the mixed oxide increases with Ti concentration. Utilizing the Scherrer equation, this observation translates to an increase of the crystallite size of RuO_2, while that of the mixed oxide decreases with increasing Ti concentration (until 50% Ti) (cf. Table 1). In order to consider also the micro-strain in the calculation of the crystallite size, we use the Williamson−Hall method [30], whose results are summarized in Figure S4 and Table S1; the Williamson−Hall plots of RuO_2 and the Ru–Ti solid solution phase are exemplified for the Ru_60 sample shown in Figure S5. Since the micro-strain values $\Delta\varepsilon$ ($\leq$0.004) of the powder materials are relatively low compared to those described in the literature [31], the values derived from the Scherrer equation are practically not affected by the micro-strain.

Table 1. XRD derived data of Ru–Ti mixed oxide catalysts.

Catalysts	Cell Parameter a/b (nm) [a]	Cell Parameter c (nm) [b]	Grain Size (RuO_2) (nm) [c]	Grain Size (Ru–Ti) (nm) [c]	Ru–Ti/(RuO_2 + Ru–Ti) (%) [d]
Ru_100	4.500	3.107	18 ± 0.5	-	0
Ru_90	4.509	3.094	27 ± 1	25 ± 2	81.2
Ru_80	4.519	3.082	32 ± 0.5	15 ± 0.3	89.9
Ru_70	4.528	3.068	33 ± 1	12 ± 0.2	90.9
Ru_60	4.538	3.053	36± 1	10 ± 0.5	93.7
Ru_50	4.548	3.035	46 ± 8	9 ± 0.5	96.4
Ru_40	4.558	3.022	45 ± 6	10 ± 0.5	88.8
Ru_30	4.572	3.006	43 ± 5	12 ± 2	81.9
Ru_20	4.591	2.977	28 ± 6	16 ± 1	92.5

a: Calculated by rutile (110) reflection of the Ru–Ti solid solution phase. *b*: Calculated based on obtained a/b value and rutile (101)/(101) reflections of the Ru–Ti solid solution phase. *c*: Determined by Scherrer equation from the (110)/(101) reflections of the RuO_2 phase after peak deconvolution. *d*: Determined by peak deconvolution of the (110)/(101) reflections.

From XRD we gain the following structural information of the Ru–Ti mixed oxides: RuO_2 nanoparticles and Ru–Ti solid solutions co-exist throughout the entire composition range, while metallic ruthenium is eliminated when more than 20 mol% titanium is incorporated. The Ru–Ti solid solutions fulfill Vegard's law, thus evidencing that ruthenium and titanium form a solid solution despite phase separation.

While XRD is a bulk characterization method, X-ray photoelectron spectroscopy (XPS) can determine the surface/near-surface compositions of Ru_x catalysts with varying nominal x values (as presented in Figure S6, fitting parameters are compiled in Table S2). From the Ru 3d XP spectra, Ti-rich samples (Ru_40, Ru_30 and Ru_20) show a weak peak at ~288.0 eV whose origin may be attributed to the formed carbonates (O=C=O) from exposure to air or from residual carbon of preparation. It is evident that ruthenium is in the Ru^{4+} oxidation state in each sample Ru_x; this assignment is corroborated by the pronounced satellite features [32]. No metallic ruthenium is detected on the catalyst surface, proving that the metallic ruthenium species (see in Figure 1a) is encapsulated by the oxide. Buried metallic ruthenium is not expected to participate in the catalytic reaction.

Additionally, the binding energies of $Ru3d_{5/2}$ and $Ru3d_{3/2}$ do not vary with the composition, while, surprisingly, the Ru satellite features monotonically shift to lower binding energies with lower ruthenium concentration (see in Figure 3), from 282.69 eV for Ru_100 to 282.34 eV for Ru_30. As the satellite feature is attributed to surface plasmon excitation [33], this shift is correlated to a reduced valence electron density in $Ru_xTi_{1-x}O_2$.

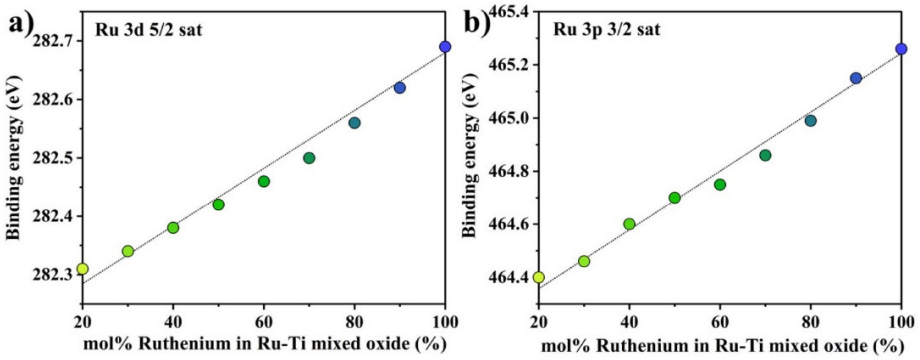

Figure 3. Shift of binding energies of (**a**) Ru 3d satellite features. (**b**) Ru 3p satellite features derived from peak deconvolution of XPS data when varying the composition *x* of Ru_x.

The O 1s spectrum in Figure S7 depicts two chemical states of near surface oxygen: one is the O^{2-} from the lattice oxygen at ~529 eV, and the other, a shoulder peak at higher binding energy (around 531.8 eV), which is ascribed to the surface OH groups/oxygenated carbon [34]. The integral ratio of OH to the entire surface oxygen is continuously decreasing on lowering the ruthenium concentration, from 39.30% (for Ru_100) to 2.50% (for Ru_50), thus indicating that the incorporation of titanium reduces greatly the amount of surface OH on the catalyst surface.

Since the Ru 3p and Ti 2p XPS features are in the same binding energy region, the surface composition of ruthenium and titanium can be quantified by peak deconvolution. As presented in Table S2 and Figure S8, the Ru 3p region also exhibits satellite features, which behave identically to those in the Ru 3d region; the shifts to lower binding energy further evidence that doping of titanium leads to lower electron density. As compiled in Table 2, the actual surface concentrations deviate quite substantially above a nominal Ru concentration of 60%, while below 50 mol% Ru the surface composition agrees well with the nominal composition.

Table 2. Compositional information from the surface and bulk region of ruthenium−titanium mixed oxide catalysts.

Catalysts	S_{BET} (m^2/g)	Ru/(Ti + Ru)(mol%) [a]	Ru/(Ti + Ru)(mol%) [b]	(OH + Oxygenated Carbon)/O 1s Total [b]
Ru_100	9	100	100	39.90
Ru_90	6	89.3	70.65	14.67
Ru_80	10	78.8	59.81	5.42
Ru_70	14	68.1	60.53	4.85
Ru_60	19	56.7	54.4	4.42
Ru_50	26	46.8	47.74	2.50
Ru_40	32	40.9	37.96	4.69
Ru_30	31	30.0	29.08	3.38
Ru_20	34	17.4	17.61	4.11
Ru_60_250R	19	56.2	52.12	4.43

a: Calculated from SEM-EDS mapping. *b*: Calculated from XPS.

From these XPS results one may ask whether this deviation of the surface composition from the nominal ones originates from an insufficient control of the composition during synthesis. In order to settle this question, we applied dispersive X-ray spectroscopy (EDS)-scanning electron microscopy (SEM) to gain compositional information of all samples. Since the detection depth from EDS reaches several micrometers, we can consider it as a bulk characterization method. The average composition quantified by EDS summarized in Table 2 indicates that, in the full range ($20 \leq x \leq 100$), our synthesized catalysts agree well with the nominal compositions x, thus excluding the possibilities that the deviation of surface concentration is caused by uncertainties in the synthesis procedure.

Besides, with SEM and TEM we also investigate the morphologies of our catalysts. The Ru_100, SEM images in Figure S9 reveal a dense and rough surface with additional macropores, round small particles agglomerate like a sponge. The particle size gradually becomes smaller with increasing titanium concentration until $1 - x = 50\%$. This is in agreement with the crystallite size derived from XRD data, indicating that a proper amount of titanium will efficiently decrease the crystallite size of Ru–Ti mixed oxides. Moreover, TEM micrographs confirm that the particle size of mixed oxides decreases with the addition of titanium. Table 2 summarizes also the Krypton physisorption experiments of all as-prepared samples. The Brunauer−Emmett−Teller (BET) surface area varies quite substantially, changing from 9 m^2/g (for Ru_100) to 34 m^2/g (for Ru_20).

2.2. Hydrogen-Induced Changes of Ruthenium−Titanium Mixed Oxides

We focus on the hydrogen-induced change of the Ru_x samples. The hydrogen treatment consists of an exposure of 4% H_2/N_2 for 3 h at 250 °C. The specific reduction

temperature of 250 °C has been shown to result in a large hydrogen uptake for the case of Ru_30 [26]. As shown in Figure 1b, Ru_00, e.g., pure rutile-TiO_2, is not affected by this hydrogen treatment, while Ru_100 is fully transformed to metallic Ru phase, consistent with our previous study [26].

The diffraction peak of RuO_2 at 2θ = 28.02° disappears in Figure 1b when exposed to 4% H_2/N_2 at 250 °C, while the intensity of Ru metal-related diffraction increases. As expected, the metallic Ru diffraction intensity is higher the higher is the Ru content x of Ru_x. This means that the RuO_2 particles are easily reduced to metallic ruthenium at a temperature of 250 °C, consistent with previously published studies [35,36].

Quite in contrast, the rutile diffraction peaks of the mixed oxide phases (110) and (101) persist and shift only in position to the lower and higher angles, respectively, upon exposure to 4% H_2/N_2 at 250 °C. The degree of peak shift depends on the Ru concentration. Close to 50 mol% Ru, the observed shift is the highest. Actually, the shifted diffraction peak of rutile consists of two components, most likely evidencing different hydrogen concentrations in the mixed oxide crystallites. The bulk composition of Ru_x (cf. Table 2) does not change when exposed to H_2 at 250 °C (Ru_x_250R). As discussed recently [26], these shifts of the reflections are caused by the incorporation of hydrogen and not by reduction of the metal ions.

The Ru_x_250R samples are subsequently subject to a mild re-oxidation treatment that is conducted at 300 °C and the XRD patterns are presented in Figure S10a, and the changes of macrostrain (position) and micro-strain (FWHM) among the initial, reduced and re-oxidized samples as exemplified by Ru_20, Ru_40, Ru_60 and Ru_80 are compiled in Figure S10b. The rutile structure of Ru_x is restored after re-oxidation treatment, while most but not all of the metallic Ru transforms back to RuO_2. For the case of Ru_30_250R, it was shown that full recovery of Ru_30 requires oxidation temperatures of 400 °C [26].

With thermogravimetric-mass spectrometry (TG-MS) the amount of incorporated hydrogen can be quantified by the integrated water signal that is produced by reacting incorporated hydrogen with oxygen during heating of the sample in ambient air. We exemplify this experiment with Ru_60_250R since the catalytic activity of this sample is thoroughly tested. A nitrogen-treated Ru_60_250N sample serves as reference. As summarized in Figure 4, a small mass signal for H_2O (m/z = 18) is evident at 80 °C for Ru_60_250N, while, for Ru_60_250R, a broad and strong water signal appears. This water peak of Ru_60_250R contains actually two components, one is associated with water desorption (90 °C) and the other is related to the oxidation of incorporated hydrogen (maximum at 160 °C). Employing a deconvolution procedure, as indicated in Figure 4, the molar fraction of inserted hydrogen is determined to be 35 mol% based on the integrated water difference area of Ru_60_250R and Ru_60_250N. Recently, the molar fraction of inserted hydrogen for Ru_30_250R was found to be 18 mol% [26]. Another hydrogenation experiment for Ru_40_250R (reference Ru_40_250N) is shown in Figure S11 and yields 23 mol% of inserted hydrogen in Ru_40_250R. Given that Ru_100 and pure TiO_2 rutile cannot incorporate any hydrogen, the obtained amount of incorporated hydrogen among different Ru_x_250R catalysts (Figure S12) reveals a "volcano" type of the H-fraction with the increase of the Ru concentration in the Ru–Ti mixed oxides. The maximum amount of incorporated hydrogen is encountered at the Ru concentration of 60%.

Figure 5 compares the Ru3d XP spectrum of Ru_60 with those of the hydrogen-treated Ru_60_250R sample and the re-oxidized one, Ru_60_250R_300O. Three Ru components, namely metallic Ru, Ru^{4+}, and the satellite of Ru^{4+} and two carbon species are considered to fit the spectra. The Ru_60 sample reveals only the Ru^{4+} component (red) together with the corresponding satellite feature (blue), consistent with the corresponding XRD (pattern Figure 1a) that is composed only of diffraction peaks of the mixed oxide $Ru_{0.6}Ti_{0.4}O_2$ and pure RuO_2. Upon hydrogen exposure at 250 °C, a strong metallic Ru peak becomes apparent in the Ru 3d spectrum. The metallic Ru component comes from the reduction of RuO_2 towards metallic Ru, as indicated by XRD, while the Ru^{4+} component originates from Ru in $Ru_{0.6}Ti_{0.4}O_2$. Upon re-oxidation of Ru_60_250R at 300 °C (Ru_60_250R_300O),

most of metallic component transforms back to Ru^{4+}. We conclude from these experiments that the Ru^{4+} oxidation state $Ru_{0.6}Ti_{0.4}O_2$ is preserved, regardless of the applied treatment (hydrogenation, re-oxidation).

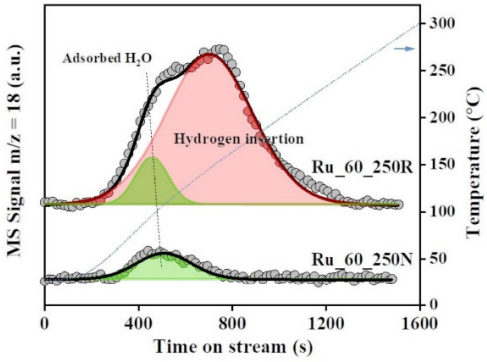

Figure 4. Peak deconvolution of H_2O signal (m/z = 18) of Ru_60_250R and Ru_60_250N from TG-MS analysis.

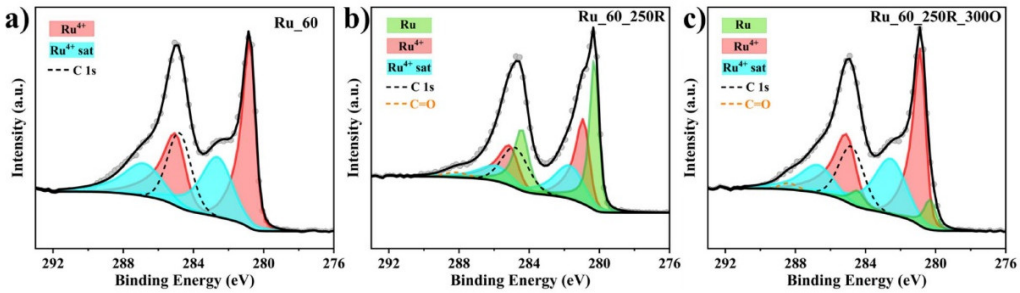

Figure 5. XP spectra of Ru_60 (**a**) in comparison with hydrogen treated sample at 250 °C. (**b**) Ru_60_250R and re-oxidized sample at 300 °C. (**c**) Ru_60_250R_300O. Using the CasaXPS software, the Ru3d spectra are decomposed into five components: Ru^{4+} (red), satellite Ru^{4+} (blue), metallic Ru (green) and two C1s species.

Hydrogen reduction of Ru from $Ru_{0.6}Ti_{0.4}O_2$ can, however, be excluded for the following reasons. The reduction treatment at 250 °C preserves the rutile structure, albeit with low intensity (cf. Figure 6). Upon re-oxidation at 450 °C (Ru_60_250R_450O), however, the rutile diffraction peaks of Ru_60 are practically restored. In particular, rutile diffraction peaks shift back to those positions of Ru_60 (with identical intensity), thus evidencing that the mol% of Ru in the mixed rutile structure has been preserved (Vegard's law).

From HRTEM and element mapping (cf. Figure S13), it is evident that Ru_60 and Ru_60_250R consist mainly of mixed $Ru_xTi_{1-x}O_2$ oxide whose composition has not changed. For Ru_60 larger RuO_2 particles are discernible.

In addition to the Ru 3d spectra (cf. Figure 5), Ti 2p XP spectra are compiled in Figure S14 for Ru_60, the hydrogen treated Ru_60_250R sample and the re-oxidized one, Ru_60_250R_300O. All Ti 2p spectra show only Ti^{4+}, and there is no indication of Ti^{3+}. The overall near-surface composition of Ru_60_250R is collected in Table 2. Corresponding O1s spectra in Figure S15 exhibit two components, one related to O^{2-} and the other assigned to OH/carbonate species. The OH/carbonate feature does not vary when Ru_60 is exposed to hydrogen or is re-oxidized, suggesting that incorporated H does not change the concentration of OH species or carbonate species.

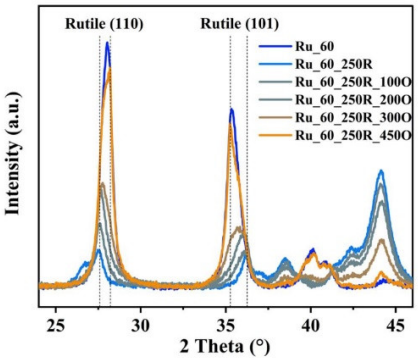

Figure 6. XRD patterns of Ru_60_250R mildly re-oxidized at various temperatures in air. For comparison, Ru_60 and Ru_60_250R are also included.

From all these experiments we infer that the reduction process results in the incorporation of hydrogen within in the mixed oxide and both Ru and Ti in the mixed Ru–Ti oxide phase remain in the 4+ oxidation state.

2.3. Catalytic Tests: Propane Combustion

In the following, we conducted catalytic tests of Ru_x and Ru_x_250R for the total oxidation of propane, serving here as a model reaction. The full set of light-off curves is presented in the ESI (cf. Figure S16a,b). Except for Ru_100, the hydrogenated Ru_x_250R sample is more active than Ru_x. The temperature differences for T_{90} is collected in Figure S16c (T_{90} is the temperature where 90% conversion is realized). From these conversion data, one can recognize that the Ru_x with x close to 60% exhibits highest activity after hydrogenation, that is even higher than that of Ru_100.

In Figure 7 we exemplify light-off curves for propane combustion of Ru_60, Ru100 and Ru_20 before and after hydrogenation. Ru_100 reveals the highest activity among the non-hydrogenated samples with T_{90} = 182 °C. Upon hydrogenation, the light-off curve of Ru_100_250R shifts to higher temperatures (T_{90} = 194 °C). Ru_20 is significantly less active than Ru_100; T_{90} = 231 °C; upon hydrogenation, T_{90} decreases to 211 °C for Ru_20_250R. Ru_60 reaches 90% conversion at 203 °C, while 90% conversion is achieved at 168 °C for Ru_60_250R, i.e., 35 °C lower than for Ru_20 and even 14 °C lower than that for Ru_100.

Since the inserted H in $Ru_xTi_{1-x}O_2$ is a labile species that leaves the sample already at about 100 °C by water formation under ambient atmosphere [26], we performed an additional experiment, where the Ru_60 sample is in situ hydrogenated at 250 °C in the reactor; this procedure allows us to keep the hydrogenation level high in the mixed oxide sample Ru_60. For the catalytic test of propane oxidation, we choose a reaction temperature of 150 °C to avoid full conversion (cf. Figure 8).

Figure 8 indicates that the activity of Ru_60_250R at 150 °C in the first cycle is quite high with a STY value of 5.2 $mol_{(CO_2)} \cdot kg^{-1}_{(Cat)} \cdot h^{-1}$, and it declines in the second cycle to 2.4 $mol_{(CO_2)} \cdot kg^{-1}_{(Cat)} \cdot h^{-1}$ likely due to the removal of incorporated hydrogen [26]. Conducting an in situ hydrogen treatment at 250 °C of Ru_60_250R leads to a re-activation of the catalyst with a steady state STY of 6.1 $mol_{(CO_2)} \cdot kg^{-1}_{(Cat)} \cdot h^{-1}$ that is even higher than the initial activity during the first cycle. Hydrogen exposure at higher temperature will lead to lower activity of the Ru_60_400R sample (STY = 3.1 $mol_{(CO_2)} \cdot kg^{-1}_{(Cat)} \cdot h^{-1}$) (cf. Figure S17). After in situ hydrogen treatment at 150 °C, Ru_60_400R is reactivated with a higher STY value of 4.7 $mol_{(CO_2)} \cdot kg^{-1}_{(Cat)} \cdot h^{-1}$, that is lower than that of Ru_60_250R (cf. Figure S17). Altogether, hydrogen treatment at 250 °C seems to optimize the promotional effect of hydrogen in the total oxidation of propane.

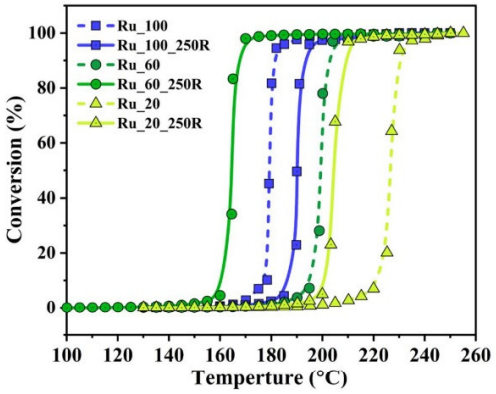

Figure 7. Selection of full conversion curves of catalytic propane combustion over Ru_x and Ru_x_250R (x = 100%, 60% and 20%) as a function of reaction temperature, when cycling the reaction temperature from 30 °C to 250 °C. The full set of conversion curves can be found in Figure S16.

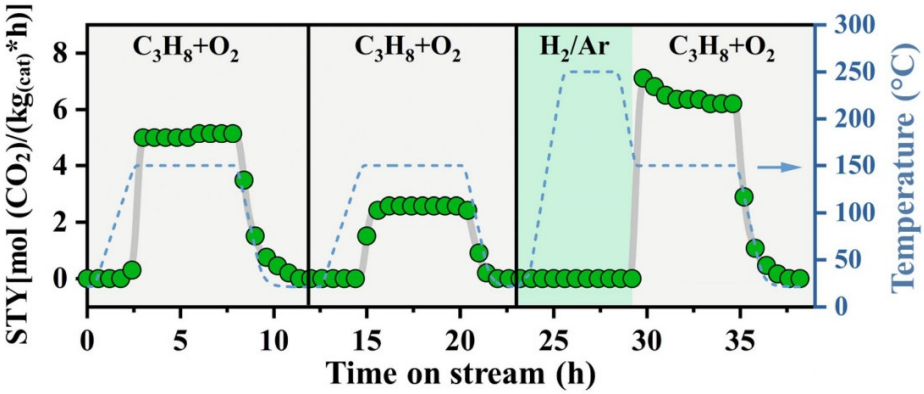

Figure 8. STY as a function of reaction time on catalytic propane oxidation over Ru_60_250R when cycling the reaction temperature from 30 °C to 150 °C (blue dotted line). The gray background represents total C_3H_8 oxidation conditions: 1 vol% C_3H_8, 5 vol% O_2, balanced by N_2; total volume flow: 100 sccm/min, temperature ramp: 1 K/min. The green background represents the gas mixture during heating and cooling stage: 4% H_2/Ar, total volume flow: 50 sccm/min. When reaching 150 °C, the gas composition is switched to the reaction mixture (gray background).

3. Discussion

3.1. Formation of Ru_x and Ru_x_250R

A mixed ruthenium–titanium oxide material with nominal varying concentration *x* of Ru (Ru_x) is successfully prepared by a conventional sol-gel method. Below x = 70%, Ru_x consists of pure RuO_2 and a mixed oxide $Ru_xTi_{1-x}O_2$. For higher concentration of Ru, in addition, a metallic Ru is formed. The metallic Ru phase is caused by the preparation method. For sol-gel synthesis, O_2 cannot penetrate into the polymer network when metal cations nucleate during the calcination stage, thus causing a net reducing environment for the growing particle where the metal cations Ru^{3+} is reduced to Ru^0 [34]. From EDS-SEM and XPS, the bulk and surface compositions for x < 50% are similar and close to the nominal composition of Ru_x, while for x > 50%, the surface composition of Ru is significantly lower than the bulk concentration.

For Ru_x we see a clear linear correlation of the lattice parameters of $Ru_xTi_{1-x}O_2$ with the composition *x* of ruthenium. The cell parameters *a/b* of RuO_2 are smaller than those of TiO_2 while the *c* value of RuO_2 is larger than that of TiO_2, therefore for a mixed oxide, *a/b* and *c* cell parameters of the Ru–Ti phase indicate an "anti-symbatic" behavior (Figure 2). In addition, there is a clear linear correlation of the binding energy of the satellite peak in Ru3d with the composition *x* of ruthenium. (cf. Figure 3) With increasing Ru concentration, the energy of the surface plasmon increases, consistent with the surface plasmon energy being expected to increase in energy with increasing electron density [33].

From XPS, we conclude that both Ti and Ru in Ru_x for $x \leq 70\%$ are in the 4+ oxidation state independent of the composition *x*. Metallic Ru, if present, is buried, as evidenced by XPS, and does therefore not participate in the catalytic reaction.

Hydrogen exposure to Ru_x at 250 °C (Ru_x_250R) leads to hydrogen incorporation in Ru_x for Ru concentration x = 20% up to 80%. (cf. Figure 1) The extremes Ru_00 (e.g., pure rutile-TiO_2) and Ru_100 are not able to incorporate hydrogen: TiO_2 is not affected at all by hydrogenation at 250 °C, as reduction to Magneli phases requires much higher temperatures [37,38]. Ru_100 is completely transformed to metallic Ru, and with increasing Ru concentration, more metallic Ru is formed upon hydrogen exposure at 250 °C. However, 18, 23 and 35mol% of hydrogen are inserted in Ru_30_250R [26], Ru_40_250R, (Figure S11) and R_60_250R, (Figure 4), respectively. From Ru 3d XPS data, there is no indication of an oxidation state of ruthenium other than Ru^0 and Ru^{4+}. The rutile structure of mixed oxide $Ru_xTi_{1-x}O_2$ is maintained upon H_2 exposure at 250 °C, suggesting that the Ru^{4+} can be preserved in rutile structure when mixed with less reducible TiO_2. Therefore, the peak shifts in XRD (Figure 1b) after reduction treatment are caused by the incorporation of hydrogen in the rutile structure and not by the reduction of the metal ions, which is consistent with literature [26]. The only change observed for mixed $Ru_xTi_{1-x}O_2$ is a hydrogen-induced shift in the lattice parameters (cf. Figure 2), i.e., the introduction of hydrogen-induced strain into the mixed oxide lattice. Hydrogen absorption in mixed oxide $Ru_xTi_{1-x}O$ manifests therefore a synergy effect in that Ru enables the activation of H_2 while Ti stabilizes Ru^{4+} against reduction to metallic Ru.

The possible types of inserted hydrogen could be proton, neutral H or hydride H^- species. Based on the XPS data, there are no changes in the oxidation states of Ru^{4+} and Ti^{4+} in the rutile phase (as shown in Figure 5 and Figures S14 and S15). Moreover, from the O 1s spectrum, there is no obvious increase of the OH-related signals, so that we exclude the existence of protons and neutral H in the mixed oxide lattice. Instead, we favor that the incorporated hydrogen is a hydride species $H^{-\delta}$, which is reconciled with the energetic shift of the Ru satellite peak in the Ru3d spectrum and that is correlated with a reduced electron density for exciting the surface plasmon. Obviously, some of the delocalized electrons are localized at $H^{-\delta}$.

Ru_60 can almost be recovered from Ru_60_250R by mild re-oxidation at 450 °C. Re-oxidation at 100 °C starts to remove H-induced changes in strain, both macro- and micro-strain, as reflected by changes in diffraction peak position and FWHM. This behavior was also observed in a previous study of Ru_30, and it was traced to the removal of absorbed hydrogen via water formation [26].

3.2. Improved Oxidation Catalysis of Ru_x_250R in Comparison to Ru_x

The light-off curves of Ru_x and hydrogen inserted Ru_x catalysts are measured for the total oxidation of propane (cf. Figure 7 and Figure S16). These experiments provide compelling evidence that H insertion is beneficial for the oxidation catalysis of propane, with the optimum catalyst being identified with Ru_60_250R. For Ru_100, hydrogenation at 250 °C leads to lower propane combustion activity.

Hydrogen exposure at 250 °C produces a labile hydrogen species in the mixed oxide lattice that can readily be removed by increasing the temperature in the ambient atmosphere (cf. Figure 6). Already a mild re-oxidation at 100 °C restores part of the hydrogen-induced strain in the mixed oxide. From activity experiments in Figure 8, we can conclude that

hydrogen is lost during temperature ramping in the first cycle, although the catalyst runs stably at the final reaction temperature of 150 °C. In order to stabilize inserted H during reaction, the surface needs to be continuously supplied by hydrogen from propane activation. Propane dissociation is activated and needs a temperature of at least 100 °C [39,40]. Therefore, during the heating and cooling ramp in the temperature window of 50–100 °C, the catalyst is exposed to a reaction mixture that is not able to supply the surface with hydrogen. The temperature range of 50–100 °C is, however, high enough to consume inserted hydrogen by water formation due to oxygen in the feed. From this discussion, it is clear that higher activities are expected when the Ru_60_250R catalyst is in situ hydrogen-treated in the reactor during temperature ramping. The activity of propane oxidation (cf. Figure 8) is indeed significantly higher and stable when the catalyst is heated under a hydrogen atmosphere first to the specific reaction temperature and then the gas atmosphere is switched to the actual reaction mixtures. Propane decomposition at high temperature can supply the catalyst surface constantly with hydrogen. Therefore, dissolved hydrogen does not experience a driving force to diffuse towards the surface, thus stabilizing the inserted hydrogen in the lattice of the mixed oxide.

We can safely assume that inserted hydrogen does not take place in the catalytic cycle, since we focus here only on the catalytic propane oxidation reaction. The incorporated hydrogen stabilized by the presence of hydrogen at the surface is, however, the key factor to promote the oxidation catalysis. We expect, however, that for catalytic hydrogenation reaction, the beneficial effect of inserted H may be even more pronounced since inserted hydrogen is able participate in the catalytic cycle.

Hydrogen incorporation is accompanied by the development of macro- and micro-strain of Ru_x, as evidenced by the shift and broadening of the rutile diffraction maxima in the powder XRD (cf. Figure 1), while, after mild re-oxidation at 300 °C, the macro- and micro-strain of Ru_x_250R is largely removed, as reflected by the recovery of the peak position and FWHM (cf. Figure S10). Whether H insertion itself or the induced changes of lattice parameters leads to electronic modifications cannot be disentangled at this point and needs to be scrutinized by future ab initio studies. In any case, the electronic structure is affected by H insertion, as corroborated in the observed binding energy shift of the satellite feature in Ru3d (cf. Figure 3). The increased activity can therefore be related to the altered electronic structure of $Ru_xTi_{1-x}O_2$. A direct correlation of strain with activity is, however, not evident for Ru_x_250R and needs further studies.

4. Materials and Methods

4.1. Materials

Ruthenium (III) trichloride hydrate ($RuCl_3 \cdot xH_2O$, Ruthenium content: 40.00–49.00%, ReagentPlus®), anhydrous citric acid ($C_6H_8O_7$, ≥99.5%), ammonia solution (NH_4OH, 25%) and titanium butoxide ($C_{16}H_{36}O_4Ti$, 97%) are purchased from Sigma-Aldrich (St. Louis, MO, USA) and used without further purification.

4.2. Catalysts Preparation

Ru–Ti mixed oxide materials with varying compositions are prepared by a conventional citric acid assisted sol-gel method (cf. Figure 9) and are denoted as Ru_x, where x represents the nominal molar percentage of ruthenium varying from 20% to 100%. For the procedural synthesis of Ru_60: 0.024 mol citric acid (anhydrous) is dissolved into 50 mL deionized water, and the solution is stirred and kept at 60 °C. Then, 5 mL anhydrous ethanol containing 0.8 mmol titanium butoxide is quickly injected into the citric acid solution. After thorough mixing, 0.0012 mol $RuCl_3 \cdot xH_2O$ is added to the solution and stirred for another 30 min at 60 °C. The full complexation of the ruthenium and titanium cations is accomplished by slowly heating the mixture to 80 °C, afterwards, the aqueous ammonia solution of 2 mol/L is added dropwise to adjust the pH of the solution to ~6. Finally, the dark brown but transparent solution is evaporated at 90 °C and the obtained dark green gel is dried at 120 °C for 12 h. Subsequently, the dark foamy material is carefully ground

before calcination at 450 °C for 4 h in static air at 2 °C/min, and the product is ground again for further catalytic tests and characterizations. Note that, contrary to the commonly used version of the Pechini method, here, no glycol is added. The preparation of the other Ru_x catalysts follows the same procedure but adjusting the molar ratio of the ruthenium and titanium precursors.

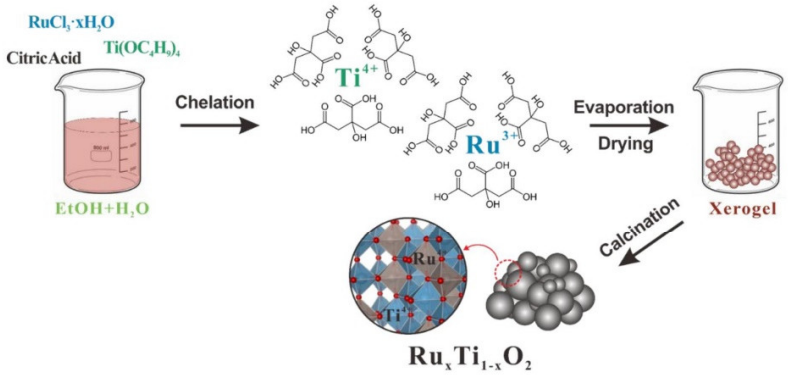

Figure 9. Illustration of the citric acid assisted sol-gel method to prepare mixed oxides of RuO_2 and TiO_2 with varying concentration x of Ru: Ru_x.

Hydrogen insertion experiments are performed as follows: 50 mg of fresh Ru_x powder material is treated at various temperatures under 4 vol% H_2/N_2 for 3 h, the total flow rate being set to 50 sccm/min. After hydrogen treatment, the catalyst is cooled down to room temperature under the same atmosphere. The obtained catalyst is referred to as Ru_x_yR, where x represents the nominal molar percentage of ruthenium, y represents the reduction temperature. The re-oxidation experiment follows the same procedure while the gas atmosphere is changed to dry air. The catalyst is now denoted as Ru_x_yR_zO, where z stands for the re-oxidation temperature. For comparison, a blank experiment is also conducted by calcining the Ru_x under pure N_2 and the catalyst is referred to as Ru_x_yN.

4.3. Catalysts Characterization

Powder XRD patterns are recorded on a Panalytical Empyrean diffractometer (Malvern, UK) equipped with a Cu K_α radiation (40 kV, 40 mA). The correction of the 2θ shift that may originate from different positions of the sample holder is assisted by mixing LaB_6 standard powder (NIST) with all the catalysts before measurement. The Scherrer equation is applied to calculate the crystallite size.

Kr physisorption experiments are performed at T = 77 K with an Autosorb 6 instrument (Quantachrome, Ostfildern, Germany), all the catalysts are pre-treated in vacuum for 12 h at 100 °C. The specific surface area is calculated by the BET method. Note that we deliberately used Kr, instead of nitrogen or argon, because the materials we anticipated to exhibit small surface areas, and Kr has a higher sensitivity in this respect.

Scanning transmission electron microscopy (STEM) micrographs are recorded on a ThermoFisher Talos F200X electron microscope (Waltham, MA, USA). SEM images are obtained on a Gemini SEM 560 instrument (Carl Zeiss MicroImaging GmbH, Göttingen, Germany). The average composition of the catalyst is quantified by energy dispersive X-ray spectroscopy (EDS).

XPS spectra are acquired on a PHI VersaProbe II instrument (Feldkirchen, Germany) equipped with a monochromatized Al-Kα line, the photon energy is 1486.6 eV. XPS spectrum data analysis is performed by using a CasaXPS software (Version 2.3.17), and the standard Carbon 1s (at 284.8 eV) is used to re-determine all the binding energy. After

calcination, the Ru_x samples do not show any residual chlorine in the XP overview spectra.

A TG-MS experiment is conducted on a STA 409PC thermoscale (Netzsch, Selb, Germany) analyzer coupled with a QMG421 quadrupole mass spectrometer (MS) from Balzers (Balzers, Liechtenstein) with an ionization energy of 70 eV. The catalyst is heated under dry air (30 sccm/min) from 25 to 500 °C, while the heating rate is 10 °C/min. The detailed procedure for calculating the amount of inserted hydrogen is as follows: dry air is applied (30 mL/min) during the TG-MS experiment. Since the flow rate/MS signal of N_2 is constant in air (78.1%), we can use the concentration of N_2 as reference to obtain the flow rate of H_2O (gaseous) by dividing the MS signal of H_2O by N_2. After having the ratio of H_2O/N_2, the total H_2O volume is determined by integration, from which the molar amount of produced H_2O and hence the molar amount of inserted hydrogen are derived; note the sample storage conditions of Ru_x_250R and Ru_x_250N are identical to guarantee accurate data processing.

4.4. Catalytic Tests

The catalytic performance of propane oxidation on the mixed Ru–Ti oxide catalysts is evaluated in a home-made quartz reactor (inner diameter = 6 mm). The feed gas contains 1 vol.% C_3H_8 (purity: 3.5), 5 vol.% O_2 (purity: 4.8) and 94 vol.% N_2 (purity: 4.8) and is admitted to reactor with a total mass flow rate of 100 cm^3 STP min^{-1} (sccm). During catalytic measurement, the temperature of a mixture consisting of 20 mg of catalyst and 40 mg of quartz sand is programmed from 25 °C to 250 °C with a heating rate of 1 °C/min. The corresponding weight hourly space velocity is 345000 $mL \cdot g^{-1} \cdot h^{-1}$. For product analysis, a nondispersive infrared sensor is coupled downstream to detect the volumetric concentration of CO/CO_2 and C_3H_8. The conversion of propane (%) is determined based on the following equation:

$$X_{C_3H_8} = \frac{c(CO_2)}{c_{max}(CO_2)} \times 100\% \quad (1)$$

where $c(CO_2)$ is the real-time concentration of CO_2 in the outlet gas and $c_{max}(CO_2)$ is the steady-state concentration of CO_2 when full conversion is achieved. Propane conversion calculated by the change of the propane concentration is simultaneously conducted to countercheck data accuracy. During the whole temperature range, there is no CO detected and the concentration of CO_2 at full conversion state is virtually three times the inlet propane concentration, thus evidencing that the carbon mass is balanced and no other byproduct is formed. Finally, we use space time yield ($mol_{(CO_2)} \cdot kg^{-1}_{(Cat)} \cdot h^{-1}$, molar amount of CO_2 per kilogram catalyst and hour, STY) to quantify the activity of the catalyst in total propane oxidation reaction.

5. Conclusions

A rational synthesis approach is introduced to favor hydrogen incorporation in the oxide lattice by mixing a reducible oxide with a less reducible oxide, as exemplified with the solid solution of RuO_2 and rutile TiO_2. Neither RuO_2 nor rutile-TiO_2 is able to incorporate hydrogen into the lattice just by hydrogen exposure at elevated temperatures: rutile-TiO_2 is not affected at all, while Ru_100 is fully reduced to metallic ruthenium. We show that mixed $Ru_xTi_{1-x}O_2$ is stable against H_2 exposure at 250 °C for compositions $0.2 < x < 0.8$ and hydrogen can be incorporated into the lattice. Hydrogen incorporation in mixed oxide $Ru_xTi_{1-x}O_2$ reveals a synergy effect in that Ru enables the activation of H_2, while Ti stabilizes the oxidation state of Ru (Ru^{4+}) against reduction to metallic Ru.

Hydrogen insertion into the rutile lattice of $Ru_xTi_{1-x}O_2$ is accompanied by a change of the lattice constants (XRD) and increased micro-strain. Hydrogen insertion affects directly or indirectly via macro- and micro-strain the electronic structure of $Ru_xTi_{1-x}O_2$ that in turn is expected to be responsible for the improved catalytic activity, not only for oxidation catalysis as exemplified with the propane oxidation, but may be equally beneficial for the selective hydrogenation and oxidation of other organic compounds. For propane

combustion, we show that the activity of Ru_x is significantly increased by H_2 exposure at 250 °C. The optimum catalyst is identified with Ru_60_250R, whose activity is substantially higher than that of Ru_100.

Hydrogen treatment can also be conducted in situ by H_2 exposure during temperature ramping and switching to the reaction mixture when the reaction temperature is reached, thus providing an additional parameter to tune the catalytic performance of a mixed oxide catalyst in the reactor. This approach is of general interest in catalysis research and inorganic chemistry to fine-tune properties of (mixed) oxides and may therefore open exciting perspectives for tuning the catalytic activity of mixed oxide catalysts, not only in thermal catalysis but also in electrocatalysis of acidic water splitting at the anode side.

Supplementary Materials: The following supporting information can be downloaded at: https://www.mdpi.com/article/10.3390/inorganics11080330/s1, Figure S1: Decomposition of the (110) and (101) reflection of Ru_x; Figure S2: Peak shift of rutile (110) and (101); Figure S3: Calculated cell volumes of the mixed oxide RuxTi1−xO2 phase; Table S1: Calculation of grain size and micro-strain of Ru–Ti mixed oxide catalysts by the Williamson−Hall method; Figure S4: Calculated crystallite size of RuO2 phase and Ru–Ti solid solution phase; Figure S5: Williamson−Hall plot of RuO2 phase and Ru–Ti solid solution phase as exemplified by Ru_60 sample; Table S2: Optimized fitting parameters for the XPS data deconvolution; Figure S6: Ru 3d XP spectra of Ru_x catalysts; Figure S7: O 1s spectra of Ru_x catalysts; Figure S8: Ru3p and Ti2p spectra of Ru_x catalysts; Figure S9: SEM micrographs for the various Ru_x samples; Figure S10: XRD patterns of Ru_x_250R samples re-oxidized at 300 °C; Figure S11: H2O signal from TG-MS analysis; Figure S12: The calculated amount of incorporated hydrogen when varying the composition x of Ru_x; Figure S13: HAADF-STEM images/element mapping of Ru_60 sample; Figure S14: Ti 2p XP spectra of Ru_60 sample; Figure S15: O 1s XP spectra of Ru_60sample; Figure S16: Light-off curves of catalytic propane combustion; Figure S17: STY as a function of reaction time over Ru_60_400R at 150 °C.

Author Contributions: Conceptualization, methodology, writing—original draft, W.W.; data curation, investigation, Y.W.; methodology, P.T. and A.S.-L.; investigation, T.W. and L.G.; supervision, resources, Y.G. and B.M.S.; conceptualization, supervision, writing—review and editing, H.O. All authors have read and agreed to the published version of the manuscript.

Funding: This project was supported financially by National Key Research and Development Program of China (2022YFB3504200), the National Natural Science Foundation of China (U21A20326, 21976057, 21922602 and 21673072), the fund of the National Engineering Laboratory for Mobile Source Emission Control Technology (NELMS2020A05) and the Fundamental Research Funds for the Central Universities.

Data Availability Statement: Not applicable.

Acknowledgments: W.W. gratefully acknowledges the China Scholarship Council for the Joint-Ph.D. program between the China Scholarship Council and the Institute of Physical Chemistry of the Justus-Liebig-University Giessen. We acknowledge support from the Center for Materials Research at the JLU. H.O. and L.G. acknowledge funding by the German Research Foundation (DFG, Deutsche Forschungsgemeinschaft—493681475).

Conflicts of Interest: The authors declare that they have no known competing financial interests or personal relationships that could have appeared to influence the work reported in this paper.

References

1. Mavrikakis, M.; Hammer, B.; Nørskov, J.K. Effect of Strain on the Reactivity of Metal Surfaces. *Phys. Rev. Lett.* **1998**, *81*, 2819–2822. [CrossRef]
2. Hammer, B.; Nørskov, J.K. *Chemisorption and Reactivity on Supported Clusters and Thin Films*; Kluwer Academic: Dordrecht, The Netherlands, 1997; pp. 285–351.
3. Buvat, G.; Eslamibidgoli, M.J.; Youssef, A.H.; Garbarino, S.; Ruediger, A.; Eikerling, M.; Guay, D. Effect of IrO_6 Octahedron Distortion on the OER Activity at (100) IrO_2 Thin Film. *ACS Catal.* **2020**, *10*, 806–817. [CrossRef]
4. Wang, H.; Xu, S.; Tsai, C.; Li, Y.; Liu, C.; Zhao, J.; Liu, Y.; Yuan, H.; Abild-Pedersen, F.; Prinz, F.B.; et al. Direct and Continuous Strain Control of Catalysts with Tunable Battery Electrode Materials. *Science* **2016**, *354*, 1031–1036. [CrossRef]
5. Strasser, P.; Kühl, S. Dealloyed Pt-based Core-shell Oxygen Reduction Electrocatalysts. *Nano Energy* **2016**, *29*, 166–177. [CrossRef]

6. Gawande, M.B.; Goswami, A.; Asefa, T.; Guo, H.; Biradar, A.V.; Peng, D.-L.; Zboril, R.; Varma, R.S. Core-shell Nanoparticles: Synthesis and Applications in Catalysis and Electrocatalysis. *Chem. Soc. Rev.* **2015**, *44*, 7540–7590. [CrossRef] [PubMed]
7. Zhang, S.; Zhang, X.; Jiang, G.; Zhu, H.; Guo, S.; Su, D.; Lu, G.; Sun, S. Tuning Nanoparticle Structure and Surface Strain for Catalysis Optimization. *J. Am. Chem. Soc.* **2014**, *136*, 7734–7739. [CrossRef]
8. Kibler, L.A.; El-Aziz, A.M.; Hoyer, R.; Kolb, D.M. Tuning Reaction Rates by Lateral Strain in a Palladium Monolayer. *Angew. Chem. Int. Ed.* **2005**, *44*, 2080–2084. [CrossRef] [PubMed]
9. Strasser, P.; Koh, S.; Anniyev, T.; Greeley, J.; More, K.; Yu, C.; Liu, Z.; Kaya, S.; Nordlund, D.; Ogasawara, H.; et al. Lattice-strain Control of the Activity in Dealloyed Core-shell Fuel Cell Catalysts. *Nat. Chem.* **2010**, *2*, 454–460. [CrossRef]
10. Xia, Z.; Guo, S. Strain Engineering of Metal-based Nanomaterials for Energy Electrocatalysis. *Chem. Soc. Rev.* **2019**, *48*, 3265–3278. [CrossRef]
11. Wang, L.; Zeng, Z.; Gao, W.; Maxson, T.; Raciti, D.; Giroux, M.; Pan, X.; Wang, C.; Greeley, J. Tunable Intrinsic Strain in Two-dimensional Transition Metal Electrocatalysts. *Science* **2019**, *363*, 870–874. [CrossRef]
12. You, B.; Tang, M.T.; Tsai, C.; Abild-Pedersen, F.; Zheng, X.; Li, H. Enhancing Electrocatalytic Water Splitting by Strain Engineering. *Adv. Mater.* **2019**, *31*, 1807001. [CrossRef] [PubMed]
13. Alayoglu, S.; Nilekar, A.U.; Mavrikakis, M.; Eichhorn, B. Ru-Pt Core-shell Nanoparticles for Preferential Oxidation of Carbon Monoxide in Hydrogen. *Nat. Mater.* **2008**, *7*, 333–338. [CrossRef] [PubMed]
14. Schlapka, A.; Lischka, M.; Groß, A.; Käsberger, U.; Jakob, P. Surface Strain versus Substrate Interaction in Heteroepitaxial Metal Layers: Pt on Ru(0001). *Phys. Rev. Lett.* **2003**, *91*, 016101. [CrossRef]
15. Teschner, D.; Borsodi, J.; Wootsch, A.; Révay, Z.; Hävecker, M.; Knop-Gericke, A.; Jackson, S.D.; Schlögl, R. The Roles of Subsurface Carbon and Hydrogen in Palladium-Catalyzed Alkyne Hydrogenation. *Science* **2008**, *320*, 86–89. [CrossRef] [PubMed]
16. Wilde, M.; Fukutani, K.; Ludwig, W.; Brandt, B.; Fischer, J.-H.; Schauermann, S.; Freund, H.-J. Influence of Carbon Deposition on the Hydrogen Distribution in Pd Nanoparticles and Their Reactivity in Olefin Hydrogenation. *Angew. Chem. Int. Ed.* **2008**, *47*, 9289–9293. [CrossRef] [PubMed]
17. Copéret, C.; Estes, D.P.; Larmier, K.; Searles, K. Isolated Surface Hydrides: Formation, Structure, and Reactivity. *Chem. Rev.* **2016**, *116*, 8463–8505. [CrossRef]
18. Wu, Z.; Cheng, Y.; Tao, F.; Daemen, L.; Foo, G.S.; Nguyen, L.; Zhang, X.; Beste, A.; Ramirez-Cuesta, A.J. Direct Neutron Spectroscopy Observation of Cerium Hydride Species on a Cerium Oxide Catalyst. *J. Am. Chem. Soc.* **2017**, *139*, 9721–9727. [CrossRef]
19. Werner, K.; Weng, X.; Calaza, F.; Sterrer, M.; Kropp, T.; Paier, J.; Sauer, J.; Wilde, M.; Fukutani, K.; Shaikhutdinov, S.; et al. Toward an Understanding of Selective Alkyne Hydrogenation on Ceria: On the Impact of O Vacancies on H_2 Interaction with CeO_2(111). *J. Am. Chem. Soc.* **2017**, *139*, 17608–17616. [CrossRef]
20. Cao, T.; You, R.; Zhang, X.; Chen, S.; Li, D.; Zhang, Z.; Huang, W. An in situ DRIFTS Mechanistic Study of CeO_2-catalyzed Acetylene Semihydrogenation Reaction. *Phys. Chem. Chem. Phys.* **2018**, *20*, 9659–9670. [CrossRef]
21. Cheng, H.; Wen, M.; Ma, X.; Kuwahara, Y.; Mori, K.; Dai, Y.; Huang, B.; Yamashita, H. Hydrogen Doped Metal Oxide Semiconductors with Exceptional and Tunable Localized Surface Plasmon Resonances. *J. Am. Chem. Soc.* **2016**, *138*, 9316–9324. [CrossRef]
22. Li, Z.; Werner, K.; Qian, K.; You, R.; Płucienik, A.; Jia, A.; Wu, L.; Zhang, L.; Pan, H.; Kuhlenbeck, H.; et al. Oxidation of Reduced Ceria by Incorporation of Hydrogen. *Angew. Chem. Int. Ed.* **2019**, *58*, 14686–14693. [CrossRef]
23. Vilé, G.; Bridier, B.; Wichert, J.; Pérez-Ramírez, J. Ceria in Hydrogenation Catalysis: High Selectivity in the Conversion of Alkynes to Olefins. *Angew. Chem. Int. Ed.* **2012**, *51*, 8620–8623. [CrossRef]
24. Vilé, G.; Colussi, S.; Krumeich, F.; Trovarelli, A.; Pérez-Ramírez, J. Opposite Face Sensitivity of CeO_2 in Hydrogenation and Oxidation Catalysis. *Angew. Chem. Int. Ed.* **2014**, *53*, 12069–12072. [CrossRef]
25. Carrasco, J.; Vilé, G.; Fernández-Torre, D.; Pérez, J.; Pérez-Ramírez, R.; Ganduglia-Pirovano, M.V. Molecular-Level Understanding of CeO_2 as a Catalyst for Partial Alkyne Hydrogenation. *J. Phys. Chem. C* **2014**, *118*, 5352–5360. [CrossRef]
26. Wang, W.; Timmer, P.; Luciano, A.S.; Wang, Y.; Weber, T.; Glatthaar, L.; Guo, Y.; Smarsly, B.M.; Over, H. Inserted Hydrogen Promotes Oxidation Catalysis of Mixed $Ru_{0.3}Ti_{0.7}O_2$ as Exemplified with Total Propane Oxidation and the HCl Oxidation Reaction. *Catal. Sci. Technol.* **2023**, *13*, 1395–1408. [CrossRef]
27. Colomer, M.T.; Jurado, J.R. Structural, Microstructural, and Electrical Transport Properties of TiO_2-RuO_2 Ceramic Materials Obtained by Polymeric Sol-Gel Route. *Chem. Mater.* **2000**, *12*, 923–930. [CrossRef]
28. Wang, X.; Shao, Y.; Liu, X.; Tang, D.; Wu, B.; Tang, Z.; Wang, X.; Lin, W. Phase Stability and Phase Structure of Ru–Ti–O Complex Oxide Electrocatalyst. *J. Am. Ceram. Soc.* **2015**, *98*, 1915–1924. [CrossRef]
29. Ashcroft, N.; Denton, A. Vegard's Law. *Phys. Rev. A* **1991**, *43*, 3161–3164.
30. Özkan, E.; Cop, P.; Benfer, F.; Hofmann, A.; Votsmeier, M.; Guerra, J.M.; Giar, M.; Heiliger, C.; Over, H.; Smarsly, B.M. Rational Synthesis Concept for Cerium Oxide Nanoparticles: On the Impact of Particle Size on the Oxygen Storage Capacity. *J. Phys. Chem. C* **2020**, *124*, 8736–8748. [CrossRef]
31. Sivakami, R.; Dhanuskodi, S.; Karvembu, R. Estimation of Lattice Strain in Nanocrystalline RuO_2 by Williamson-Hall and Size-strain Plot Methods. *Spectrochim. Acta A Mol. Biomol. Spectrosc.* **2016**, *152*, 43–50. [CrossRef]
32. Over, H.; Muhler, M. Catalytic CO Oxidation over Ruthenium—Bridging the Pressure Gap. *Prog. Surf. Sci.* **2003**, *72*, 3–17. [CrossRef]

33. Over, H.; Seitsonen, A.P.; Lundgren, E.; Smedh, M.; Andersen, J.N. On the Origin of the Ru-3$d_{5/2}$ Satellite Feature from RuO_2(110). *Surf. Sci.* **2002**, *504*, L196–L200. [CrossRef]
34. Khalid, O.; Weber, T.; Drazic, G.; Djerdj, I.; Over, H. Mixed $Ru_xIr_{1-x}O_2$ Oxide Catalyst with Well-Defined and Varying Composition Applied to CO Oxidation. *J. Phys. Chem. C* **2020**, *124*, 18670–18683. [CrossRef]
35. Assmann, J.; Narkhede, V.; Khodeir, L.; Löffler, E.; Hinrichsen, O.; Birkner, A.; Over, H.; Muhler, M. On the Nature of the Active State of Supported Ruthenium Catalysts Used for the Oxidation of Carbon Monoxide: Steady-state and Transient Kinetics Combined with in Situ Infrared Spectroscopy. *J. Phys. Chem. B* **2004**, *108*, 14634–14642. [CrossRef]
36. Wang, Z.; Khalid, O.; Wang, W.; Wang, Y.; Weber, T.; Luciano, A.S.; Zhan, W.; Smarsly, B.M.; Over, H. Comparison Study of the Effect of CeO_2-based Carrier Materials on the Total Oxidation of CO, Methane, and Propane over RuO_2. *Catal. Sci. Technol.* **2021**, *11*, 6839–6853. [CrossRef]
37. Walsh, F.; Wills, R. The Continuing Development of Magnéli Phase Titanium Sub-Oxides and Ebonex® Electrodes. *Electrochim. Acta* **2010**, *55*, 6342–6351. [CrossRef]
38. Malik, H.; Sarkar, S.; Mohanty, S.; Carlson, K. Modeling and Synthesis of Magneli Phases in Ordered Titanium Oxide Nanotubes with Preserved Morphology. *Sci. Rep.* **2020**, *10*, 8050. [CrossRef]
39. Wang, Z.; Huang, Z.; Brosnahan, J.T.; Zhang, S.; Guo, Y.; Guo, Y.; Wang, L.; Wang, Y.; Zhan, W. Ru/CeO_2 Catalyst with Optimized CeO_2 Support Morphology and Surface Facets for Propane Combustion. *Environ. Sci. Technol.* **2019**, *53*, 5349–5358. [CrossRef]
40. Wu, J.; Chen, B.; Yan, J.; Zheng, X.; Wang, X.; Deng, W.; Dai, Q. Ultra-active Ru Supported on CeO_2 Nanosheets for Catalytic Combustion of Propane: Experimental Insights into Interfacial Active Sites. *J. Chem. Eng.* **2022**, *438*, 135501. [CrossRef]

2.2 Publication 2: Inserted Hydrogen Promotes Oxidation Catalysis of Mixed $Ru_{0.3}Ti_{0.7}O_2$ as Exemplified with Total Propane Oxidation and the HCl Oxidation Reaction

This publication is on the detailed hydrogen incorporation behavior of the specified Ru_30 sample. Ru_30 sample synthesized by a sol-gel method turns out to be not phase pure but consists of 21 mol% RuO_2 and 79 mol% $Ru_{0.3}Ti_{0.7}O_2$ solid solution. The exposure of hydrogen at elevated temperature causes the reduction of RuO_2 phase while the hydrogen incorporation into the $Ru_{0.3}Ti_{0.7}O_2$ phase. 250 °C turns out to be the optimal temperature for hydrogen insertion and the amount of hydrogen in the lattice is determined to be 17.8 mol% according to the TG-MS. The hydrogenated $Ru_{0.3}Ti_{0.7}O_2$ show remarkable catalytic performance in oxidation catalysis such as propane and HCl oxidation reactions. The inserted hydrogen is not thermally stable and results in activity loss via the formation of water during temperature ramping under reaction mixture. A solution to this issue is to ramp the temperature up to the desired reaction temperature under hydrogen atmosphere and then the gas is switched to the reaction mixture. Subsequent stabilization of hydrogen can be achieved by the continuous supply of the hydrogen from the decomposition of the propane and HCl.

H. Over and I devised the experimental schedule. I prepared $Ru_{0.3}Ti_{0.7}O_2$ mixed oxide catalyst. I performed XRD, SEM, TG-MS, HR-TEM experiments. T. Weber and L. Glatthaar performed XPS measurements. P. Timmer, A. Spriewald-Luciano, Y. Wang and I contributed the construction of propane and HCl oxidation apparatuses and preliminary data analysis. H. Over, B. M. Smarsly, Y. Guo and I contributed through scientific discussion of the data. H. Over and I wrote the draft version of the manuscript. All authors revised the manuscript and have given approval to the final version.

Reprinted from Wang, W.; Timmer, P.; Spriewald-Luciano, A.; Wang, Y.; Weber, T.; Glatthaar, L.; Guo, Y.; Smarsly, B. M.; Over, H. Inserted Hydrogen Promotes Oxidation Catalysis of Mixed $Ru_{0.3}Ti_{0.7}O_2$ as Exemplified with Total Propane Oxidation and the HCl Oxidation Reaction. *Catal. Sci. Technol.* **2023**, 13, 1395. https://doi.org/10.1039/d2cy02000a.

Catalysis Science & Technology

ROYAL SOCIETY OF CHEMISTRY

PAPER

View Article Online
View Journal | View Issue

Cite this: *Catal. Sci. Technol.*, 2023, **13**, 1395

Inserted hydrogen promotes oxidation catalysis of mixed $Ru_{0.3}Ti_{0.7}O_2$ as exemplified with total propane oxidation and the HCl oxidation reaction†

Wei Wang,[ab] Phillip Timmer,[b] Alexander Spriewald Luciano,[b] Yu Wang,[ab] Tim Weber,[b] Lorena Glatthaar,[b] Yun Guo,*[a] Bernd M. Smarsly*[b] and Herbert Over*[b]

Received 22nd November 2022,
Accepted 13th January 2023

DOI: 10.1039/d2cy02000a

rsc.li/catalysis

The solid solution of a reducible oxide with a (non or) less reducible oxide may open the way to incorporate substantial amounts of hydrogen by the simple exposure to H_2 at elevated temperatures, as exemplified with the mixture of RuO_2 and TiO_2. We are able to incorporate 17.6 mol% hydrogen into the mixed oxide $Ru_{0.3}Ti_{0.7}O_2$ by H_2 exposure at 250 °C, while this is not possible for pure RuO_2 and rutile TiO_2 that is either reduced to metallic Ru or does not allow for hydrogen absorption, respectively. Hydrogenated $Ru_{0.3}Ti_{0.7}O_2$ may be utilized in hydrogenation catalysis. In this study, however, we demonstrate that hydrogen-incorporated $Ru_{0.3}Ti_{0.7}O_2$ improves substantially the catalytic performance in oxidation reactions such as the total oxidation of propane and HCl oxidation reaction. Hydrogen induced lattice strain in $Ru_{0.3}Ti_{0.7}O_2$ accompanied with altered electronic properties is likely to be the reason for the observed enhancement in catalytic activity. Hydrogen treatment can also be performed in the reactor, thus providing an additional parameter to fine-tune *in situ* the catalytic performance of a mixed oxide catalyst.

1. Introduction

Hydrogen incorporation in solid materials is mostly associated with the formation of metal hydrides[1] with special focus put on the application of these materials in the field of hydrogen storage. However, the intimate interplay of hydrogen absorption in interstices of bulk-metals and hydrogen adsorption on the surface can be equally important for heterogeneous catalysis, such as reported for Pd-based hydrogenation of alkynes.[2,3]

The hydrogen interaction with oxides is even more complex than with metals.[4] Hydrogen exposure leads frequently to the formation of surface hydroxyl groups, but can also result in hydrogen incorporation into bulk oxide as proton or hydride species. For reducible oxides, hydrogen interaction may even reduce the oxide to pure metals or generate oxygen-deficient oxides that is accompanied by a reduction of the oxidation state of the metal cation.

Up until now, only little is known about the potential of hydrogen insertion to endow metal oxides with superior catalytic performance. A peculiar type of interaction with hydrogen was reported for CeO_2. Here hydrogen exposure leads to formation of hydroxyls at the surface and hydride species H^- in bulk CeO_2.[5–9] Hydride formation is facilitated by oxygen vacancies and accompanied by the oxidation of Ce^{3+} to Ce^{4+} which may explain the remarkable catalytic performance of CeO_2 in the partial hydrogenation of alkynes to alkenes.[10–12]

Upon H_2 exposure at high temperatures (600–1000 °C), TiO_2 can be bulk-reduced to the Magneli phases down to Ti_2O_3.[13,14] At lower temperatures, theory[15,16] and experiments[17–19] indicate that traces of hydrogen can form deep donor levels in rutile TiO_2 forming $O–H^+$ complexes, while hydrogen in O vacancies can be stabilized as hydride H^- species.

Hydrogen exposure to RuO_2 is not able to form hydrous RuO_2 or solid suboxides.[20] Hydrogen treatment at temperatures above 130 °C leads instead to chemical reduction of RuO_2 that comes along with a phase separation into RuO_2 and metallic ruthenium on the nanoscale.[20,21] Hydrous RuO_2 can however be formed by anodic polarization of metallic Ru (ref. 22) or by hydrothermal

[a] *Key Laboratory for Advanced Materials, Research Institute of Industrial Catalysis, School of Chemistry and Molecular Engineering, East China University of Science and Technology, Shanghai 200237, PR China. E-mail: yunguo@ecust.edu.cn*
[b] *Institute of Physical Chemistry, Justus Liebig University, Heinrich-Buff-Ring 17, D-35392 Giessen, Germany. E-mail: Bernd.Smarsly@phys.chemie.uni-giessen.de, Herbert.Over@phys.chemie.uni-giessen.de*

† Electronic supplementary information (ESI) available. See DOI: https://doi.org/10.1039/d2cy02000a

treatment of Ru precursors.[23] Hydrous RuO_2 turned out to be a remarkably active catalyst in the oxidative dehydration of alcohols.[24–27] The superior activity of hydrous RuO_2 was reported to be correlated with its electrochemical capacitance, *i.e.*, the amount of hydrogen that can reversibly be incorporated or extracted.[26,28]

In this study we will introduce a quite general approach to insert hydrogen into RuO_2 based materials, thereby affecting the catalytic oxidation activity. In doing so, we prepare a solid solution of RuO_2 with less-reducible rutile TiO_2, aiming at modifying the reduction behavior with H_2. In particular, we synthesize a mixed oxide with the composition $Ru_{0.3}Ti_{0.7}O_2$. This specific concentration of Ru of 30 mol% is chosen to be compatible with the Ru concentration of dimensionally stable anodes (DSA[29]) employed in the large scale industrial process of chlorine evolution reaction. We will show that upon exposure to hydrogen at 250 °C, $Ru_{0.3}Ti_{0.7}O_2$ is able to insert 17.6 mol% hydrogen into the rutile lattice. Catalytic tests of H-inserted $Ru_{0.3}Ti_{0.7}O_2$ are conducted for two industrially relevant oxidation reactions, namely the total oxidation of propane and the HCl oxidation reaction. Catalytic propane oxidation is an important reaction for exhaust after treatment of liquid petroleum gas propelled engines.[30] The gas-phase HCl oxidation to Cl_2 is applied on a large scale to recover Cl_2 from HCl being generated in diverse industrial chemical processes, for instance in the production of polycarbonates.[31] For both catalytic oxidation reactions, H-inserted $Ru_{0.3}Ti_{0.7}O_2$ reveals significantly higher catalytic activity than H-free $Ru_{0.3}Ti_{0.7}O_2$.

2. Experimental details

2.1 Preparation of catalysts

The mixed ruthenium–titanium powder material with 30 mol% Ru is prepared by a conventional sol–gel method and is referred to as Ru_30 (pure RuO_2 prepared by sol–gel method is referred to Ru_100). For the synthesis of Ru_30 we apply the following procedure: 4.6 g anhydrous citric acid (CA) is dissolved into 40 mL deionized water at 60 °C using a water bath. 1.4 mmol titanium butoxide (Sigma-Aldrich, 97%) is dissolved in 5 mL anhydrous ethanol and then mixed with the above CA solution. Subsequently, 0.6 mmol $RuCl_3{\cdot}xH_2O$ (Sigma-Aldrich, molecular weight: 228.13 g mol^{-1}, determined by TG–MS) is added and the clear brown solution is continuously stirred for 15 min while mildly heated up to 80 °C, thereby leading to the complete complexation of the metal cations. Next the pH of the solution is adjusted to 6 by an ammonia solution (2 M), during which the solution remains dark brown and transparent. Finally, the solution is heated to 90 °C to evaporate the solvent. The resulting dark green gel is directly transferred into a 120 °C drying oven overnight, and the obtained black foam-like material is finely ground and calcined at 450 °C for 4 h with a heating rate of 2 °C min^{-1}. The final Ru_30 powder sample is ground again for the characterization and catalytic experiments.

Hydrogen incorporation experiments are conducted by exposing a fresh Ru_30 mixed oxide catalyst to 4 vol% H_2/N_2 (50 sccm min^{-1}) at different temperatures y in degree Celsius for 3 hours (referred to Ru_30_yR). After cooling down under the same atmosphere, the obtained catalyst is thoroughly characterized before and after catalytic tests. The re-oxidation experiment is conducted in the same apparatus by switching the gas atmosphere to 50 sccm of dry air at a temperature z in degree Celsius (referred to as Ru_30_yR_zO). The blank sample calcined in pure N_2 is referred to as Ru_30_yN.

2.2 Characterization of catalysts

Powder X-ray diffraction (XRD) measurements are conducted on a PANalytical Empyrean diffractometer employing a Cu K_α source (40 kV, 40 mA). LaB_6 standard (NIST) is mixed with the samples to correct for a potential 2θ shift due to varying sample holder positions. The crystallite size is calculated by the Scherrer equation, while the composition of the catalyst is determined by Vegard's law and energy dispersive X-ray spectroscopy (EDS) employing a scanning electron microscopy (SEM) HREM Merlin instrument (Carl Zeiss MicroImaging GmbH, Göttingen, Germany).

The samples are pre-treated at 100 °C for 12 h in vacuum before performing Kr physisorption experiments with an Autosorb 6 instrument (Quantachrome). The BET (Brunauer–Emmett–Teller) method is applied to determine the specific surface area.

Morphology and elemental distribution of the catalyst are analyzed by aberration-corrected scanning transition electron microscopy (STEM) operated on a ThermoFisher Themis Z transmission electron microscope equipped with two aberration correctors. High-angle annular dark-field (HAADF) STEM images are recorded using a convergence semi-angle of 25 mrad and inner and outer collection angles of 47 and 200 mrad, respectively. Bright field images are acquired using ThermoFisher Talos F200X. Energy dispersive spectroscopy (EDS) is carried out with a four in-column Super-X detector. Copper mesh grids are used for the sample preparation.

The concentration and chemical state of the Ru_x samples in the near surface region is quantified by X-ray photoelectron spectroscopy (XPS, PHI VersaProbe II). The photon energy is 1486.6 eV (monochromatized Al-Kα line). XPS spectra are analyzed with the CasaXPS software (Version 2.3.17).

Thermogravimetric (TG)-analysis is performed on a STA 409PC thermoscale (Netzsch) in combination with a QMG421 quadrupole mass spectrometer (MS) from Balzers with an ionization energy of 70 eV. A temperature range between 25 and 500 °C is analyzed with a heating rate of 10 °C min^{-1} in synthetic air (30 sccm min^{-1}).

2.3 Catalytic measurements

A home-built flow reactor is used to determine the catalytic propane oxidation activity of the catalysts.[32] The apparatus comprises the gas supply, the quartz tube reactor (6 mm inner diameter), furnace and a nondispersive infrared

(NDIR)-sensor to quantify volumetric CO/CO_2 and C_3H_8 concentration. The purities of the used gases are 3.5 and 4.8 for C_3H_8 and O_2, respectively. Typically, 20 mg of powder catalyst mixed with 40 mg quartz sand is employed in the test. The feed gas consists of 1 vol% C_3H_8, 5 vol% O_2 that is balanced by 94 vol% N_2. The total mass flow rate is set to 100 cm^3 STP min^{-1} (sccm), controlled by digital mass flow controllers (MKS Instruments 1179B). This that corresponds to a weight hourly space velocity (WHSV) of 345 000 mL g^{-1} h^{-1}. The temperature of the catalyst bed can be varied from room temperature to 250 °C at a rate of 1 K min^{-1}. The propane conversion is calculated by the following equation:

$$X_{C_3H_8} = \frac{c(CO_2)}{c_{max}(CO_2)}$$

where $c(CO_2)$ is the concentration of CO_2 at the outlet of the reactor during temperature ramp and $c_{max}(CO_2)$ is the full-conversion-state concentration of CO_2. Additionally, the concentration of propane is recorded during the reaction to countercheck the determined conversion. The conversions based on CO_2 and C_3H_8 are virtually identical, indicating that no other by-product is formed. When propane is fully consumed, the concentration of CO_2 turns out to be three times that of the propane concentration at the inlet. CO is not detected during the entire temperature range of the catalytic test. Altogether, the carbon mass is balanced and the selectivity towards CO_2 is 100%. The space time yield (STY) defined as the molar amount of product per time and per mass catalyst is used as descriptor to evaluate the catalytic activity in propane oxidation reaction.

Catalytic HCl oxidation measurements are conducted in another homebuilt fixed-bed reactor.[33] The reactor setup includes the gas supply, the quartz tube reactor (6 mm inner diameter), furnace, and UV-vis analytics for chlorine quantification. The following gases are used: HCl 4.5, O_2 5.0, and Ar 5.0, and the flow rates are controlled by digital mass flow controllers (MKS Instruments 1179B). The product analysis is accomplished by a fiber-optic UV-vis spectrometer (Ocean Optics USB4000 with a DH-2000-BAL light source) with a Z-shaped flow cell (Teflon, 50 mm optical path length, FIAlab). The absorbance at a wavelength of λ_{max} = 329 nm (absorption maximum of chlorine) is proportional to the chlorine space time yield (STY). For activity tests, 20 mg catalyst is exposed to a reaction mixture, containing 3 sccm HCl, 1.5 sccm O_2 and 10.5 sccm Ar, and a total flow rate 15 sccm min^{-1}. The temperature of the catalyst bed can be varied from room temperature to 450 °C at a rate of 5 K min^{-1}.

3. Experimental results

3.1 Characterization of the fresh ruthenium–titanium mixed oxides samples

The XRD patterns of freshly prepared ruthenium–titanium mixed oxide Ru_30 and Ru_100 are depicted in Fig. 1a; for comparison reason the XRD pattern of pure commercial rutile TiO_2 is overlaid. For the pure ruthenium sample Ru_100, reflections from both a rutile structure and metallic Ru (hcp structure) are discernible. The formation of metallic Ru is commonly observed for such syntheses involving organic complexation agents that can act as reducing agent during the beginning of the reaction. However, for Ru_30 no reflections from metallic Ru are observed, which we attribute to the lower amount of Ru present in the solution. With the addition of titanium, the rutile structure in XRD patterns is preserved, although the (110) and the (101) reflections shift towards the reflections of pure rutile TiO_2. The rutile related diffraction peaks of Ru_30 split into two components, thus manifesting a notable phase separation. The positions of the sharp reflections appearing at 28.02° from rutile (110) and 2θ = 35.07° from rutile (101) are ascribed to the pure RuO_2 phase, while those at 2θ = 27.56° and 2θ = 35.70° are assigned to mixed $Ti_{1-x}Ru_xO_2$. Here we utilize LaB_6 as reference to precisely determine the peak positions. It turns out that the observed variation of LaB_6 peak positions among the various samples are only 0.01° so that in further XRD experiments (Fig. 2) we refrain from using LaB_6 as reference. The existence of pure RuO_2 in the Ru-rich mixed $Ti_{1-x}Ru_xO_2$ was already reported in a previous study using a similar polymer assisted preparation method.[34] The coexistence of pure RuO_2 and mixed

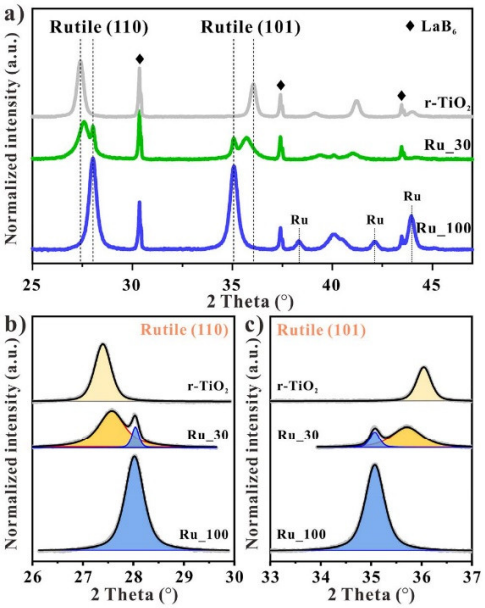

Fig. 1 (a) XRD patterns of the pure rutile r-TiO_2, Ru_100 and the ruthenium–titanium mixed oxide Ru_30. (b) Peak deconvolution of rutile (110) and (101) reflections in pure RuO_2 (blue) and mixed oxide $Ru_{0.3}Ti_{0.7}O_2$ (orange).

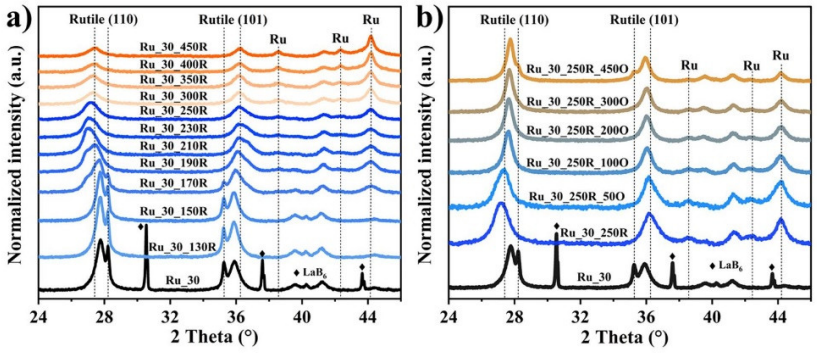

Fig. 2 (a) XRD patterns of Ru_30 catalysts treated in 4 vol% H_2/N_2 at different temperatures indicated (Ru_30_*y*R, *y* = reduction temperature). (b) XRD patterns of Ru_30_250R catalysts after re-oxidation at different temperatures indicated (Ru_30_250R_*z*O, *z* = oxidation temperature). The dashed lines correspond to the position of pure RuO_2 and rutile TiO_2. All XRD patterns are acquired at room temperature.

$Ti_{1-x}Ru_xO_2$ in a wide range of composition indicates a profound miscibility gap in agreement with a recent DFT study.[35]

In Fig. 1b, we present the peak deconvolution of the rutile (110) reflection, while that of the (101) reflection is shown in Fig. 1c. As a main result of the decomposition, the peak positions of Ru–Ti solid solution can be used to derive the lattice parameters $a = b = 4.5718$ Å and $c = 3.0059$ Å of the mixed oxide. Assuming the validity of Vegard's law,[36] the composition of the mixed Ru–Ti oxide component is estimated to be 30 ± 3% (*cf.* Fig. S1†) in good agreement with the nominal composition. From the relative integral intensities (in Fig. 1b and c) of the (110) and (101) reflection of the mixed oxide component and the pure RuO_2 component of Ru_30, the total amount of mixed oxide and RuO_2 was calculated from the (110) as well as the (101) reflections, providing average values of 79 ± 3 mol% and 21 ± 3 mol% respectively. Based on the width of these reflections the crystallite sizes derived by the Scherrer equation are 12 ± 2 nm for Ru_30 and 43 ± 5 nm for Ru_100, respectively (*cf.* Table 1). We note that the effect of microstrain on the calculation of the crystallite size, using the Williamson–Hall method, is only marginal for $Ru_{0.3}Ti_{0.7}O_2$ and pure RuO_2. We attribute the absence of a significant degree of structural disorder in the crystal structure for $Ru_{0.3}Ti_{0.7}O_2$ to the quite similar ionic radii of Ti and Ru in the formal oxidation state 4+. Thus, the incorporation of Ru into the rutile crystal lattice only generates minute microstrain.

With STEM and element mapping the morphology and the local composition of the Ru_30 sample is studied (*cf.* Fig. S2†). From the homogeneous distribution of Ti and Ru in element mapping it is obvious that a mixed oxide $Ru_xTi_{1-x}O_2$ has formed with a local Ru concentration of 26 ± 4 mol%. Occasionally, large RuO_2 particles (>50 nm diameter) are observed (*cf.* Fig. S2†).

With XPS we can determine the surface/near-surface composition of the mixed oxide Ru_30 catalyst in comparison with that of Ru_100 (*cf.* Fig. S3,† and the fitting parameters are provided in Table S1†). From the Ru 3d XP spectrum we can clearly see that ruthenium is exclusively in the Ru^{4+} oxidation state that is further supported by the pronounced satellite features. The O1s spectrum in Fig. S4† (fitting parameters are given in Table S1†) exhibits two chemical states of near surface oxygen: one is the O^{2-} from the lattice oxygen at ~529 eV, and the other, a shoulder peak at higher binding energy (around 531.8 eV), is ascribed to surface OH.

In order to quantify the surface composition of ruthenium and titanium, we measured Ru 3p and Ti 2p XPS spectra and performed peak deconvolution since these peaks overlap (*cf.* Fig. S5;† fitting parameters are collected in Table S1†). For the Ru_30 catalyst, the surface concentration of ruthenium turns out to be 29.1 mol%. Employing EDS–SEM with a

Table 1 Physicochemical propertied including compositional information of Ru–Ti mixed oxides catalysts

Catalyst	Cell parameter a/b^a (Å)	Cell parameter c^b (Å)	Grain size $(RuO_2)^c$ (nm)	Grain size $(Ru–Ti)^c$ (nm)	Ru–Ti/(RuO_2 + Ru–Ti)^d (%)	Ru/(Ru + Ti)^e (%)	Ru/(Ru + Ti)^f (%)	BET surface area ($m^2\ g^{-1}$)
Ru_100	4.4998	3.1069	18 ± 0.5	—	100	100	100	9
Ru_30	4.5718	3.0059	43 ± 5	12.0 ± 2	79 ± 3	30.0	29.1	31
Ru_30_250R	4.6381	2.9373	—	12.2 ± 3	—	29.8	31.1	30

[a] Calculated by rutile (110) reflection of the Ru–Ti solid solution phase. [b] Calculated based on obtained *a*/*b* value and rutile (101)/(101) reflections of the Ru–Ti solid solution phase. [c] Determined by Williamson–Hall method. [d] Determined by peak deconvolution of the XDR reflections from 25–45°. [e] Obtained from SEM–EDS mapping. [f] Calculated from XPS.

detection depth of several micrometers, the bulk composition of Ru_30 is determined to be 30 mol% Ru, in good agreement with the nominal composition of Ru_30. Krypton physisorption experiments provide a BET surface area of 31 m^2 g^{-1} (for Ru_30). Table 1 summarizes the derived properties of Ru_30 and Ru_100.

3.2 Hydrogen incorporation into ruthenium–titanium mixed oxides

In the following we discuss the hydrogen incorporation of Ru_30. XRD in Fig. 1 reveals that Ru_30 consists of a mixture of RuO_2 and $Ru_{0.3}Ti_{0.7}O_2$ mixed oxides. The hydrogen treatment involves the exposure of Ru_30 to 4% H_2/N_2 for 3 h at various temperatures ranging from 130 °C (Ru_30_130R) to 450 °C (Ru_30_450R). Note that the XRD measurements are performed after cooling down the mixed oxide to room temperature. As indicated in Fig. 2a, the diffraction peak of RuO_2 at $2\theta = 28.02°$ starts to decline at 150 °C and completely disappears at 190 °C. Concomitantly, the intensity of Ru metal related diffraction increases in intensity. These changes imply that the pure RuO_2 particles are reduced to metallic ruthenium at temperature below 200 °C, fully consistent with previous surface science studies of RuO_2(110).[21] Quite in contrast, the rutile reflections (110) and (101) of the mixed oxide phase persist and shift to lower and higher diffraction angles, respectively, upon exposure to 4% H_2/N_2 and increasing the temperatures. At 250 °C, *i.e.*, for Ru_30_250R, only a single and symmetric signal shows up at $2\theta = 27.16°$, a position that is lower than that of pure rutile TiO_2 (110). The corresponding cell parameters together with the bulk compositions are collected in Table 1. However, even H_2 treatment at 450 °C leaves the rutile structure of Ru_30 stable, shifting the (110) peak little less than for the 250 °C reduction treatment.

With HRTEM the topography of Ru_30_250R is imaged and presented in Fig. 3a. The mixed oxide is clearly visible in the overlay of Ti and Ru element mappings (*cf.* Fig. 3b), showing a homogeneous distribution of Ru and Ti after the 250 °C reduction treatment. The fringes in Fig. 3a indicate (110) facets of rutile. As seen in the magnified image in Fig. 3c, these fringes are due to regular rows of spots (columns of Ti and Ru cations) with varying intensity. This intensity variation (Fig. 3d) is due to different compositions of these columns, with higher concentrations of Ru in the higher intensity spots. In Fig. 3c we can also discern a twin grain boundary. Notably, the fringes of rutile (110) facets (*cf.* Fig. 3a and c) indicate a layer spacing of $d \approx 3.4$ Å, indicating a clear expansion compared to the unreduced Ru_30 with $d \approx 3.3$ Å (*cf.* Fig. S6†) that is in qualitative agreement the XRD derived data. Altogether, HRTEM data strongly evidence that the mixed oxide phase is preserved upon exposure to 4% H_2/N_2 at 250 °C. On other positions of the sample, the mixed oxide is shown to be partly decorated by Ru-rich particles (*cf.* Fig. S7†). The overlay of O and Ru indicates that these Ru-rich particles are composed of metallic Ru, while the oxide is

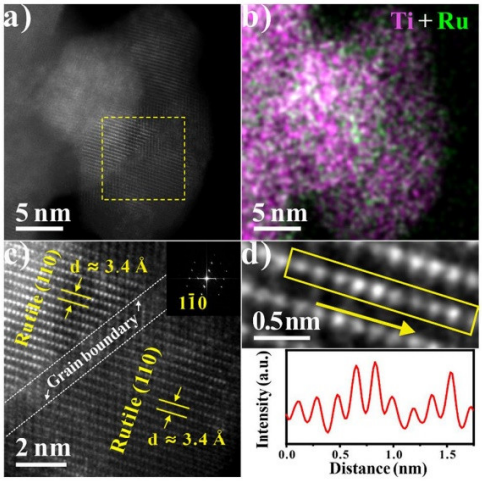

Fig. 3 (a) Aberration-corrected HAADF-STEM images of Ru_30_250R sample. (b) EDS mapping of the same region shown in (a): green = Ru, magenta = Ti. (c) HAADF-STEM images of the selected yellow dotted region in (a). (d) Enlarged aberration-corrected HAADF-STEM images of Ru_30_250R along the rutile (110) direction and intensity analysis from the rectangle box along the arrow (yellow).

always present as mixed oxide. These large Ru particles stem from the reduction of the RuO_2 particles.

To highlight the particular behavior of Ru_30 in the hydrogen treatment, we carry out hydrogen incorporation experiments with Ru_100 and pure rutile TiO_2 for comparison reason. As summarized in Fig. S8,† Ru_100 is fully transformed to metallic Ru under 4% H_2/N_2 at 250 °C, while for TiO_2 there is no change observed at all in the XRD pattern.

To further study the redox properties of Ru_30, the Ru_30_250R sample is subject to re-oxidation that is conducted at elevated temperatures up to 450 °C (Fig. 2b). Upon exposure to air at 50 °C, the (110) and (101) reflections start to shift in position while maintaining the FWHM. Further increase of temperature to 100 °C in air the peak positions keep shifting and the diffraction profiles sharpen considerably. Since a temperature of 100 °C is far too low to cause an increase of the crystallite size, these experiments clearly indicate that the hydrogen-induced FWHM increase of hydrated $Ru_{0.3}Ti_{0.7}O_2$ (110) component is due exclusively to micro strain. This view is fully supported by a detailed Williams–Hall analysis (*cf.* Table S2†). The microstrain decreases form 1.2% for Ru_30_250R to 0.2% for Ru_30_250R_100O. The micro strain is induced by hydrogen incorporation that reversibly diminishes by hydrogen removal during oxygen exposure at high temperatures. Final oxidation at 450 °C leads to the rutile diffraction signals (shape and position) that are identical to those of the pristine $Ru_{0.3}Ti_{0.7}O_2$. This means that the Ru–Ti mixed oxide phase can be fully recovered upon oxidative treatment. Above 100 °C the Ru

metal signals decrease in intensity and at 450 °C the RuO_2 peaks re-appear as shoulder at the (110) and (101) positions. A cycled hydrogen incorporation/re-oxidation experiment is applied to test the reversibility of the mixed oxides structure. The XRD results are summarized in Fig. S9,† evidencing that during three redox cycles at higher temperatures, the structure can reversibly be switched between mixed $Ru_{0.3}Ti_{0.7}O_2$ oxide phase and the hydrogenated $Ru_{0.3}Ti_{0.7}O_2$ oxide.

To learn more about the process of hydrogen incorporation into Ru_30 sample, the (110) and the (101) reflections are analyzed by decomposition into up to three components (*cf.* Fig. 4); one component is related to pure RuO_2 (blue) the other two (green and red) are related to hydrogenated $Ru_{0.3}Ti_{0.7}O_2$ with different hydrogen concentrations causing different lattice distortions. The reflections of the untreated Ru_30 sample can be decomposed into a narrow contribution of pure RuO_2 (blue) and one that is related to mixed oxide $Ru_{0.3}Ti_{0.7}O_2$ (green). Hydrogen treatment at 150 °C for three hours does not cause any change in the diffraction features of (110) and (101) reflections. Upon hydrogen treatment at 170 °C, the green component shifts slightly and a third component (red) appears that is even farther shifted toward the TiO_2-related diffraction peaks. Increasing the temperature to 190 °C, the red component gains in intensity, sharpens and shifts slightly, while the green component continues to shift and broadens significantly. The pure RuO_2 component (blue) disappears. Upon hydrogen treatment at 210 °C, the green component shifts without increasing the FWHM and the red component loses intensity, but does not shift further. Upon further increasing the temperature of hydrogen treatment to 230 °C, the green component remains constant, while the red component diminishes and disappears finally at 250 °C. Detailed parameters of all the peak deconvolutions of rutile (110) and rutile (101) are compiled in Table S3.† The main result of this analysis is that RuO_2 is chemically reduced while the mixed $Ru_{0.3}Ti_{0.7}O_2$ incorporates hydrogen upon hydrogen treatment at 250 °C that shifts the 2θ positions of the (110) and (101) reflections towards those of TiO_2 (macrostrain), while the FWHM increases substantially due to the formation of microstrain.

Employing TG–MS the amount of hydrogen incorporated into the lattice of Ru_30_250R is quantified by the amount of water that is produced by the reaction of incorporated hydrogen with oxygen during heating the sample in ambient air. The derived value is counterchecked by the corresponding mass loss in TGA. As reference a nitrogen-treated sample Ru_30_250N sample is used. As depicted in Fig. 5, a little mass signal for H_2O (m/z = 18) originating from the water desorption is already evident at 80 °C for Ru_30_250N, while for Ru_30_250R a broader and stronger signal can be recognized. This latter water peak consists actually of two components, one related to water desorption (80 °C) and a second that is associated with the oxidation of incorporated hydrogen (maximum at 130 °C). A peak temperature of 130 °C agrees reasonably well with the temperature where significant changes in XRD (Fig. 2b) occur during re-oxidation. Employing a deconvolution procedure as shown in Fig. 5 the amount of inserted hydrogen can be quantified from the integral area of the difference of Ru_30_250R and Ru_30_250N. The molar fraction of inserted hydrogen for Ru_30_250R turns out to be 17.6 mol% (see ESI† for the raw data, Fig. S10). A similar analysis is carried out for Ru_30_450R (see ESI,† Fig. S11), resulting in a concentration of incorporated hydrogen of 6.6 mol%. The lower concentration is reconciled with a smaller shift of the (110) and (101) reflections in Fig. 2a.

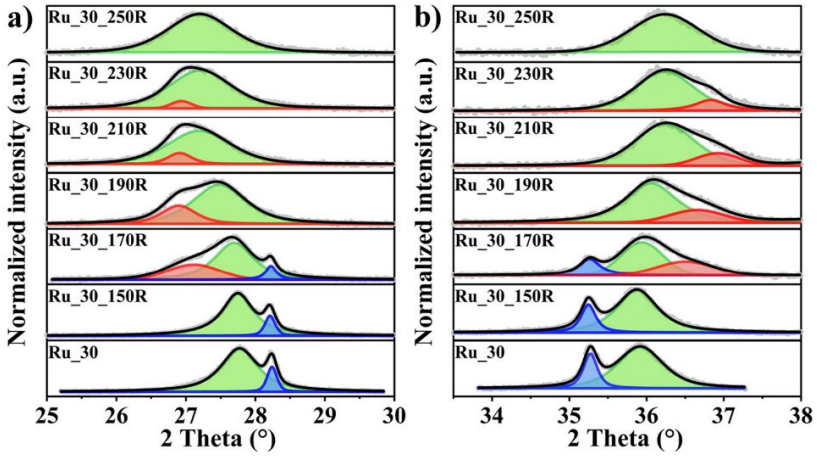

Fig. 4 (110) (a) and (101) (b) reflection of Ru_30 and how these reflections evolve with hydrogen treatment at various temperatures ranging from 150 °C to 250 °C. The reflections are decomposed into up to three components: one component is related to pure RuO_2 (blue) the other two (green and red) are related to hydrogenated $Ru_{0.3}Ti_{0.7}O_2$ with different hydrogen concentrations causing different lattice distortions.

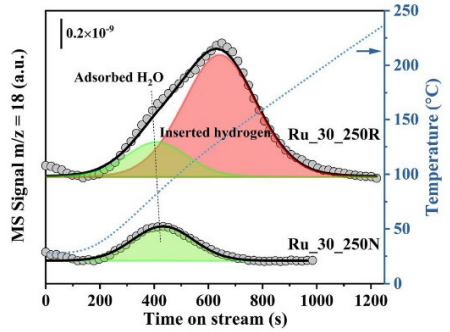

Fig. 5 Peak deconvolution of H_2O signal (m/z = 18) of the Ru_30_250R and Ru_30_250N from TG–MS analysis.

In Fig. 6 XP spectra of Ru 3d of Ru_30 are compared to those of the hydrogen treated Ru_30_250R sample and the re-oxidized one Ru_30_250R_300O. The spectra can be fitted by three components, namely metallic Ru, Ru^{4+} and the satellite feature of Ru^{4+}. For clarity reasons, the carbon C 1s component is removed from the spectra. The Ru_30 sample reveals only Ru^{4+} (red) and the corresponding satellite features (blue). This is consistent with the XRD (Fig. 4) that shows only diffraction peaks based on the mixed oxide $Ru_{0.3}Ti_{0.7}O_2$ and pure RuO_2. In both oxides Ru is exclusively in the 4+ oxidation state. Upon hydrogen treatment at 250 °C, a strong metallic Ru peak appears in the Ru 3d spectrum (green). This metallic component originates from the reduction of RuO_2 at 250 °C towards metallic Ru, as evidenced by XRD. The molar concentration of metallic Ru corresponds to 24 mol% in reasonable agreement with that concluded from XRD (21 ± 3 mol%). Therefore, the observed Ru^{4+} component is that of Ru in mixed $Ru_{0.3}Ti_{0.7}O_2$. Upon re-oxidation of Ru_30_250R at 300 °C (Ru_30_250R_300O), the metallic component diminishes and the Ru^{4+} concentration is largely recovered. From these experiments we conclude that the oxidation state of Ru in $Ru_{0.3}Ti_{0.7}O_2$ is preserved, regardless of the chemical treatment (hydrogen treatment or re-oxidation). Quite surprising, the binding energy of the satellite feature (blue) reveals a significant shift towards lower binding energy when treated with hydrogen, while this shift is restored during the re-oxidation process.

In principle hydrogen reduction could also reduce Ru from $Ru_{0.3}Ti_{0.7}O_2$. This process can be excluded. On reduction treatment at 250 °C, we found that the rutile structure is preserved (XRD (Fig. 2a) and TEM (Fig. 3)) and the rutile structure persists as a mixture of Ti and Ru (element mapping and "atomically" resolved STEM in Fig. 3). The XPS analysis indicates that overall the Ru_30_250R sample still contains 76 mol% of Ru^{4+}. The most compelling evidence for the stability of the $Ru_{0.3}Ti_{0.7}O_2$ after reduction treatment is provided by the re-oxidation experiments in Fig. 2b. From XRD we see that the rutile diffraction peaks of $Ru_{0.3}Ti_{0.7}O_2$ are fully recovered after re-oxidation above 250 °C. In particular rutile diffraction peaks shift back to those positions of Ru_30 (with identical intensity), thus evidencing that the mol% of Ru in the mixed rutile structure has been preserved (Vegard's law).

In addition to the Ru 3d, Ti 2p XP spectra are summarized in the ESI† (Fig. S12) for Ru_30, hydrogen treated Ru_30_250R sample, and the re-oxidized one Ru_30_250R_300O. All spectra indicate Ti^{4+} and no sign of Ti^{3+}. The overall near-surface composition of Ru_30_250R is given in Table 1. Corresponding O1s spectra in Fig. S13† exhibit two components, one related to O^{2-} and the other assigned to OH species. However, the OH feature does not vary when Ru_30 is exposed to hydrogen or is re-oxidized, suggesting that incorporated H does not change the concentration of OH species.

3.3 Catalytic tests: total oxidation of propane and HCl oxidation reaction

In the following we present catalytic tests of Ru_30 and Ru_30_250R for two oxidation reactions in order to study the effect of incorporated H in $Ru_{0.3}Ti_{0.7}O_2$ on the catalytic performance. Since we know already that incorporated H is quite labile and leaves the mixed oxide under oxidizing reaction conditions above 50 °C, we select deliberately oxidation

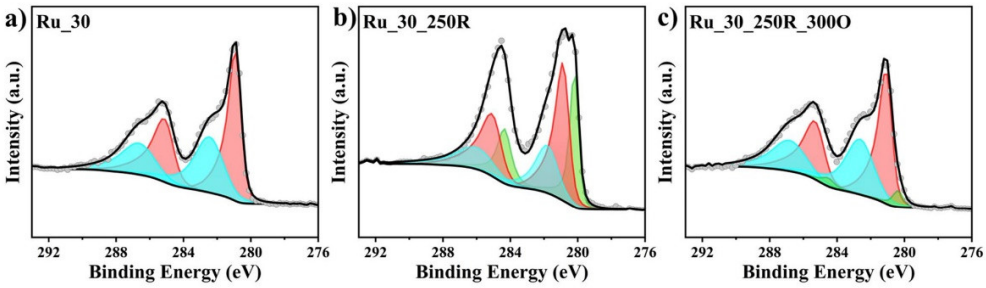

Fig. 6 XP spectra of Ru_30 (a) in comparison with a hydrogen treated sample at 250 °C (b) Ru_30_250R and re-oxidized sample at 300 °C (c) Ru_30_250R_300O. Using the CasaXPS software, the Ru3d spectra are decomposed into four components: Ru^{4+} (red), satellite Ru^{4+} (blue), metallic Ru (green), and C1s. For clarity reasons the C1s signal is removed from the experimental spectra.

reactions that supply the catalyst surface continuously with hydrogen, namely total oxidation of propane and HCl oxidation.

Total oxidation of propane. For the propane oxidation reaction (1% C_3H_8 and 5% O_2 balanced by 94% N_2) at 170 °C the catalytic performance of Ru_30 is compared to that of Ru_30_250R in Fig. 7a. The STY of Ru_30 is shown when increasing the reaction temperature from 30 °C to 170 °C, maintaining 170 °C for 5 h and reducing subsequently the temperature back to room temperature. This temperature cycling is conducted three times, reaching in all cases STY values of 0.5 mol of CO_2 per kg cat^{-1} h^{-1} at 170 °C. This finding demonstrates that the activity of Ru_30 is stable under these conditions. With the Ru_30_250R the very same protocol is carried out (Fig. 7a). Here within the first temperature cycle the activity of Ru_30_250R is significantly enhanced and the activity at 170 °C is stable at STY = 2.7 mol of CO_2 per kg cat^{-1} h^{-1}. In the second cycle the activity is reduced to 1.3 mol of CO_2 per kg cat^{-1} h^{-1}, but still substantially higher than that of Ru_30. Again the activity at 170 °C is constant, *i.e.*, no further deactivation takes place at constant reaction temperature. In the third cycle the achieved activity is identical to that reached in the second cycle. The Ru_30_250R catalyst runs now stable also when cycling the temperature.

In order to determine the chemical nature of the active phase, the degree of hydrogen insertion in Ru_30_250R is estimated from XRD (*cf.* Fig. 8a) after the catalytic test experiments. Clearly, the signature for H insertion is much less developed (see Ru_30_250R_C_3H_8/O_2_3 cycles in Fig. 8a). Both the FWHM and the peak position change towards those of Ru_30_250R_300O. However, the final peak position is still (albeit only slightly) shifted when compared to Ru_30_250R_300O, evidencing that some inserted hydrogen is left in sample Ru_30_250R_C_3H_8/O_2_3cycles after the catalytic tests.

Since the activity of Ru_30_250R at 170 °C is always constant during a reaction time of 5 h, the loss of hydrogen must occur during the temperature ramps in the first temperature cycle. For this reason, we designed another propane oxidation experiment with Ru_30_250R, where during both the heating and the cooling ramp 4% H_2 in Ar is exposed and only when the reaction temperature of 170 °C is reached the feed is switched to the (1% C_3H_8 + 5% O_2) reaction mixture. These samples are referred to Ru_30_250R_H_2. As depicted in Fig. 7b, the activity at 170 °C is now substantially enhanced (4.3 mol of CO_2 per kg cat^{-1} h^{-1}) in comparison to the case without *in situ* H_2 treatment during temperature ramping, and the high activity is maintained during the next temperature cycles. Actually, the catalytic activity of Ru_30_250R is now one order of magnitude higher than for Ru_30. The XRD pattern (*cf.* Fig. 8a) after these catalytic tests indicates that the degree of H insertion of Ru_30_250R_H_2 after three reaction cycles is high and halfway between that of Ru_30 and Ru_30_250R (*cf.* Table S2†).

In addition, we compare in Fig. 8b conversion curves for the total oxidation of propane over Ru_30_250R, where during temperature ramping 4% H_2/Ar is supplied, with that of Ru_30. Ru_30 is substantially less active than Ru_30_250R, reaching 95% conversion at 240 °C. With the hydrogen treated sample Ru_30_250R 95% conversion is achieved at 200 °C that is 40 °C lower than for Ru_30.

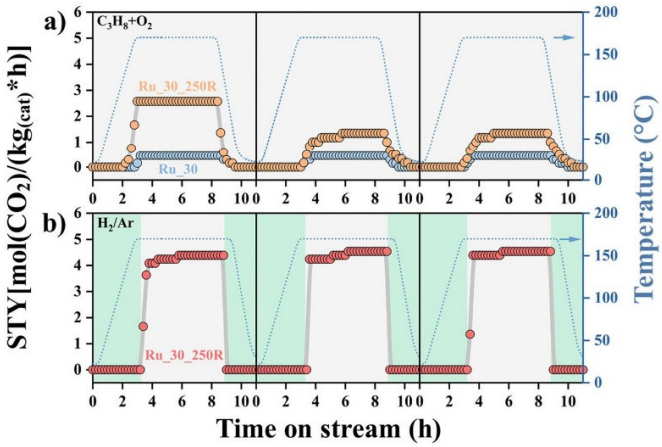

Fig. 7 (a) STY as a function of reaction time of catalytic propane oxidation over Ru_30 and Ru_30_250R when cycling the reaction temperature from 30 °C to 170 °C (blue dotted line). The grey background represents total C_3H_8 oxidation conditions: 1 vol% C_3H_8, 5 vol% O_2, balanced by N_2; total volume flow: 100 sccm min^{-1}, temperature ramp: 1 K min^{-1}. (b) for Ru_30_250R, during heat ramping the reaction mixture is switched to 4% H_2/Ar with total volume flow of 50 sccm min^{-1} (green background). When reaching 170 °C, the gas composition is switched to the reaction mixture (grey background).

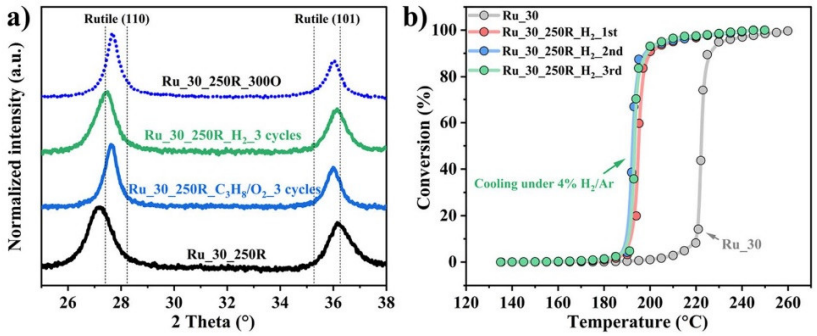

Fig. 8 (a) XRD data before and after cyclic experiments at 170 °C for Ru_30_250R. The dotted lines are guide lines to follow the shift in 2θ. Total C_3H_8 oxidation reaction conditions: 1 vol% C_3H_8, 5 vol% O_2, balanced by N_2; total volume flow: 100 sccm, temperature ramp: 1 K min^{-1}. (b) Full conversion curves of catalytic propane oxidation over Ru_30 and Ru_30_250R as a function of reaction temperature, when cycling the reaction temperature from 30 °C to 250 °C. For Ru_30_250R, during the cooling stage after each cycle, the gas is switched to 4% H_2/Ar.

In next set of experiments we study the total oxidation of propane at 170 °C starting from Ru_30 and then activate *in situ* the Ru_30 sample with 4% H_2/N_2 at 250 °C in the reactor. The appeal of this approach is that the activity can directly be compared without facing the problem that the catalyst loading or the catalyst bed has changed from one sample to the next. From inspection of Fig. S14a,† the activity increases by almost one order of magnitude due to this hydrogen-induced activation step, independent at which stage the *in situ* reduction is performed. A control experiment (*cf.* Fig. S14b†) is conducted with Ru_100, indicating that the oxidized sample Ru_100 is significantly more active than Ru_100_250R. Altogether, these experiments evidence that the dramatic increase in activity of Ru_30_250R (*cf.* Fig. 7 and 8) is traced to H incorporation into the solid solution of rutile $Ru_{0.3}Ti_{0.7}O_2$ and not to the chemical reduction of RuO_2.

HCl oxidation reaction. We test now the Deacon activity of Ru_30 at 250 °C in a net oxidizing reaction mixture (20% HCl and 10% O_2 balanced by 70% Ar, total volume flow: 15 sccm min^{-1}). During temperature ramping the catalyst may suffer from deactivation due to in-depth chlorination which was reported for CeO_2 based catalyst.[37] To cope with this concern, pure Ar is applied during temperature ramping and only if the reaction temperature of 250 °C is reached, the gas feed is switched to $HCl:O_2 = 2:1$.

As seen in Fig. 9 the Ru_30 catalyst is stable with a STY = 3.4 mol per Cl_2 per kg h^{-1}. After this first run we switch to pure Ar for 1 h and then switch to 4% H_2/Ar keeping the catalyst at 250 °C. This *in situ* treatment transforms Ru_30 to Ru_30_250R. Subsequently, the second run starts with the same reaction mixture (20% HCl and 10% O_2). We observe that the STY sharply increases, declines then over 3 h and is finally stabilized at 5.2 mol of Cl_2 per kg catalyst and per h, *i.e.*, substantially higher than for Ru_30 in the first run. After this second run we switch to pure Ar for 1 h and then introduce 20% O_2/Ar to re-oxidize the Ru_30_250R catalyst,

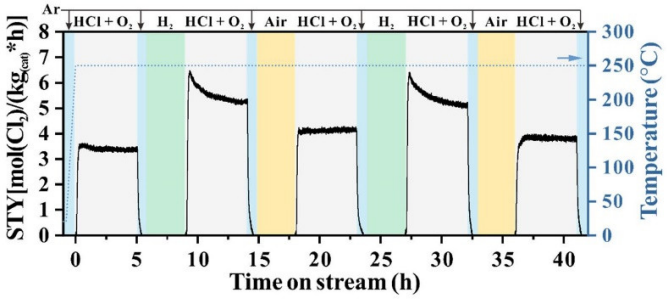

Fig. 9 STY as a function of reaction time on catalytic HCl oxidation over Ru_30. The grey background represents HCl oxidation reaction conditions: 3 sccm HCl, 1.5 sccm O_2, balanced by Ar; total volume flow: 15 sccm min^{-1}, temperature ramp: 5 K min^{-1}. The green background represents the gas mixture during heating and cooling stage: 4% H_2/Ar, total volume flow: 50 sccm min^{-1}. The yellow background represents the gas mixture during the heating and cooling stage: Air (20%O_2/Ar) 50 sccm min^{-1}. The light blue background represents the purging stage under pure argon, 15 sccm min^{-1}.

keeping the catalyst temperature at 250 °C. Subsequently, the third run continues with the HCl oxidation reaction at 250 °C. The steady state value of STY declines to 3.8 mol of Cl_2 per kg catalyst and per h, being slightly higher than in the first run. However, the fourth and fifth run of hydrogen *versus* oxygen treated sample reveal a reversible and stable behavior in the catalytic HCl oxidation reaction in that hydrogen treated samples are significant more active than oxygen treated samples.

With XRD the degree of hydrogen incorporation can be estimated after the catalytic test (*cf.* Fig. S15†). Similar to the case of total oxidation of propane, the degree of H insertion of Ru_30_H_2 is high and halfway between that of Ru_30 and Ru_30_250R.

To check for the contribution of RuO_2/Ru in the HCl oxidation reaction activity over Ru_30, we perform a similar experiment as in Fig. 9 for Ru_100 (*cf.* Fig. S16†). Clearly, Ru_100 is at least one order of magnitude more active than Ru_100_250R, because the latter is reduced to elemental Ru. This experiment implies that the increase in activity of Ru_30_250R is solely caused by hydrogen incorporation into rutile $Ru_{0.3}Ti_{0.7}O_2$.

For comparison reason and to assess the effectiveness of Ru_30 and Ru_30_250R, a benchmark catalyst with similar composition, namely 30 mol% RuO_2/TiO_2-rutile, is prepared by a simple impregnation method and tested under the same reaction conditions as in Fig. 8 and 9 and summarized in Fig. S17.† For propane oxidation, the temperature of 95% conversion for supported 30 mol% RuO_2/TiO_2 is reached at 250 °C, evidencing that the activity is substantially lower than for both Ru_30 (240 °C) and Ru_30_250R samples (200 °C). For HCl oxidation reaction, the STY of 30 mol% RuO_2/TiO_2 at 250 °C is around 5.0 mol of Cl_2 per kg catalyst and per h, a value that is slightly higher than for the Ru_30 sample (4.2 mol of Cl_2 per kg catalyst and per h), while it is slightly lower that that of the hydrogen incorporated Ru_30 catalyst (5.3 mol of CO_2 per kg catalyst and per h).

4. Discussion

4.1 Hydrogen insertion into the mixed $Ru_{0.3}Ti_{0.7}O_2$

A mixed ruthenium–titanium oxide material with nominal 30 mol% Ru (Ru_30) is prepared by a conventional sol–gel method. From XRD this material is shown to consist of two phases, namely of 21 mol% RuO_2 (grain size = 43 ± 5 nm) and 79 mol% of solid solution $Ru_{0.3}Ti_{0.7}O_2$ (grain size = 12 ± 0.5 nm). From EDS–SEM and XPS the bulk and surface composition of Ru_30 are 30 mol% and 29.1 mol% Ru, respectively, and hence close to nominal composition of 30 mol% Ru.

Hydrogen treatment of Ru_30 in 4% H_2/Ar at higher temperatures is able to incorporate hydrogen into the rutile lattice, while this is not possible for pure RuO_2 and pure TiO_2. TG–MS experiments quantify the amount of hydrogen incorporated at 250 °C in the mixed $Ru_{0.3}Ti_{0.7}O_2$ to be 17.6 mol% (*cf.* Fig. 5). If the hydrogenation step of the $Ru_{0.3}Ti_{0.7}O_2$ is performed at 450 °C, only 6.6 mol% H can be incorporated. Obviously, H incorporation is a weakly exothermic process with a reaction enthalpy to be −14 ± 2 kJ mol^{-1}, estimated by assuming that both concentrations are equilibrium concentrations (Van't Hoff equation). H incorporation is an activated process that needs temperatures higher than 150 °C in H_2 atmosphere. Since hydrogen dissociation over ruthenium sites is expected to be non-activated,[38] the observed activation barrier is due likely to diffusion from the adsorbed surface H towards the absorbed state (H insertion). Assuming a typical frequency factor for the diffusion process of 10^{13} s^{-1} and an Arrhenius type equation, a temperature of 150 °C translates to an activation energy of 115 ± 5 kJ mol^{-1}. The estimated energy values are summarized in the black energy diagram of Fig. 10.

Hydrogen treatment leads to changes in the lattice parameters by 1–2% (XRD), but clearly retaining the rutile structure. From a structural point of view (XRD) there is no evidence that the rutile structure of $Ru_{0.3}Ti_{0.7}O_2$ transforms partly into a hydroxide structure.

Next, we elucidate the synergy effect of Ru and Ti in $Ru_{0.3}Ti_{0.7}O_2$ to promote H incorporation. RuO_2 is not stable under H_2 treatment at 250 °C, instead it transforms fully to metallic ruthenium.[20,38] Although Näslund *et al.*[39] reported the hydrogenation of RuO_2 to $RuO(OH)_2$ or $Ru(OH)_3$, these findings were immediately challenged by Karlsson *et al.*[40] Only recently hydrogen insertion into RuO_2 was reported to be accomplished by a dedicated soft chemical approach based on the water gas shift reaction at temperatures below 200 °C.[41] This approach leads to a monoclinic H_xRuO_2 phase upon insertion of hydrogen into the rutile RuO_2 matrix with superior activity in hydrogenation reactions. In our case, no monoclinic structure of $Ru_{0.3}Ti_{0.7}O_2$ is formed.

TiO_2 on the other hand is stable under H_2 exposure at 250 °C for kinetic reasons. The reaction TiO_2 + H_2 → Magneli phase + H_2O requires much higher temperatures (600–1000 °C)[42,43] In the present study, the formation of a Magneli phase upon H_2 treatment at 250 °C can safely be ruled out

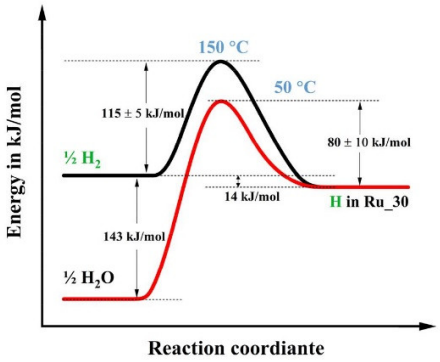

Fig. 10 Energy diagram for the hydrogen incorporation process in Ru_30 catalyst at around 150 °C (black curve) followed by remove under air at around 50 °C (red curve).

based on the presented XRD experiments (*cf.* Fig. 2). At lower temperatures, hydrogen may form deep donors in rutile TiO_2 forming O–H^+ complexes, while in O vacancies hydrogen is stabilized as H^- species; both species occur with low concentrations.[15–19]

One shortcoming of rutile-TiO_2 is the low activity towards molecular H_2 dissociation, requiring an active precious metal. Recently, it was reported that a Pd layer supported on rutile-TiO_2 could accumulate a substantial amount of hydrogen at the interface (within a thickness of 2 nm).[19] In mixed oxide $Ru_{0.3}Ti_{0.7}O_2$ both worlds meet to the advantage. Ru is able to activate molecular hydrogen, while Ti is stabilizing the oxidation state of Ru against further reduction to metallic Ru. This synergistic effect enables $Ru_{0.3}Ti_{0.7}O_2$ to accumulate adsorbed H at the surface first, potentially in the form of surface hydroxides, and in a second step the surface H species is able to penetrate the bulk of $Ru_{0.3}Ti_{0.7}O_2$ maintaining the rutile structure.

So far, we have considered that the H_2 activation takes place on the mixed $Ru_{0.3}Ti_{0.7}O_2$. However, it is also conceivable that metallic ruthenium could activate the H_2 and *via* "spill-over" hydrogen is then transferred to $Ru_{0.3}Ti_{0.7}O_2$. From TEM it is obvious that many mixed oxide particles do not carry any Ru metal particle. Therefore, if only metallic Ru can activate H_2 to dissociate, one would expect a broad distribution of inserted H concentrations that is not reconciled with the XRD experiments in Fig. 2. Therefore, the contribution of metallic Ru particles to dissociate H_2 together with a subsequent spill-over to the mixed oxide is considered to be small if not even negligible.

The next question one can ask is which type of H species is incorporated in the mixed oxide lattice of rutile $Ru_{0.3}Ti_{0.7}O_2$: proton, neutral H, or hydride H^- species. From XPS there is no evidence for a change in oxidation states of Ti^{4+} and Ru^{4+} so that metal cations both remain in the 4+ oxidation state after H insertion. The stable oxidation state of Ru^{4+} and Ti^{4+} excludes substantial formation of O vacancies. In the O1s spectrum (*cf.* Fig. S13†), no additional OH is discernible. This excludes the formation of a mixed oxo-hydroxide as previously proposed by Näslund *et al.*[44] The energy shift of the satellite feature in Ru3d XP spectrum (*cf.* Fig. 6) is reconciled with a reduced valence electron density, when the satellite peak is interpreted in terms of a surface plasmon.[45] This observation is not reconciled with proton incorporation, but instead may point to a kind of hydride species where part of the valence electron density is consumed to form $H^{\delta-}$.

4.2 Stabilization of inserted H in Ru_30_250R

From re-oxidation experiments of Ru_30_250R (*cf.* Fig. 2b) we know that at 50 °C in oxygen atmosphere, hydrogen is largely removed from H-inserted $Ru_{0.3}Ti_{0.7}O_2$ phase, thereby rendering inserted H a labile species. This re-oxidation process is highly exothermic since water is produced (−143 kJ mol^{-1}). Here the diffusion of absorbed H toward surface is again the rate determining step. Assuming a frequency factor of 10^{13} s^{-1} an activation energy of 80 ± 10 kJ mol^{-1} can be estimated based on the Arrhenius equation. The estimated energy values are collected in the red energy diagram of Fig. 10.

Since catalytic oxidation reactions take place typically at higher temperatures than 50–100 °C, we need to find ways to stabilize the inserted hydrogen in $Ru_{0.3}Ti_{0.7}O_2$. In doing so, we develop a two-step strategy: first, since hydrogenation of $Ru_{0.3}Ti_{0.7}O_2$ is very efficient at 250 °C, we apply (*in situ*) the very same hydrogen treatment also in the reactor during ramping the temperature to the desired reaction temperature. In this way, we can reach the reaction temperature without losing hydrogen. Secondly, we choose specific oxidation reactions (HCl and propane oxidation) as test reactions where the catalyst surface is continuously supplied with hydrogen (oxidative dehydrogenation reactions).

4.3 Improved oxidation catalysis of Ru_30_250R in comparison to that of Ru_30

In catalysis research hydrogen treatment of the catalyst is a typical treatment to form the active catalyst. In this process the active component is essentially reduced and considered to be more active than the corresponding oxide phase that is generated during the calcination step of the preparation of the catalyst material. A particularly nice example was previously reported with ruthenium-based catalyst in the ammonia synthesis. Even the optimum Ba-promoted Ru catalyst needs several days on stream and cycling the reaction temperature to accomplish the final activity and therefore the active phase.[46]

In the present study we keep with the oxide phase and insert H into the oxide lattice in order to modulate the catalytic performance. Equally important is that we are able to tune the activity of catalyst *in situ* in the reactor by this simple H_2 treatment at relatively low temperatures.

In the following we discuss the results of two catalytic oxidation reactions, namely the total oxidation of propane and HCl oxidation reaction (Deacon process). These experiments provide compelling evidence that H insertion into rutile $Ru_{0.3}Ti_{0.7}O_2$ promotes oxidation catalysis. It should be noticed that inserted H modulates the catalytic activity without participating directly in the catalytic reactions.

Total oxidation of propane. In the catalytic tests, the propane oxidation reaction is conducted at 170 °C with a reaction mixture of 1% C_3H_8 and 5% O_2 that is balanced by 94% N_2. Ru_30_250R turns out to be significantly more active than Ru_30 (*cf.* Fig. 7a). In pure oxygen, inserted hydrogen is only thermally stable up to 50–100 °C. However, under propane oxidation condition, the hydrogenated catalyst is stable during steady state reaction at 170 °C. Obviously, the hydrogen concentration at the surface produced by H abstraction during catalytic propane decomposition is sufficiently high so that dissolved hydrogen does not experience differences in chemical potential that drives bulk-H towards the surface.

The activity in propane oxidation over Ru_30_250R decreases, however, in the second temperature cycle (*cf.*

Fig. 7a). As the catalyst runs stably in the first cycle at the reaction temperature of 170 °C, we infer that the catalyst Ru_30_250R undergoes deactivation only during temperature ramping. Important for the stability of inserted H is that the surface is continuously supplied by hydrogen from the propane activation. Since propane dissociation is activated, the reaction mixture is at low temperature net oxidizing and only if the temperature is high enough to allow for propane activation (around 100 °C as reflected by an ignition temperature of 100–150 °C (ref. 47 and 48)) the reaction mixture turns into a less oxidizing reaction mixture for the catalyst. Therefore, during the heating and cooling ramp the catalyst is exposed to a reaction mixture that is not able to supply enough hydrogen to the surface (temperature range: 50–100 °C), while the temperature is high enough to loose inserted hydrogen by water formation due to oxygen in the feed. This interplay results in the observed depletion of inserted hydrogen and the observed activity decline.

To overcome this H-depleting scenario, H_2 is deliberately supplied during temperature ramping and only if the reaction temperature is reached, the feed is switched to the reaction mixture propane + O_2. With this "trick" the high concentration of inserted H concentration in $Ru_{0.3}Ti_{0.7}O_2$ can be stabilized and the catalytic oxidation activity for propane keeps high and stable (*cf.* Fig. 7b). As demonstrated in Fig. S14† it is not necessary to start the catalytic tests from Ru_30_250R, but rather the hydrogen insertion step of Ru_30 can be carried out *in situ* in the reactor to achieve high activity in total oxidation of propane.

HCl oxidation reaction (deacon process). The Deacon reaction allows to recover Cl_2 from omnipresent HCl waste produced in chemical industry.[31,49] Sumitomo Chemical developed a RuO_2 based catalyst that is supported on rutile-TiO_2. Currently, this catalyst is the only commercialized one that can cope with the harsh reaction conditions, being sufficiently stable and active.[50]

The Ru_30 catalyst turns out be active and stable under the reaction conditions (T = 250 °C, 20% HCl, 10% O_2, balanced by Ar), *i.e.*, it does not loose activity during time on stream (*cf.* Fig. 9, first cycle). Next, we expose Ru_30 to 4% H_2/Ar for 3 h, thereby transforming *in situ* the catalyst to Ru_30_250R. The advantage of the *in situ* hydrogen treatment is that the catalyst bed, the BET surface area, and other parameters are maintained that are important for the reaction kinetics. This allows for a direct activity comparison of Ru_30 with Ru_30_250R. For the H-treated catalyst, the activity is significantly higher than for Ru_30 and the catalyst runs stably after 3 h on stream (*cf.* Fig. 9, second cycle). Cycling between activation by hydrogen und deactivation by oxygen switches reversibly the catalytic activities between that of Ru_30 and Ru_30_250R. HCl is readily activated on this catalyst by an acid–base reaction[51] so that a sufficient concentration of hydrogen is supplied to the surface under reaction conditions, thereby stabilizing a high concentration of inserted hydrogen. This explains the stable activity of Ru_30_250R after 3 h on stream. We emphasize that *in situ* hydrogenation of Ru_30 needs to be carried out only once prior to the actual Deacon reaction.

4.4 H-Induced activity enhancement

The increased activity can be traced to the modification of the electronic structure of $Ru_{0.3}Ti_{0.7}O_2$ due to H insertion. We can safely assume that inserted hydrogen is not taking place in the catalytic cycle, since we focus here only oxidation reactions in the catalytic tests. Both H insertion itself and the H-induced changes of lattice parameters (*cf.* XRD in Fig. 2) can lead to electronic modifications of $Ru_{0.3}Ti_{0.7}O_2$. The electronic structure is directly affected by H insertion as reconciled with the binding energy shift of the satellite feature in Ru3d. As the satellite feature is assigned to plasmon excitation,[45] the observed shift to lower binding energies can be explained by a reduced valence electron density in $Ru_{0.3}Ti_{0.7}O_2$ due to hydrogen incorporation.

However, H-insertion leads also to strain in the lattice of $Ru_{0.3}Ti_{0.7}O_2$ that can modulate the activity. For instance, the hydrogen-induced compression of the Me–Me bonding of Ru_30_250R along the [001] direction as observed in XRD (*cf.* Table 1) will lead to broader d-band features in the valence band structure that may change the activity.[52–54] Here further *ab initio* studies are required to comprehend on the effect of H insertion in $Ru_{0.3}Ti_{0.7}O_2$ on the catalytic oxidation activity.

It is known that strain can aid to improve the performance of a catalyst such as reported recently for the oxygen evolution reaction (OER) when Li was inserted into RuO_2.[55] Here lithiation maintains the rutile structure of RuO_2, but reveals a slight expansion of the lattice parameters. Similar effects are expected when hydrogen is incorporated in Ru_30 for the OER, especially since the induced strain is substantially larger than for lithiation. Therefore, exposing the mixed oxide catalyst Ru_30 to H_2 may be a viable option to (*in situ*) engineer lattice strain in the catalyst.

In general, a catalyst promotor affects the rate limiting step in a catalytic reaction. For the Deacon reaction, where the final recombination of surface chlorine to form gaseous Cl_2 is considered to the rate determining step,[56,57] we expect that inserted hydrogen will likely reduce the adsorption energy of chlorine. For the case of the total oxidation of propane, both the C–H and the C–C activation are critical steps[58–60] that are promoted by inserted H in Ru_30.

5. Conclusion

We introduce a general and rational synthetic approach to allow for substantial hydrogen incorporation into the lattice by mixing a reducible oxide with a less reducible oxide. This approach is exemplified with the solid solution of RuO_2 and TiO_2. Upon hydrogen exposure at elevated temperatures, RuO_2 is not stable and transforms to metallic Ru, while TiO_2 is not able to incorporate hydrogen into the lattice. A strong synergy effect is established when mixing RuO_2 with a less (or non) reducible rutile-TiO_2. It is shown that the rutile structure of mixed $Ru_{0.3}Ti_{0.7}O_2$ is

stable against H_2 exposure at 250 °C and can readily incorporate 17.6 mol% hydrogen into the rutile lattice, thereby changing slightly the lattice parameters. Inserted hydrogen is likely to be a hydride species since the oxidation state of Ti and Ru in $Ru_{0.3}Ti_{0.7}O_2$ is preserved in the 4+ oxidation state and no additional OH is formed.

For both catalytic oxidation reactions, total oxidation of propane and the HCl oxidation reaction, we demonstrate that the activity is substantially enhanced by H insertion, and the bulk hydrogen concentration is largely preserved under temperature conditions under which hydrogen would have left the oxide bulk, without the catalytic reaction taking place. We anticipate that hydrogen incorporation in mixed oxides may open exciting perspectives as catalysts for the selective hydrogenation of organic compounds. However, hydrogen incorporation in mixed oxides may also be beneficial for electrocatalysis, in particular for the anodic reaction of acidic water electrolysis where strain engineering has already been shown to improve the activity for instance of rutile IrO_2 (ref. 61) or RuO_2.[55]

With bulk incorporation of hydrogen either in a pretreatment or in an *in situ* step, we have an additional handle to control the activity of a mixed oxide catalyst. This approach may be of general interest in catalysis research and inorganic chemistry to fine-tune properties of (mixed) oxides.

Conflicts of interest

The authors declare no conflict of interest.

Acknowledgements

This project was supported financially by National Key Research and Development Program of China (2022YFB3504200), the National Natural Science Foundation of China (U21A20326, 21976057, 21922602 and 21673072) and the Fundamental Research Funds for the Central Universities. Wei Wang gratefully acknowledge the China Scholarship Council for the Joint-Ph.D. program between the China Scholarship Council and the Institute of Physical Chemistry of the Justus-Liebig-University Giessen. We acknowledge support from the Center for Materials Research at the JLU.

References

1 A. Schneemann, J. L. White, S. Y. Kang, S. Jeong, L. F. Wan, E. S. Cho, T. W. Heo, D. Prendergast, J. J. Urban, B. C. Wood, M. D. Allendorf and V. Stavila, *Chem. Rev.*, 2018, **118**, 10775–10839.
2 D. Teschner, J. Borsodi, A. Wootsch, Z. Revay, M. Havecker, A. Knop-Gericke, S. D. Kackson and R. Schlogl, *Science*, 2008, **320**, 86–89.
3 M. Wilde, K. Fukutani, W. Ludwig, B. Brandt, J.-H. Fischer, S. Schauermann and H.-J. Freund, *Angew. Chem., Int. Ed.*, 2008, **47**, 9289–9293.
4 C. Copéret, D. P. Estes, K. Larmier and K. Searles, *Chem. Rev.*, 2016, **116**, 8463–8505.
5 Z. Wu, Y. Cheng, F. Tao, L. Daemen, G. S. Foo, L. Nguyen, X. Zhang, A. Beste and A. J. Ramirez-Cuesta, *J. Am. Chem. Soc.*, 2017, **139**, 9721–9727.
6 K. Werner, X. Weng, F. Calaza, M. Sterrer, T. Kropp, J. Paier, J. Sauer, M. Wilde, K. Fukutani, S. Shaikhutdinov and H.-J. Freund, *J. Am. Chem. Soc.*, 2017, **139**, 17608–17616.
7 T. Cao, R. You, X. Zhang, S. Chen, D. Li, Z. Zhang and W. Huang, *Phys. Chem. Chem. Phys.*, 2018, **20**(14), 9659–9670.
8 H. F. Cheng, M. C. Wen, X. C. Ma, Y. Kuwahara, K. Mori, Y. Dai, B. B. Huang and H. Yamashita, *J. Am. Chem. Soc.*, 2016, **138**, 9316–9324.
9 Z. Li, K. Werner, K. Qian, R. You, A. Płucienik, A. Jia, L. Wu, L. Zhang, H. Pan, H. Kuhlenbeck, S. Shaikhutdinov, W. Huang and H.-J. Freund, *Angew. Chem., Int. Ed.*, 2019, **58**, 14686–14693.
10 G. Vilé, B. Bridier, J. Wichert and J. Pérez-Ramírez, *Angew. Chem., Int. Ed.*, 2012, **51**, 8620–8623.
11 G. Vilé, S. Colussi, F. Krumeich, A. Trovarelli and J. Pérez-Ramírez, *Angew. Chem., Int. Ed.*, 2014, **53**, 12069–12072.
12 J. Carrasco, G. Vilé, D. Fernández-Torre, R. Pérez, J. Perez-Ramírez and M. V. Ganduglia-Pirovano, *J. Phys. Chem. C*, 2014, **118**, 5352–5360.
13 F. Walsh and R. Wills, *Electrochim. Acta*, 2010, **55**, 6342–6351.
14 H. Malik, S. Sarkar, S. Mohanty and K. Carlson, *Sci. Rep.*, 2020, **10**, 8050.
15 Y. Filinchuk, N. A. Tumanov, V. Ban, H. Ji, J. Wei, M. W. Swift, A. H. Nevidomskyy and D. Natelson, *J. Am. Chem. Soc.*, 2014, **136**, 8100–8109.
16 W. R. Palfey, G. R. Rossman and W. A. Goddard III, *J. Phys. Chem. Lett.*, 2021, **12**, 10175–19181.
17 O. W. Johnson, J. Deford and J. W. Shaner, *J. Appl. Phys.*, 1973, **44**, 3008.
18 P. W. Peacock and J. Robertson, *Appl. Phys. Lett.*, 2003, **83**, 2025.
19 M. Sotoudeh, M. D. Bongers-Loth, V. Roddatis, J. Čížek, C. Nowak, M. Wenderoth, P. Blöchl and A. Pundt, *Phys. Rev. Mater.*, 2021, **5**, 125801.
20 Y. B. He, M. Knapp, E. Lundgren and H. Over, *J. Phys. Chem. B*, 2005, **109**, 21825–21830.
21 H. Over, M. Knapp, E. Lundgren, A. P. Seitsonen, M. Schmid and P. Varga, *ChemPhysChem*, 2004, **5**, 167–174.
22 P. P. T. Krause, H. Camuka, T. Leichtweiss and H. Over, *Nanoscale*, 2016, **8**, 13944–13953.
23 C. C. Hu, K. H. Chang, M. C. Lin and Y. T. Wu, *Nano Lett.*, 2006, **6**, 2690–2695.
24 D. R. Rolison, *Science*, 2003, **299**, 1698.
25 K. Yamaguchi, J. W. Kim, J. He and N. Mizuno, *J. Catal.*, 2009, **268**, 343–349.
26 H. Yu, X. Fu, C. Zhou, F. Peng, H. Wang and J. Yang, *Chem. Commun.*, 2009, 2408–2410.
27 V. V. Costa, M. J. Jacinto, L. M. Rossi, R. Landers and E. V. Gusevskaya, *J. Catal.*, 2011, **282**, 209–214.
28 D. R. Rolison, P. L. Hagans, K. E. Swider and J. W. Long, *Langmuir*, 1999, **15**, 774–779.
29 S. Trasatti, *Electrochim. Acta*, 2000, **45**, 2377–2385.

30 H. Hao, Z. W. Liu, F. Q. Zhao and W. Q. Li, *Renewable Sustainable Energy Rev.*, 2016, **62**, 521–533.
31 J. Pérez-Ramírez, C. Mondelli, T. Schmidt, O. F.-K. Schlüter, A. Wolf, L. Mleczko and T. Dreier, *Energy Environ. Sci.*, 2011, **4**, 4786–4799.
32 O. Khalid, A. S. Luciano, G. Drazic and H. Over, *ChemCatChem*, 2021, **13**, 3983–3994.
33 C. Kanzler, S. Urban, K. Zalewska-Wierzbicka, F. Hess, S. F. Rohrlack, C. Wessel, R. Ostermann, J. P. Hofmann, B. M. Smarsly and H. Over, *ChemCatChem*, 2013, **5**, 2621–2626.
34 M. T. Colomer and J. R. Jurado, *Chem. Mater.*, 2000, **12**(4), 923–930.
35 X. Wang, Y. Shao, X. Liu, D. Tang, B. Wu, Z. Tang, X. Wang and W. Lin, *J. Am. Ceram. Soc.*, 2015, **98**, 1915–1924.
36 A. R. Denton and N. W. Ashcroft, *Phys. Rev. A: At., Mol., Opt. Phys.*, 1991, **43**, 3161–3164.
37 A. P. Amrute, C. Mondelli, M. Moser, G. Novell-Leruth, N. López, D. Rosenthal, R. Farra, M. E. Schuster, D. Teschner, T. Schmidt and J. Pérez-Ramírez, *J. Catal.*, 2012, **286**, 287–297.
38 M. Knapp, D. Crihan, A. P. Seitsonen, E. Lundgren, A. Resta, J. N. Andersen and H. Over, *J. Phys. Chem. C*, 2007, **111**, 5363–5373.
39 L.-Å. Näslund, Á. S. Ingason, S. Holmin and J. F. Rosen, *J. Phys. Chem. C*, 2014, **118**, 15315–15323.
40 R. K. B. Karlsson, A. Cornell and L. G. M. Petterson, *J. Phys. Chem. C*, 2016, **120**, 7094–7102.
41 H. J. Yang, M. Redington, D. P. Miller, E. Zurek, M. Kim, C.-S. Yoo, S. Y. Lim, H. Cheong, S.-A. Chae, D. Ahn and N. H. Hur, *Catal. Sci. Technol.*, 2022, **12**, 6556.
42 F. Walsh and R. Wills, *Electrochim. Acta*, 2010, **55**, 6342–6351.
43 H. Malik, S. Sarkar, S. Mohanty and K. Carlson, *Sci. Rep.*, 2020, **10**, 8050.
44 L.-Å. Näslund, C. M. Sánchez-Sánchez, Á. S. Ingason, J. Bäckström, E. Herrero, J. Rosen and S. Holmin, *J. Phys. Chem. C*, 2013, **117**, 6126–6135.
45 H. Over, A. P. Seitsonen, E. Lundgren, M. Smedh and J. N. Andersen, *Surf. Sci.*, 2002, **504**, L196–L200.
46 H. Bielawa, O. Hinrichsen, A. Birkner and M. Muhler, *Angew. Chem., Int. Ed.*, 2001, **40**, 1061–1063.
47 Z. Wang, Z. Huang, J. T. Brosnahan, S. Zhang, Y. Guo, Y. Guo, L. Wang, Y. Wang and W. Zhan, *Environ. Sci. Technol.*, 2019, **53**(9), 5349–5358.
48 J. Wu, B. Chen, J. Yan, X. Zheng, X. Wang, W. Deng and Q. Dai, *Chem. Eng. J.*, 2022, **438**, 135501.
49 M. W. M. Hisham and S. W. Benson, *J. Phys. Chem.*, 1995, **99**, 6194–6198.
50 K. Seki, *Catal. Surv. Asia*, 2010, **14**, 168–175.
51 M. Capdevila-Cortada, G. Vilé, D. Teschner, J. Pérez-Ramírez and N. López, *Appl. Catal., B*, 2016, **197**, 299–312.
52 B. Hammer and J. Nørskov, *Surf. Sci.*, 1995, **343**, 211–220.
53 J. R. Kitchin, J. K. Nørskov, M. A. Barteau and J. G. Chen, *Phys. Rev. Lett.*, 2004, **93**, 156801.
54 J. K. Nørskov, F. Abild-Pedersen, F. Studt and T. Bligaard, *Proc. Natl. Acad. Sci. U. S. A.*, 2011, **108**, 937–943.
55 Y. Qin, T. Yu, S. Deng, X. Y. Zhou, D. Lin, Q. Zhang, Z. Jin, D. Zheng, Y. B. He, H. J. Qiu, L. He, F. Kang, K. Li and T. Y. Zhang, *Nat. Commun.*, 2022, **13**, 3784.
56 N. López, J. Gòmez-Segura, R. Marìn and J. Pérez-Ramírez, *J. Catal.*, 2008, **255**, 29–39.
57 S. Zweidinger, D. Crihan, M. Knapp, J. Hofmann, A. Seitsonen, C. Weststrate, E. Lundgren, J. Andersen and H. Over, *J. Phys. Chem. C*, 2008, **112**, 9966–9969.
58 T. F. Garetto, E. Rincón and C. R. Apestegua, *Appl. Catal., B*, 2004, **48**, 167–174.
59 C. G. Freyschlag and R. J. Madix, *Mater. Today*, 2011, **14**, 134–142.
60 L. Ma, Y. Geng, X. Y. Chen, N. Q. Yan, J. H. Li and J. W. Schwank, *Chem. Eng. J.*, 2020, **402**, 125911.
61 G. Buvat, M. J. Eslamibidgoli, A. H. Youssef, S. Garbarino, A. Ruediger, M. Eikerling and D. Guay, *ACS Catal.*, 2020, **10**, 806–817.

3. Conclusion and Outlook

The present Ph.D. thesis presents the fundamental research on the rutile-phase ruthenium-titanium mixed oxides with varying compositions, aiming to explore the potential for hydrogen incorporation into the lattice and its effect on thermal catalysis such as propane oxidation and HCl oxidation reactions. Initially, we prepare the mixed ruthenium-titanium oxide material with varying concentration *x* of Ru (Ru_x) by a conventional sol-gel method. Thereafter, the Ru_x catalysts undergo pretreatment under hydrogen at 250 °C, after which their activity and stability are evaluated in propane oxidation reaction. Furthermore, Ru_30 sample is chosen to investigate the structural changes by hydrogen exposure at elevated temperatures. In order to understand the promotional effect of hydrogen insertion during the catalytic process, dedicated in-situ hydrogen/air treatment experiments are conducted during propane oxidation and HCl oxidation tests. The main conclusions are as follows.

$Ru_xTi_{1-x}O_2$ catalysts prepared by classic sol-gel method reveals a clear miscibility gap in a wide composition range. Ru_x consists of pure RuO_2 and a well-mixed $Ru_xTi_{1-x}O_2$ when *x* is below 70%, while additional metallic Ru is formed for higher concentrations of Ru. The specific surface area increases with an increase in the concentration of Ti. The Ru 3d satellite features in XPS monotonically shift to lower binding energies with lower Ru concentration, pointing to a reduced valence electron density. Based on extensive characterizations, the rutile structure as well as the oxidation states of Ru^{4+} and Ti^{4+} can be preserved after hydrogen exposure at 250 °C, while a certain amount of hydrogen can be incorporated into the lattice. Base on the XPS data, we infer that the inserted hydrogen is a hydride species ($H^{-\delta}$), which can be readily removed by increasing the temperature in the ambient atmosphere. Propane oxidation activity data indicates that H insertion is beneficial for the oxidation catalysis of propane, with the optimum catalyst being identified with Ru_60_250R. The inserted hydrogen does not take place in the catalytic cycle, and an altered electronic structure induced by hydrogen may be the reason for the increased activity.

The Ru_30 sample is chosen for further studies, since the specific concentration of Ru of 30 mol% is comparable with the Ru concentration of dimensionally stable anodes (DSA) employed in the large-scale industrial process of chlorine evolution reaction. As derived from the characterization by XRD and XPS, Ru_30 is not phase pure but consists of 21 mol% RuO_2 and 79 mol% $Ru_{0.3}Ti_{0.7}O_2$ solid solution. The $Ru_{0.3}Ti_{0.7}O_2$ solid solution phase can successfully incorporate 17.6 mol% hydrogen into the rutile lattice after hydrogen treatment in 4% H_2/Ar.

Quite in contrast, pure RuO_2 is not able to incorporate hydrogen under hydrogen exposure of but transforms into metallic Ru, while rutile TiO_2 is kinetically stable and does not allow for hydrogen absorption at 250 °C. Therefore, according to our study, mixing Ru with a non or less reducible oxide like Ti could be a general approach to incorporate hydrogen into the RuO_2-based materials. The activity data in both propane oxidation and HCl oxidation reaction demonstrate that for hydrogen-incorporated $Ru_{0.3}Ti_{0.7}O_2$ the catalytic performance in oxidation catalysis is improved substantially. Hydrogen-induced lattice strain in $Ru_{0.3}Ti_{0.7}O_2$ accompanied by altered electronic properties is likely to be the reason for the observed enhanced catalytic activity. The stabilization of hydrogen in the rutile lattice during oxidation reactions could be achieved by the following two-step strategy: First, since hydrogenation of $Ru_{0.3}Ti_{0.7}O_2$ is very efficient at 250 °C, we apply (in situ) the very same hydrogen treatment also in the reactor during ramping the temperature up to the desired reaction temperature. In this way, we can reach the reaction temperature without losing hydrogen. Secondly, we choose specific oxidation reactions (HCl and propane oxidation) as test reactions where the catalyst surface is continuously supplied with hydrogen. Therefore, dissolved hydrogen does not experience a driving force to diffuse towards the surface, thus stabilizing the inserted hydrogen in the lattice of the mixed oxide.

According to the above-mentioned investigations of hydrogen-incorporated $Ru_xTi_{1-x}O_2$ catalysts, some interesting issues may be studied in the future:

1. Strain engineering has been considered a promising way to tune the catalytic activity. In the present study, hydrogen treatment at 250 °C can induce substantial lattice strain in Ru-Ti mixed oxide systems which strongly enhances the catalytic activity, while the mild re-oxidation treatment can recover most of the strain, leading to the activity decrease in both propane and HCl oxidation reactions. However, a direct correlation of strain with activity is not evident for Ru_x_250R and needs further studies. In doing so, a simpler catalyst model needs to be established with less variant parameters but only the lattice stain. The sol-gel method applied in the present study does not produce single-phase Ru-Ti mixed oxides, hence the synthesis method needs to be further optimized.

2. In the current study, the inserted hydrogen is considered to be a hydride species by excluding the existence of proton and elemental hydrogen species. However, the exact state of hydrogen needs to be clarified by state-of-the-art characterization methods such as Neutron powder diffraction (NPD) and infrared reflection absorption spectroscopy (IRAS).

3. The present study shows the promotional effect of hydrogen in oxidation catalysis, but it is also meaningful to explore its potential application in catalytic hydrogenation reaction or water splitting reactions like OER and HER. In the former case, the inserted hydrogen can directly participate into the reaction as the active component, while in the latter case the reaction temperature is less intensive (laboratory electrochemical testing is normally conducted at room temperature, while industrial electrolyzers are run at temperatures around 80 °C for both acidic and alkaline conditions.), so that the incorporated hydrogen could be safely preserved in the lattice without continuous supply. In fact, the hydrogenated Ru_30 and Ir_30 catalysts are currently being tested and studied in OER in our group.

4. Appendix

4.1 Supporting Information of Publication 1

Supporting Information

Hydrogen Incorporation in $Ru_xTi_{1-x}O_2$ Mixed Oxides Promotes Total Oxidation of Propane

Wei Wang,[1,2] Yu Wang,[1,2] Phillip Timmer,[2] Alexander Spriewald-Luciano,[2] Tim Weber,[2] Lorena Glatthaar,[2] Yun Guo,[1] Bernd M. Smarsly,[2]* Herbert Over[2]**

1) Key Laboratory for Advanced Materials, Research Institute of Industrial Catalysis, School of Chemistry and Molecular Engineering, East China University of Science and Technology, Shanghai 200237, China
2) Institute of Physical Chemistry, Justus Liebig University, Heinrich-Buff-Ring 17, D-35392 Giessen, Germany

* Correspondence: Herbert.Over@phys.chemie.uni-giessen.de; Bernd.Smarsly@phys.Chemie.uni-giessen.de; yunguo@ecust.edu.cn

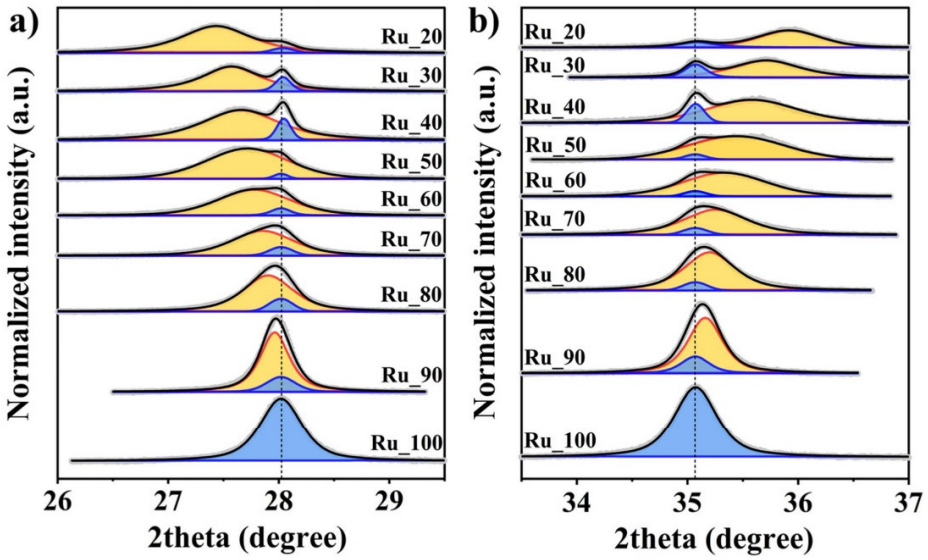

Figure S1: Decomposition of the (110) (a) and the (101) (b) reflection of Ru_x as a function of composition *x* in order to extract lattice parameters of the mixed phase.

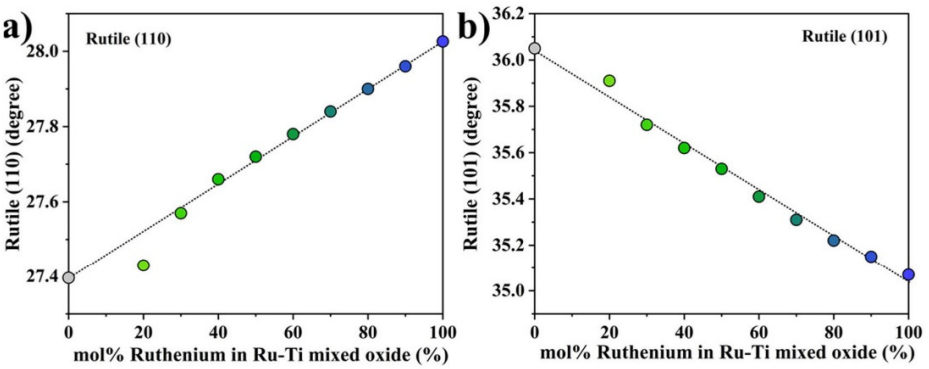

Figure S2: Peak shift of rutile (a) (110) and (b) (101) reflections in the mixed $Ru_xTi_{1-x}O_2$ oxide phase as a function of the nominal composition *x*.

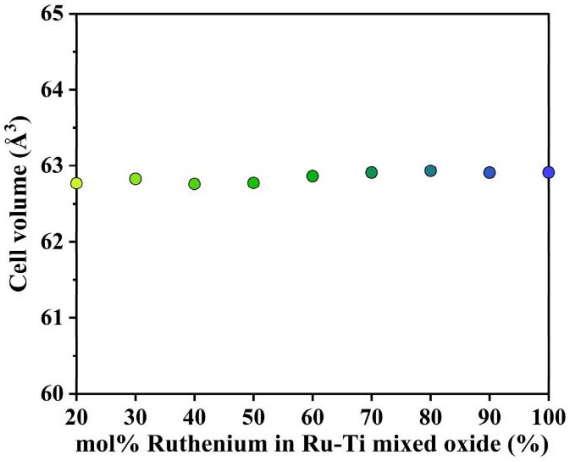

Figure S3: Calculated cell volumes of Ru_x as a function of composition *x* based on the unit cell parameters *a/b* and *c* of the mixed oxide $Ru_xTi_{1-x}O_2$ phase.

Table S1: Calculation of grain size and microstrain of Ru-Ti mixed oxides catalysts by Williamson-Hall method.

Catalysts	Grain size (RuO_2) (nm)[a]	Microstrain (RuO_2)[a]	Grain size (Ru-Ti) (nm)[b]	Microstrain (Ru-Ti)[b]
Ru_100	25.87	0.0020	-	-
Ru_90	29.17	0.0020	50.78	0.0020
Ru_80	36.08	0.0020	19.87	0.0004
Ru_70	54.85	0.0020	14.14	0.0006
Ru_60	72.16	0.0020	9.79	0.0008
Ru_50	137.11	0.0006	7.21	0.0002
Ru_40	114.26	0.0020	9.79	0.0040
Ru_30	72.16	0.0005	12.46	0.0020
Ru_20	69.15	0.0004	11.56	0.0002

a: Determined by Williamson-Hall method from the (110), (101), (020) and (111) reflections of RuO_2 phase.
b: Determined by Williamson-Hall method from the of (110), (101), (020) and (111) reflections of Ru-Ti mixed oxide phase.

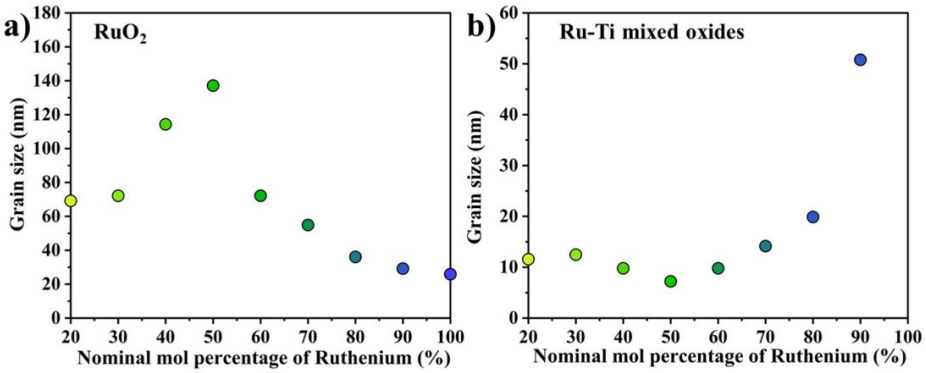

Figure S4: Calculated crystallite size of (a) RuO_2 phase and (b) Ru-Ti solid solution phase as a function of the nominal composition x given in mol% as determined by Williamson-Hall method.

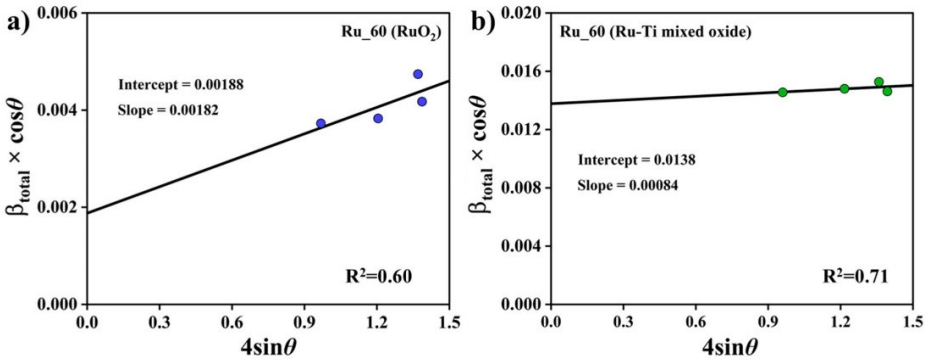

Figure S5: Williamson-Hall plot of (a) RuO_2 phase and (b) Ru-Ti solid solution phase as exemplified by Ru_60 sample.

Table S2: Optimized fitting parameters for the deconvolution of Ru 3d, Ru 3p, Ti 2p and O 1s photoelectron spectra used in our study.

	Ru3d-5/2		Ru3d-5/2 sat		Ru3d-3/2		Ru3d-3/2 sat		Ru3d-5/2 metal		Ru3d-3/2 metal	
Line shape	LF (0.4, 1, 45, 280)		LF (0.4, 1, 45, 280)		LF (0.6, 1, 45, 280)		LF (0.6, 1, 45, 280)		LF (1.2, 1, 400; 280)		LF (1.01, 1.25, 500, 50)	
Cat.	BE (eV)	FWHM	BE (eV)	FWHM	BE (eV)	BE (eV)	FWHM	BE (eV)	FWHM	BE (eV)	BE (eV)	FWHM
Ru_100	280.72	0.71	282.69	1.81	284.89	1.32	286.86	2.43	-	-	-	-
Ru_90	280.74	0.70	282.62	1.81	284.91	1.39	286.79	2.53	-	-	-	-
Ru_80	280.77	0.71	282.56	2.08	284.93	1.24	286.73	2.51	-	-	-	-
Ru_70	280.69	0.72	282.50	2.07	284.86	1.43	286.67	2.33	-	-	-	-
Ru_60	280.72	0.78	282.46	2.03	284.89	1.36	286.63	2.48	-	-	-	-
Ru_50	280.69	0.76	282.42	2.12	284.86	1.31	286.59	2.49	-	-	-	-
Ru_40	280.84	0.79	282.38	1.88	285.01	1.29	286.64	2.29	-	-	-	-
Ru_30	280.84	0.82	282.34	1.89	285.00	1.30	286.51	2.26	-	-	-	-
Ru_20	280.90	0.93	282.31	1.86	285.12	1.47	286.48	2.30	-	-	-	-
Ru_60_250R	280.83	0.85	281.59	1.89	285.00	1.22	285.75	2.10	280.25	0.58	284.42	0.95
Ru_60_250R_300O	280.80	0.74	282.43	2.05	284.97	1.29	286.60	2.1	280.28	0.68	284.45	0.95

	Ru3p-3/2		Ru3p-3/2 sat		Ru3p-1/2		Ru3p-1/2 sat		Ti2p-3/2		Ti2p-3/2	
Line shape	LF(1, 1, 45, 280)		LF(1, 1, 45, 280)		LF(1, 1, 45, 280)		LF(1, 1, 45, 280)		GL(30)		GL(30)	
Cat.	BE (eV)	FWHM	BE (eV)	FWHM	BE (eV)	FWHM	BE (eV)	FWHM	BE (eV)	FWHM	BE (eV)	FWHM
Ru_100	462.51	3.11	465.26	4.34	484.91	3.2	487.60	5.07	-	-	-	-
Ru_90	462.32	2.88	465.15	4.0	484.72	3.10	487.50	4.30	458.32	1.65	464.02	2.0
Ru_80	462.36	3.11	464.99	3.64	484.76	3.30	487.39	3.80	458.35	1.56	464.05	2.25
Ru_70	462.21	3.00	464.86	4.10	484.61	3.26	487.26	4.30	458.26	1.62	463.96	2.20
Ru_60	462.19	2.85	464.75	3.90	484.59	3.33	487.15	4.42	458.27	1.61	463.97	2.16
Ru_50	462.20	3.10	464.70	4.00	484.60	3.24	487.10	4.20	458.25	1.52	463.95	2.22
Ru_40	462.20	2.97	464.60	3.61	484.61	3.23	487.06	4.00	458.59	1.53	464.29	2.31
Ru_30	462.18	3.00	464.46	3.81	484.58	3.20	487.00	4.08	458.53	1.45	464.23	2.23
Ru_20	462.19	3.08	464.41	3.90	484.69	3.50	486.81	4.08	458.33	1.37	464.03	2.20
Ru_60_250R	461.73	2.90	463.76	4.10	484.13	2.90	486.16	4.15	458.27	1.33	463.97	2.29
Ru_60_250R_300O	462.09	3.09	464.56	4.11	484.49	3.10	486.96	4.11	458.27	1.41	463.97	2.17

	O-1s		OH/Oxygenated carbon	
Line shape	LF(0.37,1.2,25,110)		GL(30)	
Cat.	BE (eV)	FWHM	BE (eV)	FWHM
Ru_100	529.21	1.01	531.98	2.90
Ru_90	529.28	1.0	531.84	2.40
Ru_80	529.34	1.02	531.90	1.40
Ru_70	529.26	1.05	531.55	1.30
Ru_60	529.28	1.06	531.83	1.28
Ru_50	529.25	1.03	531.91	1.17
Ru_40	529.56	1.06	531.99	1.04
Ru_30	529.54	1.04	531.91	0.80
Ru_20	529.39	0.98	531.87	0.96
Ru_60_250R	529.56	1.06	531.87	1.19
Ru_60_250R_300O	529.37	0.99	531.78	1.39

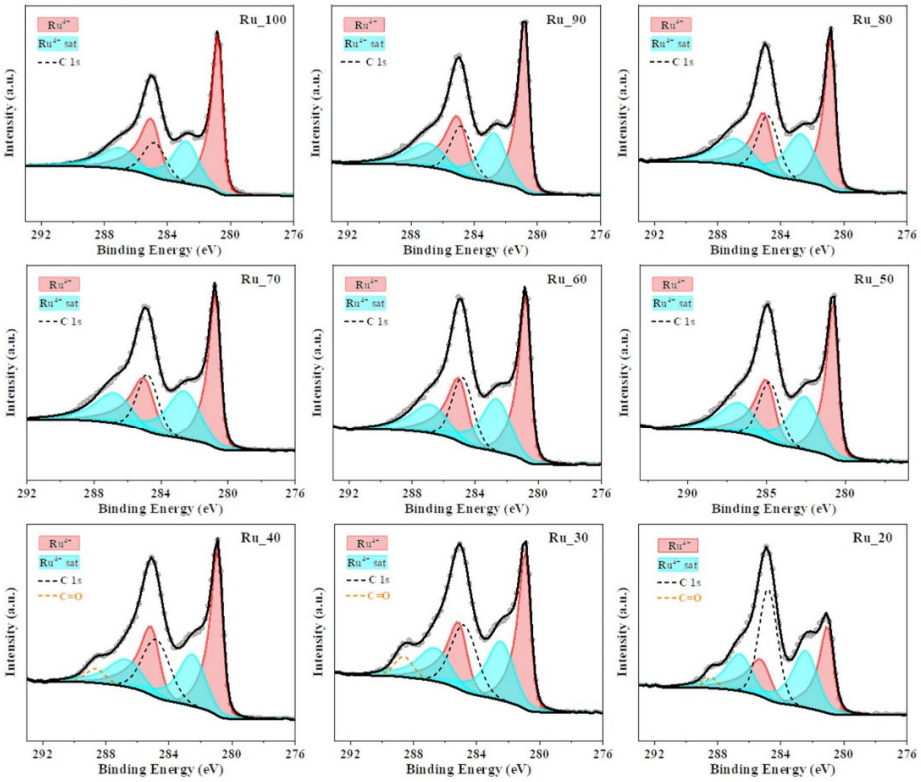

Figure S6: Deconvolution of Ru 3d XP spectra of freshly prepared Ru_x catalysts.

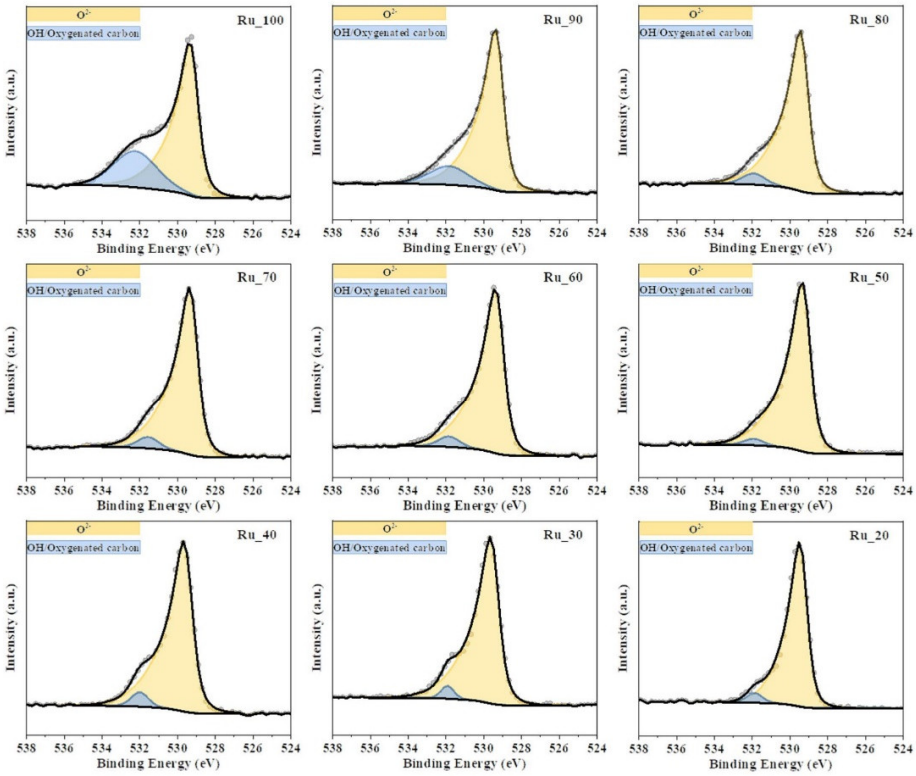

Figure S7: Deconvolution of O 1s spectra of freshly prepared Ru_x catalysts with varying composition *x*.

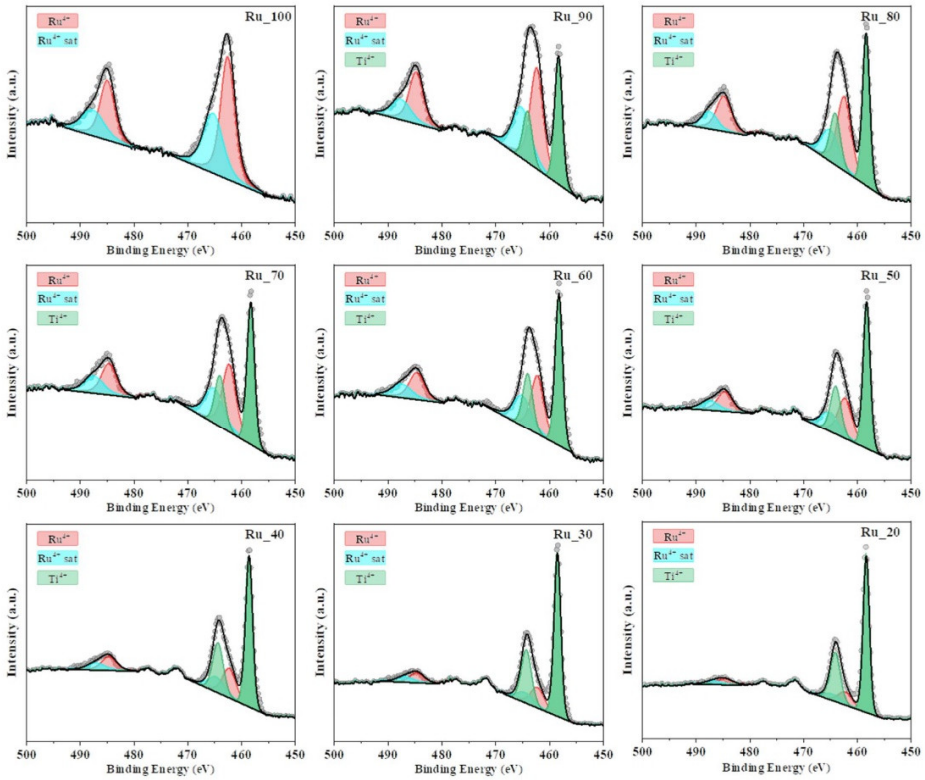

Figure S8: Deconvolution of Ru3p and Ti2p spectra of Ru_x catalysts with varying composition *x*.

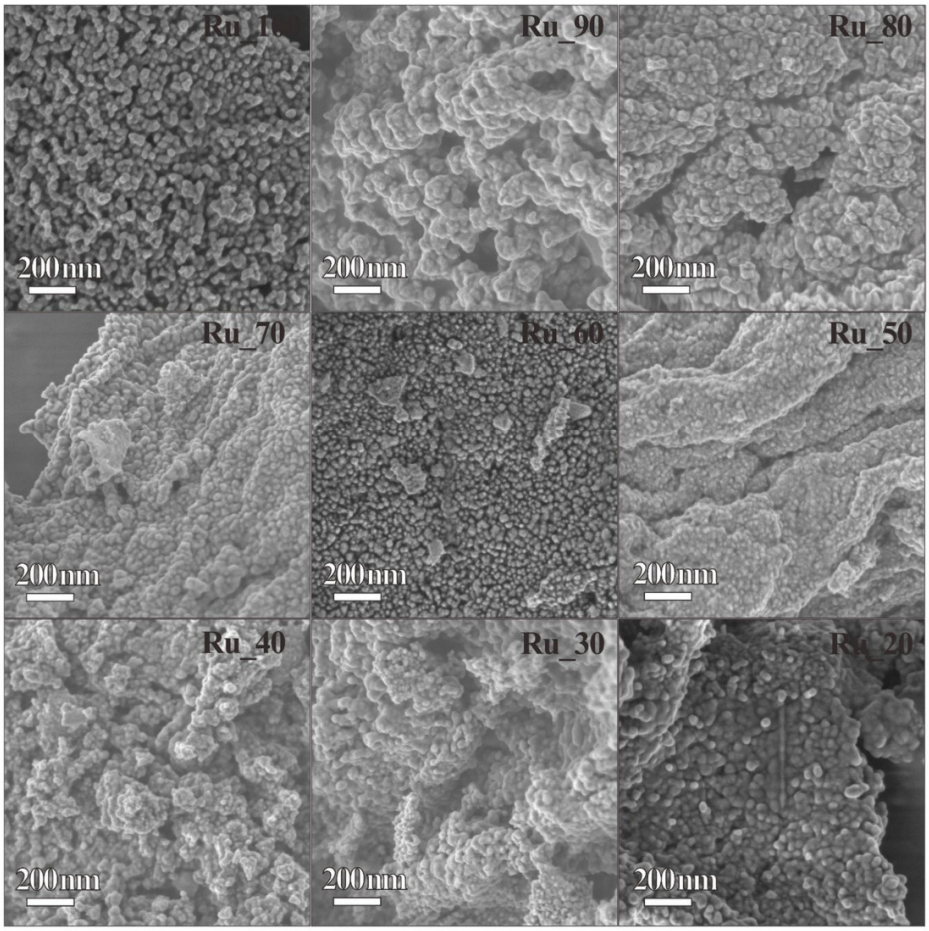

Figure S9: SEM micrographs for the various Ru_x samples.

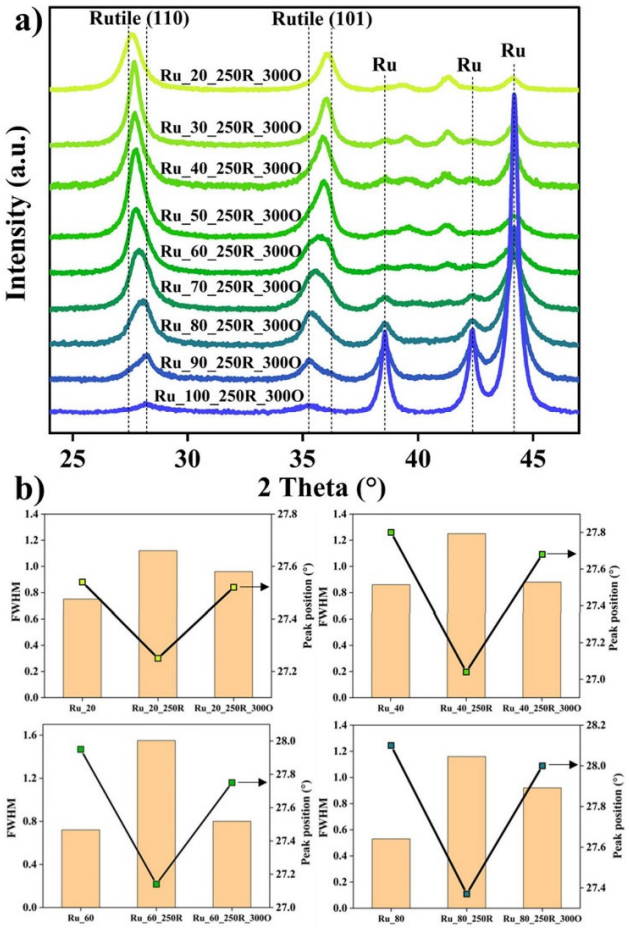

Figure S10: (a) XRD patterns of Ru_x_250R samples re-oxidized at 300 °C. (b) The changes of macrostrain (position) and microstrain (FWHM) of rutile (110) reflections of the Ru-Ti mixed oxide phase among the initial, reduced and re-oxidized Ru_x samples.

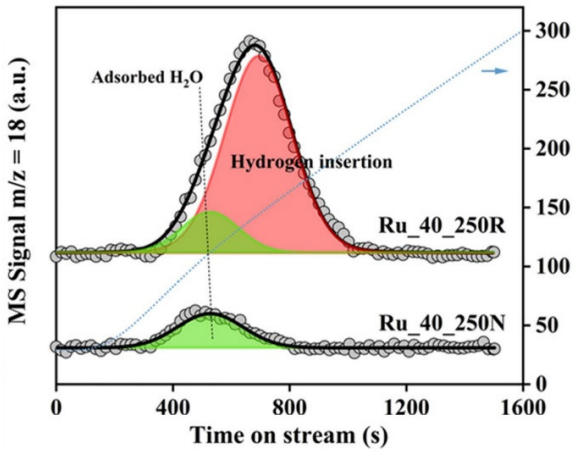

Figure S11: Peak deconvolution of H_2O signal (m/z = 18) of the Ru_40_250R and Ru_40_250N.

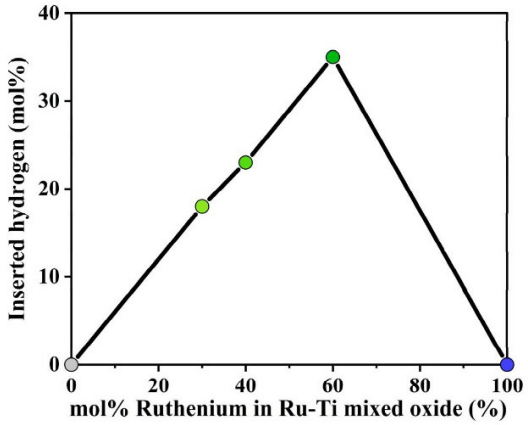

Figure S12: The calculated amount of incorporated hydrogen when varying the composition *x* of Ru_x.

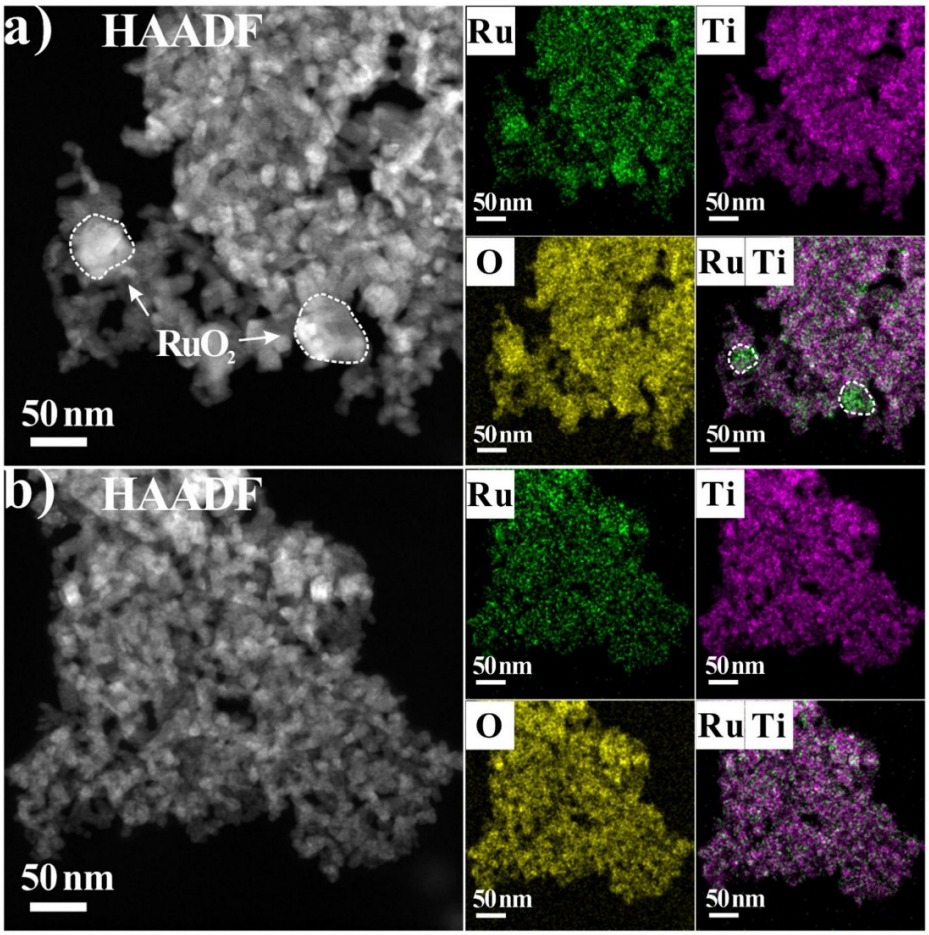

Figure S13: HAADF-STEM images and element mapping of (a) Ru_60 and (b) Ru_60_250R.

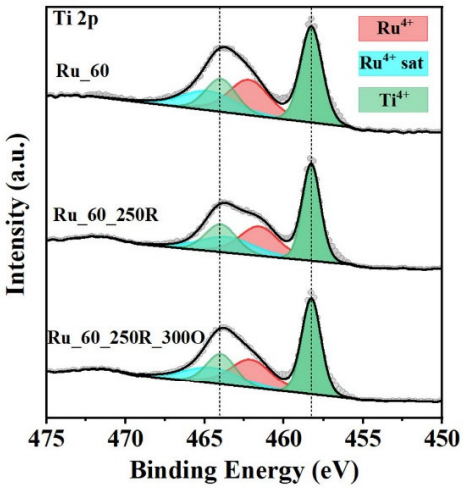

Figure S14: XPS-Ti 2p XP spectra of Ru_60, Ru_60_250R and Ru_60_250R_300O.

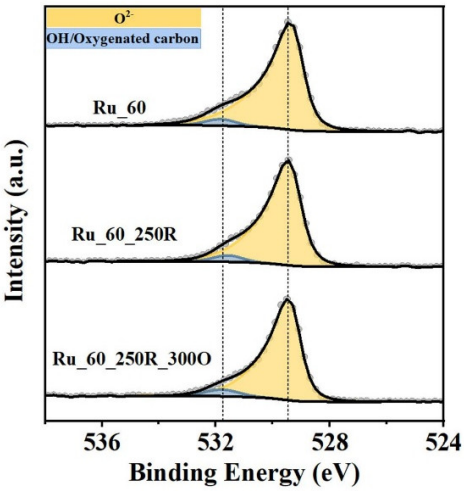

Figure S15: XPS-O 1s XP spectra of Ru_60, Ru_60_250R and Ru_60_250R_300O.

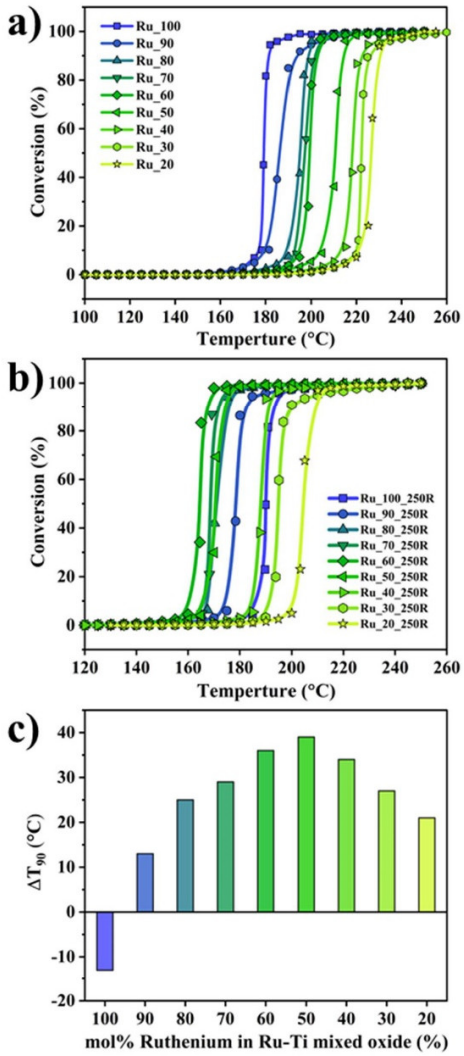

Figure S16: Light-off curves of catalytic propane combustion (1% propane, 5% O_2 balanced by 94% N_2) over Ru_x (b) and Ru_x_250R (b) (x ranging from 20% to 100% in steps of 10%) as a function of reaction temperature, when cycling the reaction temperature from 30 °C to 250 °C. The difference in T_{90}, i.e. the temperature, where 90 % conversion is reached, for Ru_x and Ru_x_250R is shown in panel c).

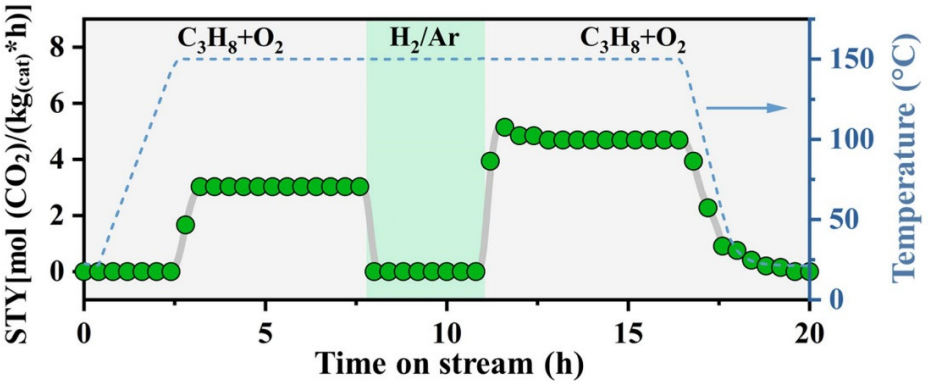

Figure S17. STY as a function of reaction time on catalytic propane oxidation over Ru_60_400R when keeping the reaction temperature at 150 °C (blue dotted line). The grey background represents total C_3H_8 oxidation conditions: 1 vol% C_3H_8, 5 vol% O_2, balanced by N_2; total volume flow: 100 sccm/min, temperature ramp: 1 K/min. The green background represents the gas mixture during heating and cooling stage: 4% H_2/Ar, total volume flow: 50 sccm/min. When reaching 150 °C, the gas composition is switched to the reaction mixture (grey background).

4.2 Supporting Information of Publication 2

Electronic Supplementary Material (ESI) for Catalysis Science & Technology.

Supporting Information

Inserted Hydrogen Promotes Oxidation Catalysis of Mixed $Ru_{0.3}Ti_{0.7}O_2$ as Exemplified with Total Propane Oxidation and HCl Oxidation Reaction

Wei Wang,[a,b] Phillip Timmer,[b] Alexander Spriewald Luciano,[b] Yu Wang,[a,b] Tim Weber,[b] Lorena Glatthaar,[b] Yun Guo,[a]* Bernd M. Smarsly,[b]* Herbert Over [b]*

a) Key Laboratory for Advanced Materials, Research Institute of Industrial Catalysis, School of Chemistry and Molecular Engineering, East China University of Science and Technology, Shanghai 200237, PR China
b) Institute of Physical Chemistry, Justus Liebig University, Heinrich-Buff-Ring 17, D-35392 Giessen, Germany

*Corresponding author: email Herbert.Over@phys.chemie.uni-giessen.de; Bernd.Smarsly@phys.Chemie.uni-giessen.de; yunguo@ecust.edu.cn

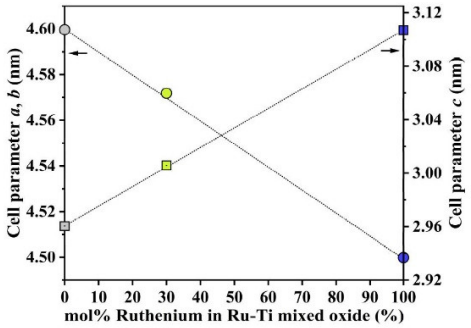

Figure S1: Lattice parameters of rutile TiO_2, RuO_2 and $Ru_xTi_{1-x}O_2$ of Ru_30, as derived from the peak deconvolution of rutile (110) and rutile (101). Assuming the validity of Vegard's rule, the composition *x* of $Ru_xTi_{1-x}O_2$ in Ru_30 is determined to be x=30 ± 3%.

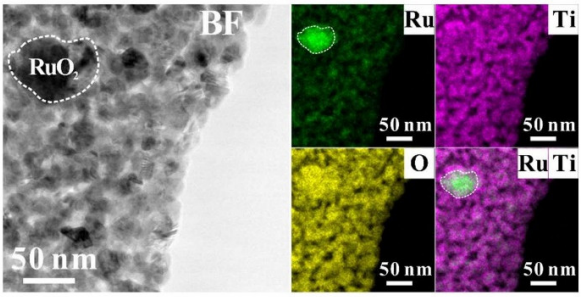

Figure S2: High resolution bright field (BF) images of Ru_30. EDS mapping images are also presented on the right: green = Ru; magenta = Ti; yellow = O, indicating the presence of big RuO_2 particles supported on an otherwise mixed $Ru_xTi_{1-x}O_2$; x = 26 ± 4 mol%.

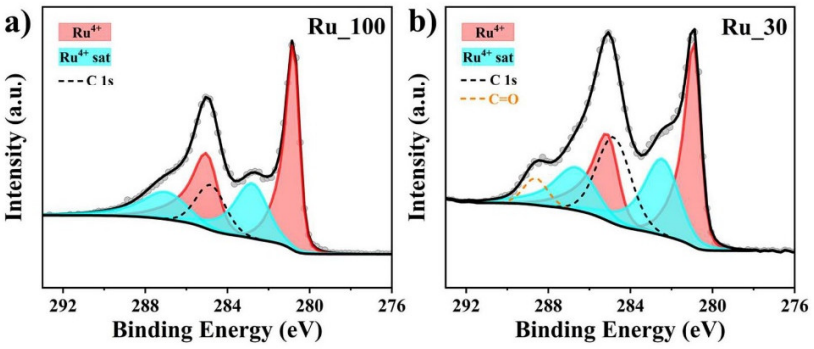

Figure S3: Deconvolution of Ru 3d XP spectra of freshly prepared Ru_100 and Ru_30.

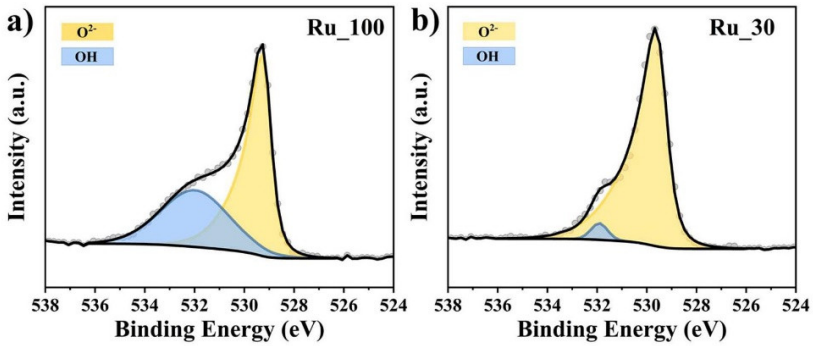

Figure S4: Deconvolution of O 1s spectra of freshly prepared Ru_100 and Ru_30.

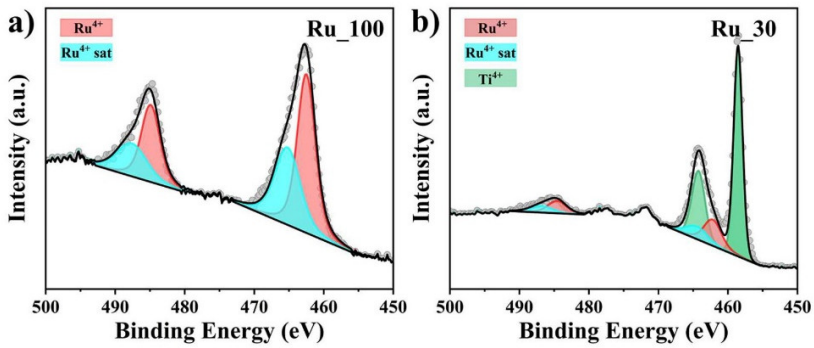

Figure S5: Deconvolution of Ru 3p and Ti 2p XP spectra of Ru_100 and Ru_30.

Table S1: Optimized fitting parameters for the deconvolution of Ru 3d, Ru 3p, Ti 2p and O 1s of used in our study.

	Ru_100	Ru_30	Ru_30_250R	Ru_30_250R_300O
BE (eV) Ru3d-5/2	280.7	280.8	280.8	281.0
FWHM	0.71	0.82	0.85	0.85
Line shape	LF (0.4, 1, 45, 280)			
BE (eV) Ru3d-3/2	284.9	285.0	284.9	285.2
FWHM	1.32	1.30	1.12	1.31
Line shape	LF (0.4, 1, 45, 280)			
BE (eV) Ru3d-5/2 sat	282.7	282.3	281.6	282.5
FWHM	1.81	1.89	1.51	1.88
Line shape	LF (0.6, 1, 45, 280)			
BE (eV) Ru3d-3/2 sat	286.9	286.5	285.8	286.7
FWHM	2.43	2.26	2.34	2.28
Line shape	LF (0.6, 1, 45, 280)			
BE (eV) Ru3d-5/2 metal	-	-	280.2	280.3
FWHM	-	-	0.60	0.71
Line shape	LF (1.2, 1, 400; 280)			
BE (eV) Ru3d-3/2 metal	-	-	284.4	284.5

FWHM	-	-	0.80	0.89
Line shape		LF (1.01, 1.25, 500, 50)		

	Ru_100	Ru_30
BE (eV) Ru3p-3/2	462.5	462.2
FWHM	3.11	3.00
Line shape	LF(1, 1, 45, 280)	
BE (eV) Ru3p-1/2	484.9	484.5
FWHM	3.2	3.00
Line shape	LF(1, 1, 45, 280)	
BE (eV) Ru3p-3/2 sat	465.3	464.5
FWHM	4.34	3.81
Line shape	LF(1, 1, 45, 280)	
BE (eV) Ru3p-1/2 sat	487.6	486.9
FWHM	5.07	4.08
Line shape	LF(1, 1, 45, 280)	
BE (eV) Ti2p-3/2	-	458.5
FWHM	-	1.46
Line shape	GL(30)	
BE (eV) Ti2p-1/2	-	464.2
FWHM	-	2.24
Line shape	GL(30)	

	Ru_100	Ru_30
BE (eV) O-1s	529.2	529.5
FWHM	0.86	1.07
Line shape	LF(0.37, 1.2, 25, 110)	
BE (eV) O-1s sat	532.0	531.9
FWHM	3.22	0.80
Line shape	GL(30)	

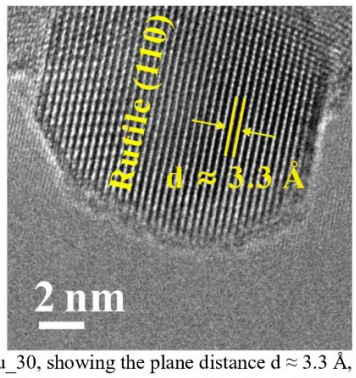

Figure S6: HR-TEM images of Ru_30, showing the plane distance d ≈ 3.3 Å, which is shorter than the d-spacing of Ru_30_250R shown in Fig 3c, indicating a lattice expansion along (110) direction after hydrogen treatment at 250 °C.

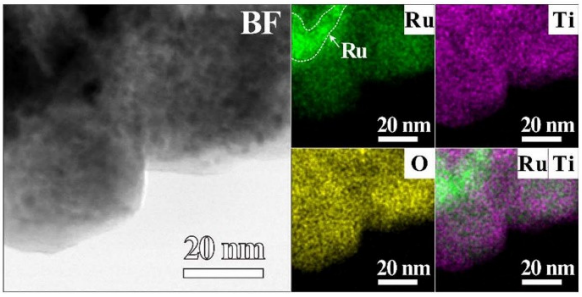

Figure S7: High resolution bright field (BF) images of Ru_30_250R with metallic Ru particles. EDS mapping images are also presented on the right: green = Ru; magenta = Ti; yellow = O.

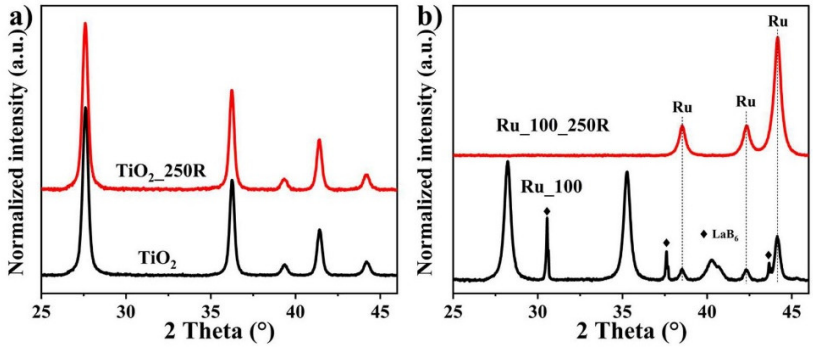

Figure S8: XRD diffraction from Ru_100 (a) and pure rutile TiO_2 (b) before and after reduction treatment with 4%H_2/N_2 at 250 °C.

Table S2: Microstrain and crystallite size of different catalysts determined by Williamson-Hall method.

Catalyst	Microstrain	Crystallite size (nm)
Ru_30_250R	0.0120	12.2 ± 3
Ru_30_250R_50O	0.0063	11.5 ± 4
Ru_30_250R_100O	0.0020	12.2 ± 1
Ru_30_250R_200O	0.0013	11.9 ± 1
Ru_30_250R_300O	0.0005	11.2 ± 1
Ru_30_250R_H_2_3 cycles	0.0070	13.1 ± 4
Ru_30_250R_C_3H_8_3 cycles	0.0020	13.8 ± 3

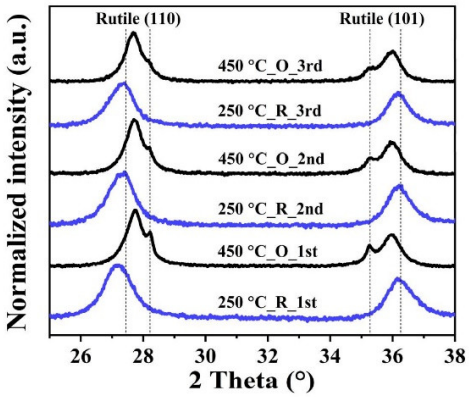

Figure S9: XRD patterns of Ru_30 catalysts after calcination in hydrogen at 250 °C and re-oxidation at 450 °C for three cycles.

Table S3: Optimized peak deconvolution information (cf. **Figure 3**) of Ru_30 catalyst treated in H_2/N_2 at different temperatures.

Catalyst	Rutile 110								
	Component (red)			Component (green)			RuO_2 (blue)		
	Pos.	FWHM	Area	Pos.	FWHM	Area	Pos.	FWHM	Area
Ru_30	-	-	-	27.77	0.64	0.80	28.23	0.17	0.12
Ru_30_150R	-	-	-	27.75	0.54	0.73	28.21	0.18	0.10
Ru_30_170R	27.11	0.89	0.31	27.70	0.69	0.73	28.22	0.19	0.09
Ru_30_190R	26.90	0.60	0.28	27.48	0.90	0.97	-	-	-
Ru_30_210R	29.91	0.41	0.14	27.19	1.06	0.99	-	-	-
Ru_30_230R	26.92	0.36	0.06	27.20	1.06	1.04	-	-	-
Ru_30_250R	-	-	-	27.20	1.10	1.22	-	-	-

Catalyst	Rutile 101								
	RuO_2 (blue)			Component (green)			Component (red)		
	Pos.	FWHM	Area	Pos.	FWHM	Area	Pos.	FWHM	Area
Ru_30	35.27	0.22	0.13	35.92	0.70	0.45	-	-	-
Ru_30_150R	35.25	0.23	0.11	35.88	0.63	0.45	-	-	-
Ru_30_170R	35.26	0.23	0.08	35.93	0.64	0.44	36.50	0.85	0.20
Ru_30_190R	-	-	-	36.06	0.79	0.67	36.65	0.83	0.18
Ru_30_210R	-	-	-	36.24	0.90	0.63	36.92	0.66	0.13
Ru_30_230R	-	-	-	36.24	0.89	0.60	36.83	0.50	0.09
Ru_30_250R	-	-	-	36.24	1.04	0.71	-	-	-

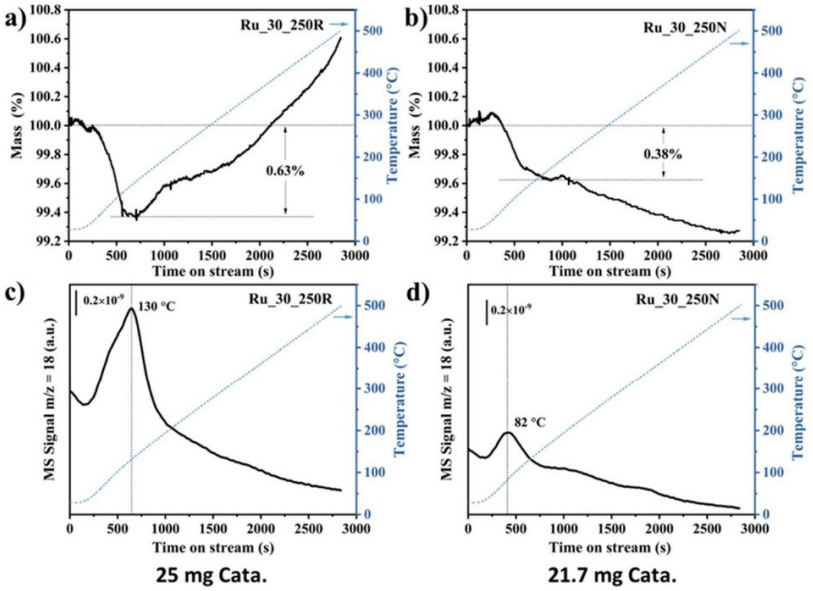

Figure S10: TGA-MS raw data of Ru_30_250R and Ru_30_250N. The catalyst is heated from room temperature to 500 °C under 30 mL/min of dry air. Mass spectrometry (c, d) is used to monitor the gas composition during the heating ramp. After peak deconvolution of H_2O signal (m/z = 18) (cf. **Figure 4**), the amount of inserted hydrogen is calculated by the difference of the integral area of H_2O. The amount of inserted hydrogen is also counterchecked by the difference of the weight loss in TG (a, b), the estimated H% is 18.3%, which is very close to the value calculated by the MS data (17.6%).

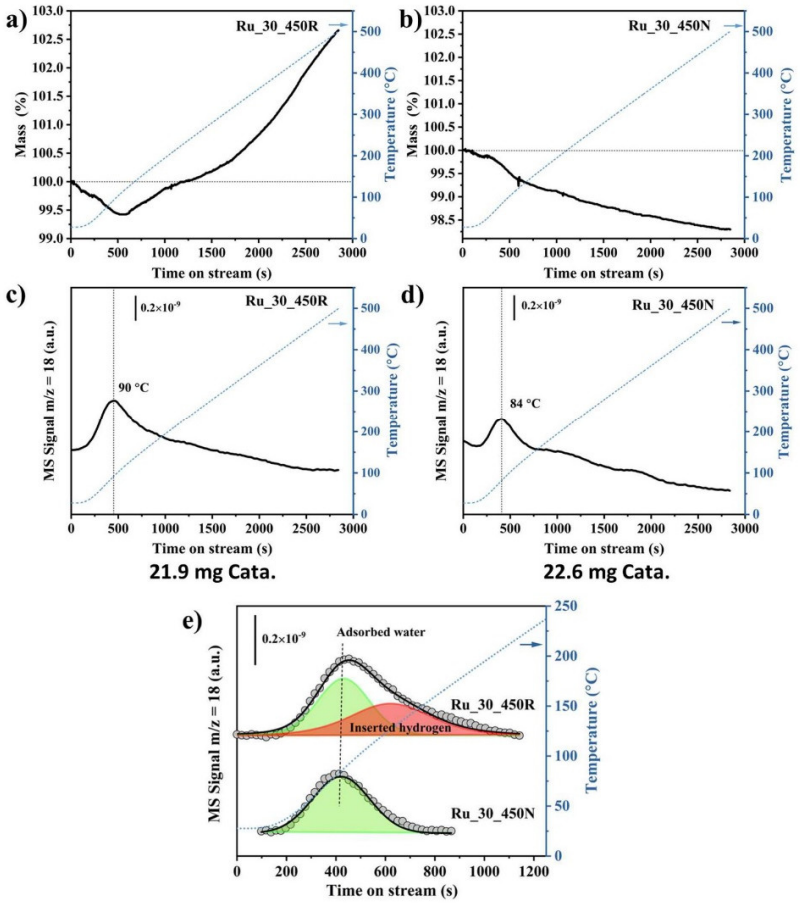

Figure S11: TGA-MS raw data of Ru_30_450R and Ru_30_450N. The catalyst is heated from room temperature to 500 °C under 30 mL/min of dry air. Mass spectrometer (c, d) is used to monitor the gas composition during the heating ramp. e) The amount of inserted hydrogen is calculated by the difference of the integral area of H_2O, indicating lower incorporation of hydrogen into the lattice (6.6 mol%) than for Ru_30_250R (17.6 mol%).

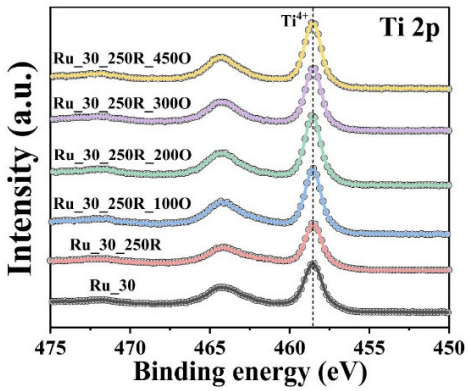

Figure S12: XPS-Ti 2p for fresh Ru_30 in comparison to hydrogen treated sample and the re-oxidized one.

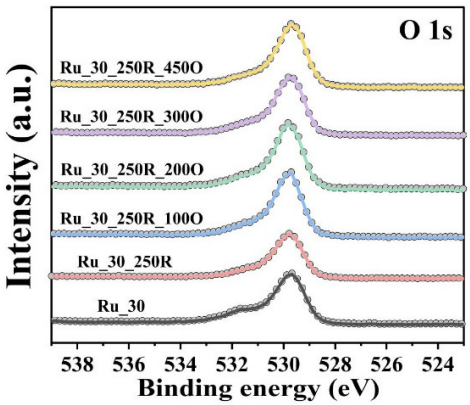

Figure S13: XPS-O1s for fresh Ru_30 in comparison to hydrogen treated sample and the re-oxidized one.

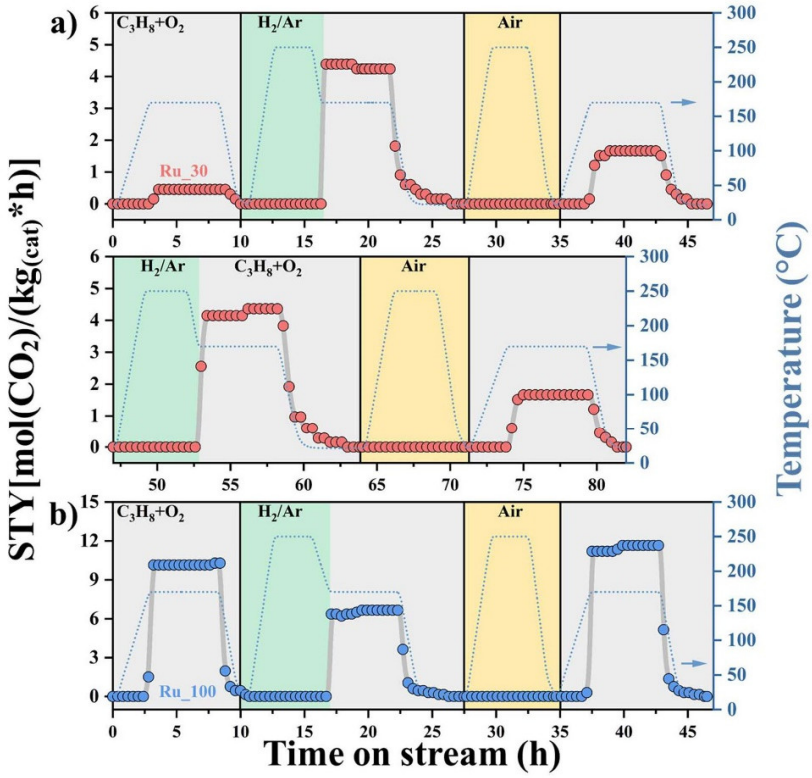

Figure S14: STY as a function of reaction time on catalytic propane combustion over a) Ru_30 and b) Ru_100 when measured for 3 cycles at 170 °C (blue dotted line). Before switched to the reaction mixture the catalyst is exposed to different gas atmosphere during the heat ramping: first under reaction mixture, followed by reduction under 4% H_2/Ar for 3 hours, and last pretreated under air for 3 hours. The grey background represents total C_3H_8 oxidation reaction conditions: 1 vol% C_3H_8, 5 vol% O_2, balanced by N_2; total volume flow: 100 sccm/min, temperature ramp: 1 K/min. The green background represents the gas mixture during heating and cooling stage: 4% H_2/Ar, total volume flow: 50 sccm/min. The yellow background represents the gas mixture during the heating and cooling stage: Air, 50 sccm/min.

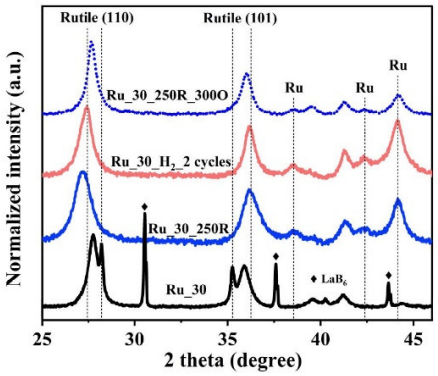

Figure S15: XRD data before and after cyclic experiments at 250 °C for Ru_30. HCl oxidation reaction conditions: 3 sccm HCl, 1.5 sccm O_2, balanced by Ar; total volume flow: 15 sccm/min. The XRD patterns of fresh Ru_30, Ru_30_250R and Ru_30_250R_300O are also presented as reference; the dotted lines are guiding lines to follow the shift in 2θ. Here Ru_30_H_2_2 cycles means the catalyst after 2 cycles (2 in-situ treatments under hydrogen and then switched to reaction mixture) of Deacon tests and finally cooled down under 4% H_2/Ar.

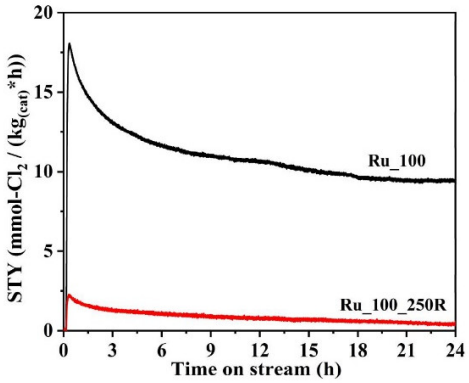

Figure S16: Catalytic HCl oxidation test of fresh Ru_100 sample in comparison to that of Ru_100_250R at 250 °C. Ru_100_250R is about one order of magnitude less active in HCl oxidation than Ru_100. Reaction conditions: 3 sccm HCl, 1.5 sccm O_2, balanced by Ar; total volume flow: 15 sccm/min.

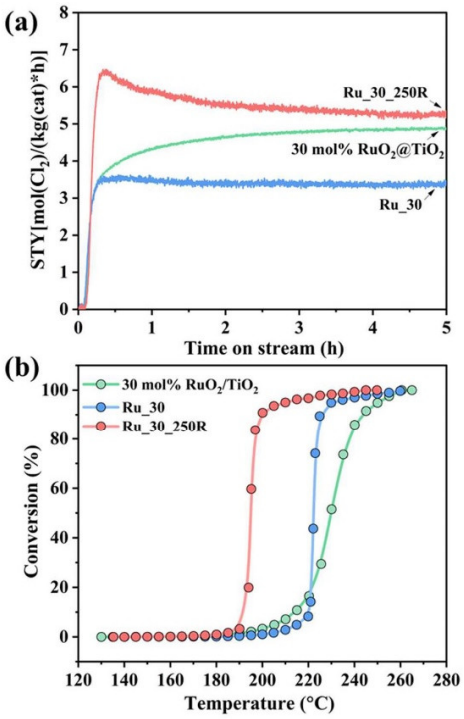

Figure S17: Catalytic HCl oxidation test at 250 °C (a) and propane oxidation test (b) of 30 mol% RuO_2/TiO_2_rutile catalyst, the benchmark catalyst, however with similar Ru loading as Ru_30 in comparison with catalytic tests of Ru_30 and Ru_30_250R. Reaction conditions for HCl oxidation: 3 sccm HCl, 1.5 sccm O_2, balanced by Ar; total volume flow: 15 sccm/min; Reaction conditions for propane oxidation: 1 vol% C_3H_8, 5 vol% O_2, balanced by N_2; total volume flow: 100 sccm/min, temperature ramp: 1 K/min. 30 mol% RuO_2/TiO_2_rutile catalyst is prepared by incipient wetness impregnation method and calcined at 450 °C for 4 h.

4.3 List of Abbreviations

DSAs	dimensionally stable anodes
DPC	differential phase contrast
DFT	density functional theory
EDS	energy dispersive spectroscopy
HER	hydrogen evolution reaction
HR-TEM	high resolution transmission electron microscopy
HAADF-STEM	high-angle annular dark-field scanning transmission electron microscopy
HRCLS	high-resolution core-level shift
INS	inelastic neutron scattering
IRAS	infrared reflection absorption spectroscopy
LEED	low-energy electron diffraction
L-H	Langmuir-Hinshelwood
LPG	liquid petroleum gas
M-K	Mars van Krevelen
NPs	nanoparticles
NPD	neutron powder diffraction
OER	oxygen evolution reaction
OSC	oxygen storage capacity
PGAA	prompt gamma activation analysis
PM	particulate matter
STY	space time yield
SEM	scanning electron microscopy
SMSI	strong metal support interaction
TG-MS	thermogravimetric mass spectrometry
TEM	transmission electron microscopy
TDS	thermal desorption spectra
TAP	temporal analysis of products

UHV	ultra-high vacuum
WDS	wavelength dispersive X-ray spectroscopy
XRD	X-ray diffraction
XPS	X-ray photoelectron spectroscopy

4.4 List of Peer-Reviewed Publications and Articles to be Submitted

1. **Wei Wang**, Phillip Timmer, Alexander Spriewald Luciano, Yu Wang, Tim Weber, Lorena Glatthaar, Yun Guo*, Bernd M. Smarsly*, Herbert Over*. Inserted Hydrogen Promotes Oxidation Catalysis of Mixed $Ru_{0.3}Ti_{0.7}O_2$ as Exemplified with Total Propane Oxidation and the HCl Oxidation Reaction. *Catalysis Science & Technology*, 2023, 13, 1395–1408.

2. **Wei Wang**, Yu Wang, Phillip Timmer, Alexander Spriewald Luciano, Lorena Glatthaar, Yun Guo*, Bernd M. Smarsly*, Herbert Over*. Hydrogen Incorporation in $Ru_xTi_{1-x}O_2$ Mixed Oxides Promotes Total Oxidation of Propane. *Inorganics*, 2023, 11(8), 330.

3. **Wei Wang**, Yajie Liu, Li Wang*, Wangcheng Zhan, Yanglong Guo, Yun Guo*. Soot Combustion over Ag Catalysts Supported on Shape-controlled CeO_2. *Catalysis Today*, 2021, 376, 9–18.

4. Zheng Wang, **Wei Wang**, Omeir Khalid, Tim Weber, Alexander Spriewald Luciano, Wangcheng Zhan*, Bernd M. Smarsly*, Herbert Over*. Supported $Ru_xIr_{1-x}O_2$ Mixed Oxides Catalysts for Propane Combustion: Resistance Against Water Poisoning. *ChemCatChem*, 2022, 14. DOI: 10.1002/cctc.202200149R2.

5. Zheng Wang, Omeir Khalid, **Wei Wang**, Yu Wang, Tim Weber, Alexander Spriewald Luciano, Wangcheng Zhan*, Bernd M. Smarsly*, Herbert Over*. Comparison Study of the Effect of CeO_2-based Carrier Materials on the Total oxidation of CO, Methane, and Propane over RuO_2. *Catalysis Science & Technology*, 2021, 11, 6839–6853.

6. Yu Wang, Jaime Gallego, **Wei Wang**, Phillip Timmer, Min Ding, Alexander Spriewald Luciano, Tim Weber, Lorena Glatthaar, Yanglong Guo *, Bernd M. Smarsly*, Herbert Over*. Unveiling the Self-activation of Exsolved $LaFe_{0.9}Ru_{0.1}O_3$ Perovskite during Catalytic Propane Combustion. *Chinese Journal of Catalysis*, 2023, in press.

7. Zhou Shang, Min Sun, Xiang Che, **Wei Wang**, Li Wang*, Xiaoming Cao, Wangcheng Zhan, Yanglong Guo, Yun Guo*, Guanzhong Lu. The Existing States of Potassium Species in K-doped Co_3O_4 Catalysts and Their Influence on the Activities for NO and Soot Oxidation. *Catalysis Science & Technology*, 2017, 7, 4710–4719.